

Propagating Quantum Microwaves: Dual-path State Reconstruction and Path Entanglement

Dissertation

Edwin Peter Kurt Menzel

December 2013

Advisor: Prof. Dr. Rudolf Gross

Fakultät für Physik

TECHNISCHE UNIVERSITÄT MÜNCHEN

TECHNISCHE UNIVERSITÄT MÜNCHEN

Fakultät für Physik

Lehrstuhl E23 für Technische Physik

Walther-Meißner-Institut für Tieftemperaturforschung
der Bayerischen Akademie der Wissenschaften

Propagating Quantum Microwaves: Dual-path State Reconstruction and Path Entanglement

Edwin Peter Kurt Menzel

Vollständiger Abdruck der von der Fakultät für Physik der Technischen
Universität München zur Erlangung des akademischen Grades eines

Doktors der Naturwissenschaften

genehmigten Dissertation.

Vorsitzender: Univ.-Prof. Dr. J. Leo van Hemmen

Prüfer der Dissertation: 1. Univ.-Prof. Dr. Rudolf Gross
2. Univ.-Prof. Jonathan J. Finley, Ph.D.

Die Dissertation wurde am 29. Oktober 2013 bei der
Technischen Universität München eingereicht und durch
die Fakultät für Physik am 4. Dezember 2013 angenommen.

Divide et impera!

Translation: "Divide and rule!"

This maxim characterizing the foreign policy of the Roman ruler Gaius Iulius Caesar should only be applied to noise.

To my parents

Abstract

The work presented in this thesis constitutes an important contribution to the flourishing field of quantum microwave photonics. Quantum states of microwave light are prepared by applying Josephson-junction-based superconducting circuits. In order to avoid thermal excitations at gigahertz frequencies, temperatures of a few tens of millikelvins are obligatory for experiments with propagating quantum microwaves. In addition to demanding cryogenics, superconducting micro- and nanocircuits, advanced microwave technology, and realtime data processing present substantial challenges. In this work, we get over several hurdles to master these challenges. In particular, we illuminate the rich physics of propagating quantum microwaves with a novel characterization technique developed in this thesis: the dual-path state reconstruction method. To this end, we develop the theoretical foundations of this method, present its implementation and demonstrate its applicability. To gain more insight into the quantum noise properties of microwave beam splitters, which are key components of the dual-path method, we investigate thermal states and perform Planck spectroscopy. Aiming at the generation of non-classical states, we then characterize the amplification, squeezing and noise properties of a Josephson parametric amplifier (JPA). Applying the dual-path method, we reconstruct the squeezed vacuum, squeezed thermal and squeezed coherent states generated by the JPA and perform a detailed analysis of the squeezing physics. Finally, we make first steps towards the implementation of quantum information processing and communication protocols in the microwave domain by superposing the non-classical squeezed state with the vacuum at a beam splitter to prepare path entanglement. We detect and quantify the entanglement by directly investigating the correlations between the microwave signals propagating along spatially separated paths. We emphasize that the observed entanglement can easily be distributed. In contrast to other work, the frequency of the microwaves propagating along the two paths is degenerate and our entangler and detector are based on different experimental techniques.

Kurzzusammenfassung

Die vorgelegte Dissertation stellt einen wichtigen Beitrag zu dem aufstrebenden Forschungsgebiet der Quantenmikrowellenphotonik dar. Quantenzustände des Mikrowellenlichts werden mittels supraleitender Schaltkreise, welche auf Josephson-Kontakten basieren, präpariert. Um thermische Anregungen bei Gigahertzfrequenzen zu vermeiden sind Temperaturen von einigen zehn Millikelvin unerlässlich für Experimente mit propagierenden Quantenmikrowellen. Zusätzlich zur anspruchsvollen Kryotechnik stellen supraleitende Mikro- und Nanoschaltkreise, hochentwickelte Mikrowellentechnologie und Datenverarbeitung in Echtzeit die wesentlichen Herausforderungen dar. In dieser Arbeit unternehmen wir wichtige Schritte um diese Anforderungen zu meistern. Insbesondere beleuchten wir die reichhaltige Physik propagierender Quantenmikrowellen mit einem von uns entwickelten neuartigen Charakterisierungsverfahren, der Zweipfadmethode zur Zustandsrekonstruktion. Hierzu entwickeln wir die theoretischen Grundlagen dieser Methode, stellen ihre Implementierung dar und demonstrieren ihre Anwendung. Um mehr Einblick in die Quantenrauscheigenschaften von Mikrowellenstrahlteilern, die eine zentrale Komponente der Zweipfadmethode sind, zu erlangen untersuchen wir thermische Zustände und wenden Planckspektroskopie an. Mit der Zielsetzung nichtklassische Zustände zu generieren, charakterisieren wir die Verstärkungs-, Quetsch- und Rauscheigenschaften eines Josephson parametrischen Verstärkers. Unter Verwendung der Zweipfadmethode rekonstruieren wir gequetschte Vakuumzustände, gequetschte thermische und gequetschte kohärente Zustände, die wir mit dem Josephson parametrischen Verstärker erzeugen, und analysieren im Detail die Physik des Quetschens. Schließlich unternehmen wir erste Schritte im Hinblick auf die Implementierung von Protokollen der Quanteninformationsverarbeitung und Quantenkommunikation im Mikrowellenbereich, indem wir nichtklassische gequetschte Zustände und Vakuumzustände in einem Strahlteiler überlagern um eine Verschränkung zu präparieren. Wir detektieren und quantifizieren die Verschränkung durch die direkte Untersuchung von Korrelationen zwischen den Mikrowellensignalen, die entlang räumlich getrennter

Pfade propagieren. Wir betonen, dass die Verschränkung leicht verbreitet werden kann. Gegenüber anderen Arbeiten ist die Frequenz der Mikrowellen, die entlang der zwei Pfade propagieren, entartet und der von uns verwendete Detektor basiert auf einer anderen experimentellen Technik als der Verschränker.

Contents

| | | |
|----------|---|-----------|
| 1 | Introduction | 1 |
| 2 | Propagating classical and quantum microwaves | 5 |
| 2.1 | Classical representation of microwave states | 5 |
| 2.2 | Quantum representations of microwave states | 6 |
| 2.2.1 | Density operator | 6 |
| 2.2.2 | Quasi-probability distributions | 7 |
| 2.2.3 | Moments of the annihilation and creation operators | 9 |
| 2.3 | Important microwave states | 10 |
| 2.3.1 | Thermal states | 10 |
| 2.3.2 | Coherent states | 11 |
| 2.3.3 | Squeezed states | 12 |
| 2.3.4 | Squeezed coherent states | 13 |
| 2.4 | Detection of microwave quantum correlations | 15 |
| 2.5 | Dual-path state reconstruction – classical treatment | 16 |
| 2.6 | Dual-path state reconstruction – quantum treatment | 20 |
| 2.7 | Wigner function reconstruction | 23 |
| 2.8 | Path entanglement via a beam splitter | 24 |
| 2.9 | Reference-state method for the detection of path entanglement | 25 |
| 2.10 | Entanglement witness | 26 |
| 2.11 | Negativity | 27 |
| 2.12 | Gaussianity and higher order cumulants | 28 |
| 3 | Experimental techniques | 31 |
| 3.1 | Dual-path setup for weak propagating microwaves | 31 |
| 3.1.1 | Generation of classical mixtures of weak coherent states | 32 |
| 3.1.2 | Cryogenic setup | 35 |
| 3.1.3 | Cross-correlation detector | 44 |
| 3.1.4 | Calibration | 46 |
| 3.2 | Josephson Parametric Amplifier | 48 |
| 3.2.1 | Principle of operation | 48 |
| 3.2.2 | The JPA sample | 51 |
| 3.2.3 | Characterization setup | 52 |
| 3.2.4 | Optimization of the operation point | 56 |

| | | |
|----------|--|------------|
| 3.3 | Dual-path setup for propagating quantum microwaves and path entanglement | 56 |
| 3.3.1 | Cryogenic setup | 57 |
| 3.3.2 | IQ cross-correlation detector | 64 |
| 3.3.3 | Data acquisition and processing by FPGA logic | 66 |
| 3.3.4 | Calibration | 73 |
| 3.4 | Stability of the experimental setup | 76 |
| 3.4.1 | Stabilization of amplifier gain and cable losses | 77 |
| 3.4.2 | Phase stabilization protocol | 78 |
| 4 | Detection of weak propagating microwaves | 81 |
| 4.1 | Planck spectroscopy and quantum noise of microwave beam splitters . | 81 |
| 4.1.1 | Planck spectroscopy | 84 |
| 4.1.2 | Quantum noise of microwave beam splitters | 86 |
| 4.2 | Dual-path noise suppression | 89 |
| 4.3 | Dual-path weak signal mixtures | 92 |
| 5 | Squeezing and path entanglement | 95 |
| 5.1 | JPA characterization measurements | 95 |
| 5.1.1 | Operation point | 96 |
| 5.1.2 | Non-degenerate gain | 97 |
| 5.1.3 | Bandwidth | 98 |
| 5.1.4 | 1 dB-compression point | 99 |
| 5.1.5 | JPA noise properties in non-degenerate mode | 99 |
| 5.1.6 | Degenerate gain | 101 |
| 5.2 | Homodyne detection of squeezed vacuum | 101 |
| 5.3 | Dual-path state reconstruction | 104 |
| 5.3.1 | Reconstruction of coherent states | 105 |
| 5.3.2 | Reconstruction of squeezed vacuum and squeezed thermal states | 106 |
| 5.3.3 | JPA noise properties in degenerate mode | 112 |
| 5.4 | Path entanglement | 114 |
| 6 | Conclusions and outlook | 119 |
| A | Superconducting coil and persistent current switch | 123 |
| | Bibliography | 127 |
| | List of publications | 141 |
| | Acknowledgments | 143 |

List of Figures

| | | |
|------|---|----|
| 2.1 | Thermal state | 11 |
| 2.2 | Coherent state | 11 |
| 2.3 | Squeezed state | 13 |
| 2.4 | Squeezed coherent states | 14 |
| 2.5 | Schematics of the dual-path amplification and detection setup | 18 |
| | | |
| 3.1 | Microwave pulses with various phase shifts | 32 |
| 3.2 | Phase-shifted microwave pulses | 33 |
| 3.3 | Control pulses for the generation of signal mixtures | 34 |
| 3.4 | Sketch of the beam splitters used in our experiments | 36 |
| 3.5 | Schematics of the dual-path setup with hybrid ring | 39 |
| 3.6 | Schematics of the dual-path setup with power divider | 40 |
| 3.7 | Photographs of the dual-path setups | 41 |
| 3.8 | Photograph of the still and 4.2 K-stage | 43 |
| 3.9 | Flux-driven JPA | 49 |
| 3.10 | Micrographs of the JPA sample #2-1c | 51 |
| 3.11 | Schematic of the JPA characterization setups | 53 |
| 3.12 | Photographs of the base plate of the JPA characterization setup | 54 |
| 3.13 | Flux sweep for optimization of signal gain | 57 |
| 3.14 | Sketch of the path entanglement setup | 58 |
| 3.15 | Photograph of the sample plate of the path entanglement setup | 60 |
| 3.16 | Measurement protocol for squeezed and coherent states | 62 |
| 3.17 | Photograph of the cryogenic path entanglement setup | 64 |
| 3.18 | Sketch of the IQ cross-correlation detector | 65 |
| 3.19 | Photograph of the IQ cross-correlation detector | 66 |
| 3.20 | Photograph of the measurement devices | 67 |
| 3.21 | Sketch of the physical layer processing chain of the FPGA logic | 69 |
| 3.22 | Sketch of the data processing in the FPGA logic | 70 |
| 3.23 | Transmission characteristics of the IQ cross-correlation detector | 71 |
| 3.24 | Input range of the FPGA board | 74 |
| 3.25 | Gain calibration using thermal input states | 76 |
| 3.26 | Stabilization of squeezed state phase | 79 |
| | | |
| 4.1 | Equivalent circuits of the microwave beam splitters | 82 |
| 4.2 | Planck spectroscopy of thermal microwave states | 85 |

| | | |
|------|---|-----|
| 4.3 | Full correlation function and covariance matrices | 87 |
| 4.4 | Variance and covariance vs. temperature using a hybrid ring | 88 |
| 4.5 | Amplifier noise suppression | 90 |
| 4.6 | Dynamic range of mean value and cross-product | 91 |
| 4.7 | Time-dependent variance | 93 |
| 4.8 | Statistical mixtures of phase-shifted pulses | 94 |
| | | |
| 5.1 | JPA signal gain vs. frequency and magnetic flux | 96 |
| 5.2 | Pump power dependence of the idler and signal gain | 97 |
| 5.3 | Signal and idler bandwidth for various values of the pump power | 98 |
| 5.4 | 1 dB-compression point | 99 |
| 5.5 | Noise temperature of the JPA in non-degenerate operation mode | 100 |
| 5.6 | Phase dependence of degenerate gain | 102 |
| 5.7 | Homodyne detection of squeezed vacuum fluctuations | 103 |
| 5.8 | Layout of the path entanglement experiment | 104 |
| 5.9 | Dual-path reconstruction of coherent states | 105 |
| 5.10 | Coherent state reconstruction | 106 |
| 5.11 | Typical averaged time traces of selected second moments | 107 |
| 5.12 | Reconstruction of a squeezed vacuum state with the dual-path method | 108 |
| 5.13 | Phase control for squeezed state reconstruction | 109 |
| 5.14 | Wigner functions of squeezed vacuum and squeezed thermal states | 110 |
| 5.15 | Dependence of the squeezing level on the JPA signal gain and on noise source temperature | 111 |
| 5.16 | JPA noise temperature in degenerate operation mode | 113 |
| 5.17 | Path entanglement generated applying squeezed thermal states | 117 |
| 5.18 | Dependence of the path entanglement on the JPA signal gain | 118 |
| | | |
| 6.1 | Squeezed coherent states | 121 |
| | | |
| A.1 | Superconducting coil and persistent current switch | 124 |
| A.2 | Calculated magnetic field of the superconducting coil | 125 |
| A.3 | Characteristics of persistent current switch | 125 |

List of Tables

| | | |
|-----|---|-----|
| 2.1 | Summary of state properties | 15 |
| 5.1 | JPA noise and gain in degenerate operation mode | 114 |

Chapter 1

Introduction

Over the last few years, the investigation of the quantum properties carried by propagating microwave fields has evolved into a highly active research area [1]. While the accurate reconstruction of the involved quantum states is obviously of fundamental interest, propagating microwave fields are now more generally being considered as promising candidates for the processing and exchange of quantum information. These two tasks, which are designated quantum computing and quantum communication [2], aim at exploiting the fascinating features of quantum mechanics to improve the already impressive capabilities of today's classical information processing and communication systems beyond fundamental limitations [3–5].

For microwave fields confined to small regions of space, there has been significant progress towards the construction of a quantum information processor in the last decade. More precisely, proof-of-principle quantum information architectures were realized at the level of a few superconducting quantum bits and resonators with transition frequencies of a few gigahertz [6–11]. Propagating microwave fields however, are so far restricted to classical applications. Nevertheless, these applications are closely related to cornerstones of modern communication such as wireless networks, mobile communication, or the clocks for processing units. Propagating *quantum* microwaves now promise to provide a technological link between classical microwave-based information processing and superconducting quantum processors.

Our work represents an important contribution to the flourishing field of quantum microwave photonics [1]. Quantum states of microwave light are prepared applying Josephson-junction-based superconducting circuits [12–14]. For instance, circuit quantum electrodynamic (QED) systems combine the large dipole moments of macroscopic artificial atoms [7, 15, 16] with the enhanced field strengths in one-dimensional transmission line resonators to achieve strong interactions between mi-

microwave light and matter [6, 17–19]. While there is a close analogy to quantum-optical cavity QED¹ [4], a regime with a light-matter interaction of unprecedented strength at the single-atom-single-photon level has become accessible in circuit QED [22].

The most relevant quantum circuit in this work is a Josephson parametric amplifier (JPA) which can generate non-classical microwave states. The physics of this device is described by the interaction of a microwave field with a non-linear medium [23] or, equivalently, as a resonator whose frequency is varied rapidly resulting in parametric effects. JPAs can squeeze input states in a way that the quantum noise along a certain direction in phase space is below that of the vacuum [24, 25]. Squeezed states with this property are non-classical [26] and represent key elements of quantum information processing and communication (QIPC) protocols [27].

The intra-cavity field inside the JPA is transformed into a *propagating* mode by simply leaking into an open transmission line [28]. Alternatively, matter can be directly coupled to the continuum of the electromagnetic field in an open transmission line. For example, a single artificial atom coupled strongly to a transmission line scatters coherent states and reflects them back at resonance [29, 30] providing non-classical microwave fields [31]. This system also forms the basis for fast microwave switches [30, 32] and microwave amplification by stimulated emission of radiation [33]. By terminating a transmission line with a superconducting quantum interference device and pumping the latter with a microwave tone the dynamical Casimir effect has been observed [34].

Many of the results above were realized in continuous-variable systems. Prototypical examples for continuous variables (CV) are the position and momentum of a particle. For quantum microwaves, these conjugate variables correspond to field quadratures representing the real and imaginary part of the complex field amplitude. CVs can be exploited to encode quantum information in QIPC protocols [5]. Following this approach, quantum key distribution [35, 36], quantum teleportation [37–39], preparation of distant entangled atomic ensembles [40] and quantum memory [41] have been demonstrated in the optical regime. However, in the microwave realm the realization of QIPC protocols based on CV still represents an open issue. Entanglement is at the heart of these quantum technologies. We note that it must occur between spatially separated subsystems in order to be a resource in quantum communication protocols [3].

¹Serge Haroche from Laboratoire Kastler Brossel de l’Ecole Normale Supérieure and Collège de France has been awarded with the Nobel Prize in 2012 for the quantum non-demolition detection of intra-cavity microwaves with flying atoms [20, 21].

For the investigation of quantum properties, the measurement process is of central relevance. The reconstruction of quantum states is referred to as tomography. Part of the work presented in this thesis has laid the foundations for the tomography of propagating quantum microwaves, which has become an independent, exciting research area. In addition, other groups actively contributed to this field [13, 28, 42–45]. Although the reconstruction of intra-cavity fields in the microwave regime is well established [14, 46], the applied technique can not be adapted for propagating quantum microwaves. Similarly, schemes for the quantum state reconstruction of propagating light modes [47–49] such as optical homodyning fail in the microwave realm due to the lack of efficient photon detectors. Despite notable progress from theoretical proposals [50–54] to first experimental realizations [55] of microwave photon detectors, they still lack number resolution, which is a prerequisite for optical homodyning. The reason for this is the small energy scale of microwave photons which is five orders of magnitude below that of visible light. The equivalent power in a megahertz bandwidth of microwave signals on the single-photon level is a few attowatts and, consequently, the detection requires amplification. However, the unavoidable noise added by commercially available amplifiers obscures the tiny quantum signals. We want to note that until 2010, no experimental ansatz to this problem existed. One strategy is to minimize the added amplifier noise by using JPAs in the phase-sensitive operation mode [56]. In contrast, our approach is to use off-the-shelf amplifiers and to apply signal reconstruction techniques. To this end, we have developed the dual-path state reconstruction scheme [57] which empowers us to characterize quantum states in the presence of considerable amplifier noise with linear detectors. At the same time, it allows us to reconstruct the amplifier noise.

In order to avoid thermal excitations at gigahertz frequencies temperatures of a few tens of millikelvins are obligatory for experiments with propagating quantum microwaves. In addition to demanding cryogenics, superconducting micro- and nanocircuits, advanced microwave technology, and realtime data processing present substantial challenges. In this work, we get over several hurdles to master these challenges. In particular, we illuminate the rich physics of propagating quantum microwaves with a novel characterization technique developed in this thesis: the dual-path state reconstruction method [57]. To this end, we develop the theoretical foundations of this method, present its implementation and demonstrate its applicability. To gain more insight into the quantum noise properties of microwave beam splitters, which are key components of the dual-path method, we investigate thermal states and perform Planck spectroscopy [58]. Aiming at the genera-

tion of non-classical states, we then characterize the amplification, squeezing and noise properties of a JPA [59]. Applying the dual-path method, we reconstruct the squeezed vacuum, squeezed thermal and squeezed coherent states generated by the JPA [59] and perform a detailed analysis of the squeezing physics. Finally, we make first steps towards the implementation of QIPC protocols in the microwave domain by superposing the non-classical squeezed state with the vacuum at a beam splitter to prepare path entanglement [60,61]. We detect and quantify the entanglement by directly investigating the correlations between the microwave signals propagating along spatially separated paths. We emphasize that the observed entanglement can easily be distributed. In contrast to other work [62], the frequency of the microwaves propagating along the two paths is degenerate and our entangler and detector are based on different experimental techniques.

The thesis is structured in the following way. In chapter 2, we introduce propagating classical and quantum microwaves and develop the theoretical foundations of the dual-path state reconstruction method and the entanglement detection. Next, we present the experimental techniques in chapter 3. In chapter 4, we discuss the detection of weak propagating microwaves. Chapter 5 focuses on the generation of squeezing using a JPA, the state reconstruction of various squeezed states and the generation and detection of path entanglement. Finally, we conclude our work and give an outlook in chapter 6.

Chapter 2

Propagating classical and quantum microwaves

In this chapter, we introduce the theoretical foundations of our work. First, we consider single-mode microwave states and their reconstruction. We begin with different descriptions of quantum microwaves and give examples for common and important states. Next, we develop the theory of the dual-path state reconstruction method providing, in principle, access to all statistical moments of the signal. Following the chronological evolution of our work, we start with a classical treatment and then generalize for quantum states. Subsequently, we show how one can retrieve the Wigner function from the reconstructed moments.

Second, we investigate correlations between two spatially separated modes which enables us to study path entanglement. Therefore, we describe the generation of path entanglement using a beam splitter. In what follows, we discuss the detection of path entanglement by introducing the reference-state method and an entanglement witness. Finally, we treat the negativity as a measure of entanglement for Gaussian states.

2.1 Classical representation of microwave states

In general, microwaves are electromagnetic fields with a free-space wavelength between 1 m and 1 mm corresponding to frequencies between 300 MHz and 300 GHz [63]. In our case, we focus on frequencies in the range from 4 to 12 GHz, a part of the centimeter band. In our work, we consider itinerant microwaves which propagate in free space or along transmission line structures such as coaxial cables or coplanar wave guides. In general, the electromagnetic fields are governed by Maxwell's equa-

tions and the boundary conditions. However, when measuring microwave signals it is sufficient to consider terminal quantities such as current or voltage and one detects a time varying signal $a(t)$, which can be decomposed into its in-phase and out-of-phase quadrature components, $I(t)$ and $Q(t)$, respectively. In other words,

$$a(t) = I(t) \cos(2\pi ft) + Q(t) \sin(2\pi ft), \quad (2.1)$$

where f denotes the carrier frequency. For monochromatic microwaves such as those generated by a microwave source without any modulation present, the quadratures are constant. For signals whose bandwidth is much smaller than the carrier frequency, as it is relevant in our case, the quadratures are slowly varying on a time scale inversely proportional to the bandwidth and describe the envelope of the fast varying microwave signal. Technically speaking, the detection of this envelope is less demanding than the direct detection of the microwave tone itself. Furthermore, as the bandwidth of our signals is less than one per cent of the carrier frequency we can consider these signals as IQ modulated signals. Finally, we want to note that microwaves propagating along quasi one-dimensional transmission line structures used in superconducting microwave devices do not possess a polarization degree of freedom.

2.2 Quantum representations of microwave states

In this section, we give a short overview on different ways to describe single-mode quantum microwaves. Since our object of study is, in principle, light with frequencies in the gigahertz regime, we revert to a quantum-optical formalism. Furthermore, as the bandwidth of our signals is less than one per cent of the carrier frequency we can treat them as single modes. In the following, we present three equivalent representations of a quantum state, which have the same information content: density operator, quasi-classical distributions, and statistical moments.

2.2.1 Density operator

The density operator allows for a general description of fluctuation phenomena [64]. Among these are non-quantum stochastic effects such as thermal fluctuations as well as effects that do not have a classical analogon, such as vacuum fluctuations. The

density operator is defined as a convex sum of state projectors,

$$\hat{\rho} = \sum_{\Psi} P_{\Psi} |\Psi\rangle\langle\Psi|, \quad (2.2)$$

where P_{Ψ} is the probability to be in the state $|\Psi\rangle$. Via the trace one retrieves the expectation value of any field operator $\langle\hat{O}\rangle = \text{Tr}(\hat{O}\hat{\rho})$. A complete set often used to represent the density operator is the Fock or number state basis. The density operator is normalized, i.e., $\text{Tr}(\hat{\rho})=1$.

2.2.2 Quasi-probability distributions

The state of a classical system is represented by a point in phase space, which is spanned by Hermitian conjugate variables. In the case of an electromagnetic field mode which is described by a harmonic oscillator these coordinates are q and p . The quantity $P(q,p)dqdp$ is the probability to find the system in the phase space volume around the point (q,p) , thus defining $P(q,p)$ as a probability density function. Whereas in classical physics the system state is represented by a well-defined point (q,p) in phase space, this is no longer the case for quantum systems because the Heisenberg uncertainty relation

$$\Delta q \Delta p \geq \frac{1}{4} \quad (2.3)$$

prohibits the exact knowledge of q and p at the same time. Therefore, the concept of probability density was extended to quasi-probability distributions. The latter lack some properties of ordinary probability density functions such as positiveness [49]. Nevertheless, these quasi-probability distributions are rather useful as we will see in the following sections.

The first quasi-probability distribution was introduced by Wigner [65]. However, we will define the Wigner function using a more modern approach following the presentation in Ref. [66] based on the characteristic function [67]. To this end, we introduce the displacement operator $\hat{D}(\alpha) \equiv \exp[\alpha\hat{a}^{\dagger} - \alpha^*\hat{a}]$, where \hat{a} and \hat{a}^{\dagger} are the annihilation and creation operators obeying the bosonic commutator relation $[\hat{a}, \hat{a}^{\dagger}] = 1$ and α is the complex amplitude. The expectation value of the displacement operator is known as the symmetrically ordered characteristic function

$$\xi(\eta) = \text{Tr}\{\hat{\rho}\hat{D}(\eta)\} = \text{Tr}\{\hat{\rho}e^{n\hat{a}^{\dagger} - \eta^*\hat{a}}\}, \quad (2.4)$$

where η is a complex-valued variable. The characteristic function uniquely deter-

mines the density operator $\hat{\rho}$. The Wigner function is represented as the Fourier transform of the characteristic function $\xi(\eta)$

$$W(\alpha) = \frac{1}{\pi^2} \int \exp(\eta^* \alpha - \eta \alpha^*) \xi(\eta) d^2 \eta. \quad (2.5)$$

The Wigner function is well defined but it can become negative. When we introduce generalized quadrature operators

$$\hat{X}_\theta = \hat{q} \cos \theta + \hat{p} \sin \theta \quad (2.6)$$

and make use of the relation $\hat{X}_\theta = (\hat{a}^\dagger e^{i\theta} + \hat{a} e^{-i\theta})/2$, we retrieve the quadrature operators

$$\hat{q} = \frac{\hat{a} + \hat{a}^\dagger}{2} \quad \text{and} \quad \hat{p} = \frac{1}{i} \frac{\hat{a} - \hat{a}^\dagger}{2}. \quad (2.7)$$

Here, i is the imaginary unit and the eigenstates of \hat{q} and \hat{p} are denoted as $|q\rangle$ and $|p\rangle$. Next, we rewrite Eq. (2.5) in terms of the phase space variables q and p

$$W(q, p) = W(\alpha)|_{\alpha=q+ip}. \quad (2.8)$$

An alternative definition of the Wigner function is given by [49, 65]

$$W(q, p) = \frac{1}{2\pi} \int_{-\infty}^{\infty} \langle q - \zeta/2 | \hat{\rho} | q + \zeta/2 \rangle e^{ip\zeta} d\zeta, \quad (2.9)$$

where ζ is a real-valued integration variable. In Ref. [68] it is shown that both definitions are identical. The Wigner function is normalized

$$\int_{-\infty}^{\infty} \int_{-\infty}^{\infty} W(q, p) dq dp = 1 \quad (2.10)$$

and real valued for Hermitian operators $\hat{\rho}$. We note that Eq. (2.9) can also be derived by postulating only a single property [69] of the Wigner function, namely that it should behave like a joint probability distribution for q and p [49]. The marginal distributions for momentum and position are then given by $\int_{-\infty}^{\infty} W(q, p) dq$ and $\int_{-\infty}^{\infty} W(q, p) dp$, respectively.

Moreover, other quasi-probability functions such as the Glauber-Sudarshan P -representation [70, 71] or the Husimi Q -representation are defined in a very similar way to Eq. (2.5) but differ in the type of ordering used for the displacement operator with respect to the annihilation and creation operators. For the Q -representation anti-normally ordering is applied, whereas the P -representation is related to normal ordering [64].

For the states investigated in this work, the P -representation is inappropriate because it can become highly singular (a delta function for coherent states). Similar to the Wigner function, also the Q -function is a convolution of a Gaussian with the P -function. However, the Gaussian is so broad that the Q -function is never negative in contrast to the Wigner function, where negative values are signatures of non-classical behavior [72]. The Wigner function gives a good intuition for the quantum states as it represents the state in phase space. In this way, the vacuum state or squeezed states are well visualized.

2.2.3 Moments of the annihilation and creation operators

The knowledge of all moments $\langle (\hat{a}^\dagger)^m \hat{a}^n \rangle$ with $m, n \in \mathbb{N}_0$ is equivalent to the knowledge of the Wigner function or the density operator [73–76]. In order to retrieve the anti-normally ordered moments from the normally ordered ones, the following operator relation is applied:

$$\hat{a}^m (\hat{a}^\dagger)^n = \sum_{j=0}^{\min(m,n)} \binom{m}{j} \binom{n}{j} j! (\hat{a}^\dagger)^{n-j} \hat{a}^{m-j} \quad (2.11)$$

Stimulated by our work, Filippov and Man'ko [77, 78] developed a theoretical description of the degree of overlap between two states, the purity of a state and the evolution of microwave quantum states in terms of moments. However, we note that for these relations the knowledge of all moments is assumed. Contrarily, quantum-mechanical uncertainty relations can be formulated containing only moments up to a specific finite order. For second order [78], one retrieves

$$(\langle \hat{a}^\dagger \hat{a} \rangle - \langle \hat{a}^\dagger \rangle \langle \hat{a} \rangle) + (\langle \hat{a}^\dagger \hat{a} \rangle - \langle \hat{a}^\dagger \rangle \langle \hat{a} \rangle)^2 - (\langle (\hat{a}^\dagger)^2 \rangle - \langle \hat{a}^\dagger \rangle^2) (\langle \hat{a}^2 \rangle - \langle \hat{a} \rangle^2) \geq 0. \quad (2.12)$$

When relation Eq. (2.12) is violated, the state is unphysical and does not comply with the Heisenberg uncertainty relation. For the inequalities based on moments up to the fourth order we relegate the reader to Ref. [78]. Furthermore, in Ref. [79] it was shown that one has to consider at least moments up to the fourth order to find the negativity of the Wigner function in general and at least up to the eighth order for states with a rotationally invariant Wigner function. For a Fock state $|N\rangle$, only moments up to the N -th order are non-zero, which allows for the truncation of the Hilbert space. Finally, we want to note that Gaussian states, which are especially relevant in this work, are fully determined by the first two moments.

2.3 Important microwave states

In this section, we introduce the microwave states experimentally used in our work. We present their basic properties such as moments and Wigner function representation and visualize them in phase space.

2.3.1 Thermal states

Thermal states are chaotic light with no phase coherence. Consequently, the off-diagonal elements of the density operator are zero and the Wigner function is radially symmetric. Thermal states can easily be generated by black body emitters at suitable temperatures. In the microwave regime, these emitters are termination resistors, which have to be cooled to sub-Kelvin temperatures to obtain a small mean photon number \bar{n} . The latter is determined by the temperature T of the emitter via the Bose-Planck distribution

$$\bar{n} = \langle \hat{a}^\dagger \hat{a} \rangle = \frac{1}{\exp\left(\frac{hf}{k_B T}\right) - 1}, \quad (2.13)$$

where f is the frequency of the mode, h the Planck constant, and k_B the Boltzmann constant. The other non-zero moments of higher order are calculated from the mean photon number via

$$\langle (\hat{a}^\dagger)^m \hat{a}^n \rangle = m! \bar{n}^m \delta_{m,n} \quad (2.14)$$

with the Kronecker $\delta_{m,n}$.

The Wigner function is Gaussian

$$W_{\text{thermal}}(q, p) = \frac{1}{\pi \left(\bar{n} + \frac{1}{2}\right)} \exp\left(-\frac{q^2 + p^2}{\bar{n} + \frac{1}{2}}\right), \quad (2.15)$$

where the $1/e$ -contour is a circle with radius $\sqrt{\bar{n} + 1/2}$ centered at the origin of phase space. Thus, the area enclosed by the contour linearly depends on the mean photon number. The vacuum state exhibits minimum uncertainty, so that the equal sign in the Heisenberg uncertainty relation, Eq. (2.3), holds. An example for a thermal state with $\bar{n}=1$, equivalent to a temperature of 415 mK at $f=6$ GHz, is displayed in Fig. 2.1.

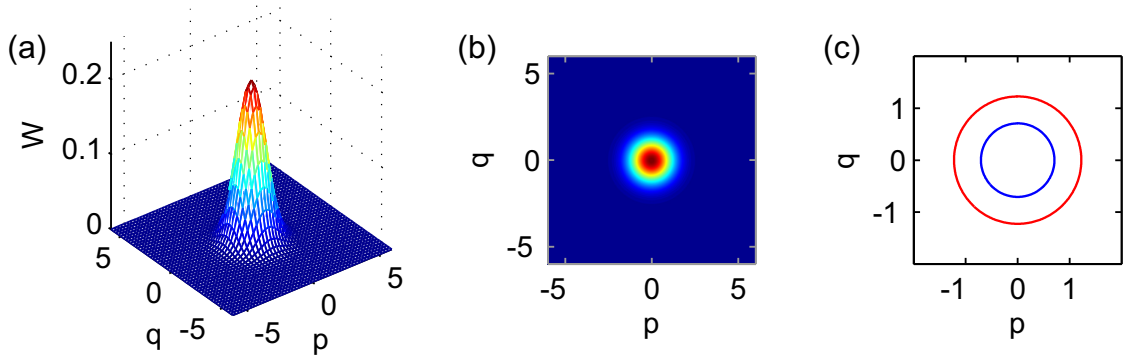


Figure 2.1: Wigner function of a thermal state with $\bar{n}=1$. (a) Mesh plot. (b) Color map plot. The color code is the same as the one used in panel (a). (c) $1/e$ -contours of Wigner functions of the vacuum (blue) and of a thermal state with $\bar{n}=1$ (red).

2.3.2 Coherent states

A coherent state $|\alpha\rangle$ is generated by applying the displacement operator $\hat{D}(\alpha)$ (cf. Sec. 2.2.2) to the vacuum. As shown in Fig. 2.2, the Gaussian blob of the vacuum is displaced by the vector α . Thus, the coherent state is a member of the class of minimum-uncertainty states.

The Wigner function of a coherent state $|\alpha\rangle = |Q + iP\rangle$ is

$$W(q, p) = \frac{2}{\pi} \exp \left[-2((q - Q)^2 + (p - P)^2) \right]. \quad (2.16)$$

Its $1/e$ -contour is given by

$$(q - Q)^2 + (p - P)^2 = \frac{1}{2} \quad (2.17)$$

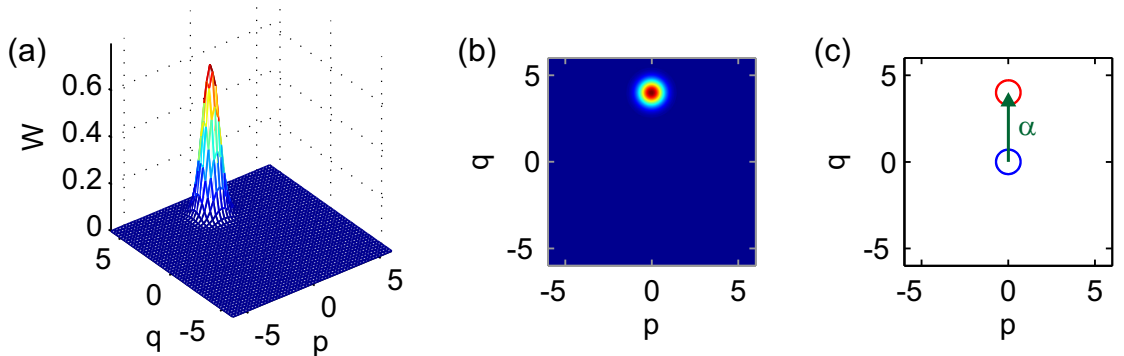


Figure 2.2: Wigner function of a coherent state with $\alpha=4$. (a) Mesh plot. (b) Color map plot. (c) $1/e$ -contours of Wigner functions of the vacuum (blue) and of the coherent state (red), whose contour is the one of the vacuum displaced by α .

and forms a circle with radius $1/\sqrt{2}$ centered on the point (Q, P) . We note that the coherent state is an eigenfunction of the annihilation operator, $\hat{a}|\alpha\rangle=\alpha|\alpha\rangle$. From this relation, we easily obtain the normally ordered moments $\langle\alpha|(\hat{a}^\dagger)^m\hat{a}^n|\alpha\rangle=(\alpha^*)^m\alpha^n$. In practice, coherent states are routinely generated with a microwave source or, as in a recent experiment, with a maser at room temperature [80].

2.3.3 Squeezed states

In general, the quadratures of a squeezed state exhibit different uncertainties. In addition, an ideal squeezed state is a minimum-uncertainty state so that the product of its quadratures' variances is the same as the one of the vacuum. A squeezed state can be generated by applying the squeeze operator

$$\hat{S}(\xi) = \exp\left(\frac{1}{2}\xi^*\hat{a}^2 - \frac{1}{2}\xi(\hat{a}^\dagger)^2\right) \quad (2.18)$$

on the vacuum $|0\rangle$, where the complex squeezing parameter ξ is defined via the relation $\xi = re^{i\varphi}$. Here, the phase φ determines the direction and the squeeze factor r the amount of squeezing. In practice, an experimental realization of the squeeze operator demands a high non-linearity. As discussed in Sec. 3.2.1, we use a Josephson parametric amplifier in the phase-sensitive (degenerate) mode of operation to generate squeezed microwave states. Thereby, one quadrature of the input field is amplified whereas the other one is deamplified.

The Wigner function of a squeezed state is given by the expression

$$W(q, p) = \frac{2}{\pi} \exp\left[-(e^{2r}+e^{-2r})|q+ip|^2 - \frac{1}{2}(e^{2r}-e^{-2r})e^{-i\varphi}(q+ip)^2 - \frac{1}{2}(e^{2r}-e^{-2r})e^{i\varphi}(q-ip)^2\right]. \quad (2.19)$$

We simplify this formula by moving into a coordinate system rotated by the angle $\varphi/2$. Applying the transformation $q' + ip' = e^{-i\varphi/2}(q + ip)$ results in the expression

$$W(q', p') = \frac{2}{\pi} \exp\left[-2(q'^2 e^{2r} + p'^2 e^{-2r})\right]. \quad (2.20)$$

Consequently, the $1/e$ -contour forms an ellipse,

$$\frac{q'^2}{e^{-2r}} + \frac{p'^2}{e^{2r}} = \frac{1}{2}. \quad (2.21)$$

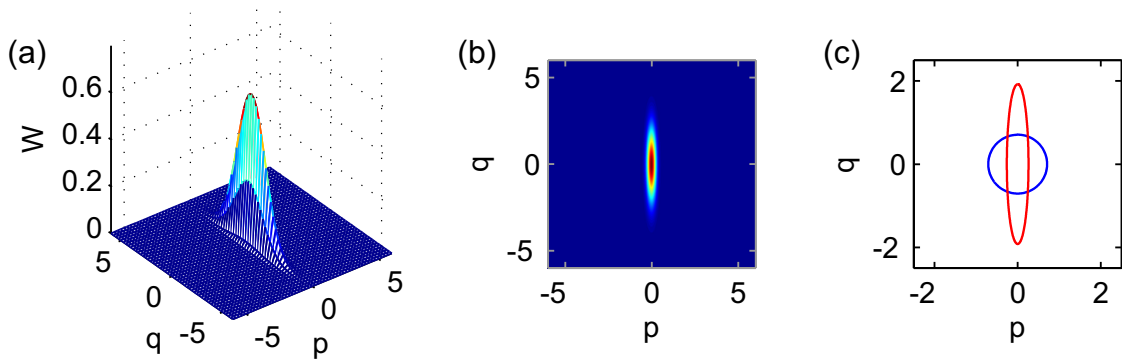


Figure 2.3: Wigner function of a squeezed state with $r=1$ and $\gamma = 90^\circ$. (a) Mesh plot. (b) Color map plot. (c) $1/e$ -contours of Wigner functions of the vacuum (blue) and of the squeezed state (red), whose q quadrature is squeezed 8.7 dB below the vacuum.

The lengths of the semi-major and semi-minor axis are given by $e^r/\sqrt{2}$ and $e^{-r}/\sqrt{2}$, respectively (cf. Fig. 2.3 for an example).

From the knowledge of the signal moments up to second order, we can readily extract the squeezing below the vacuum in decibel,

$$10 \log_{10} \left(-\langle \hat{a}^2 \rangle e^{-i\phi} - \langle (\hat{a}^\dagger)^2 \rangle e^{i\phi} + 2\langle \hat{a}^\dagger \hat{a} \rangle + 1 + \langle \hat{a} \rangle^2 e^{-i\phi} + \langle \hat{a}^\dagger \rangle^2 e^{i\phi} - 2\langle \hat{a}^\dagger \rangle \langle \hat{a} \rangle \right). \quad (2.22)$$

Here, the angle ϕ is defined via the relation $\langle \hat{a}^2 \rangle - \langle \hat{a} \rangle^2 = |\langle \hat{a}^2 \rangle - \langle \hat{a} \rangle^2| e^{i\phi}$ and the argument of the logarithm is the ratio between the variance of the squeezed quadrature and the vacuum variance. The angle ϕ is related to the phase of squeeze operator by the expression $\phi = \varphi + \pi$. Finally, we want to note that we use the angle $\gamma = -\phi/2 + \pi/2 = -\varphi/2$ between the anti-squeezed quadrature and the p -axis in phase space in the discussion of our results, since the semi-major axis of the ellipse is visually more prominent [cf. Fig. 2.3(b) and (c)].

2.3.4 Squeezed coherent states

For the generation of squeezed coherent states, two approaches exist. First, one can displace a squeezed vacuum state by applying the displacement operator after the squeeze operator. Second, we obtain a squeezed coherent state by first applying the displacement operator $\hat{D}(\alpha)$ to the vacuum followed by the squeeze operator $\hat{S}(\xi)$ [64]. In the latter case, the squeezed coherent state is defined as

$$|\alpha, \xi\rangle = \hat{S}(\xi) \hat{D}(\alpha) |0\rangle, \quad (2.23)$$

where $\alpha = |\alpha|e^{i\Theta}$ and $\xi = re^{i\varphi}$. The expectation values of the annihilation and creation operator moments up to second order are calculated as [64]

$$\langle \hat{a} \rangle = \alpha \cosh r - \alpha^* e^{i\varphi} \sinh r, \quad (2.24)$$

$$\langle \hat{a}^\dagger \rangle = \langle \hat{a} \rangle^*, \quad (2.25)$$

$$\begin{aligned} \langle \hat{a}^2 \rangle &= \alpha^2 \cosh^2 r + (\alpha^*)^2 e^{2i\varphi} \sinh^2 r \\ &\quad - 2|\alpha|^2 e^{i\varphi} \sinh r \cosh r - e^{i\varphi} \cosh r \sinh r, \end{aligned} \quad (2.26)$$

$$\langle (\hat{a}^\dagger)^2 \rangle = \langle \hat{a}^2 \rangle^*, \quad (2.27)$$

$$\begin{aligned} \langle \hat{a}^\dagger \hat{a} \rangle &= |\alpha|^2 (\cosh^2 r + \sinh^2 r) - (\alpha^*)^2 e^{i\varphi} \sinh r \cosh r \\ &\quad - \alpha^2 e^{-i\varphi} \sinh r \cosh r + \sinh^2 r. \end{aligned} \quad (2.28)$$

In the coordinate system aligned with the squeezed and anti-squeezed axes, the product of the quadrature variances attains the minimal value allowed by the Heisenberg uncertainty relation (2.3). Thus, the squeezed coherent state is an ideal squeezed state. Figure 2.4 shows the $1/e$ -contour line of the Wigner function for selected squeezed coherent states. Looking at the centers of the squeezed coherent states, we observe that the position of the squeezed coherent state depends on the squeeze angle [cf. Eq. (2.24)]. This can be intuitively understood by the fact that in the process of squeezing the coherent state is amplified in the anti-squeezed direction and deamplified in the squeezed direction.

In Tab. 2.1, we give an overview on some quantities of the states relevant in this work. If the variance of the photon number fluctuations $\langle (\Delta \hat{n})^2 \rangle$ is equal to the mean photon number, the state obeys Poissonian statistics. An example for this is

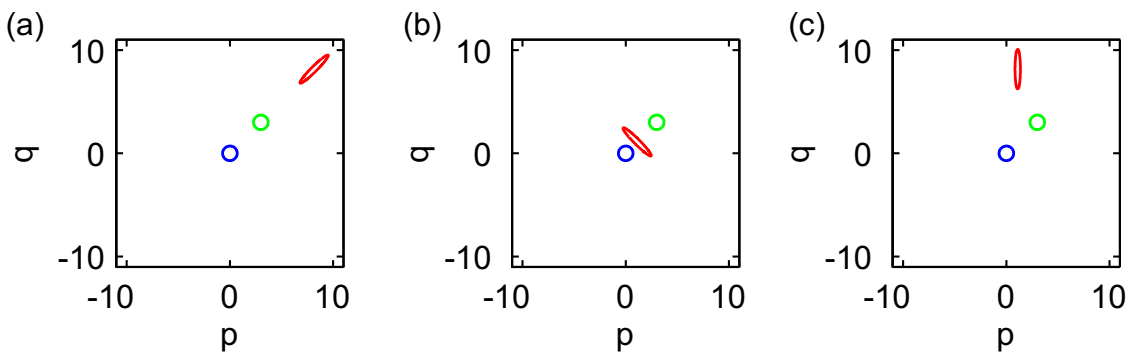


Figure 2.4: Squeezed coherent states with various squeeze angles φ . $1/e$ -contour lines for the Wigner functions of the vacuum $|0\rangle$ (blue), the coherent state $\hat{D}(3+3i)|0\rangle$ (green), and the squeezed coherent state $\hat{S}(1e^{i\varphi})\hat{D}(3+3i)|0\rangle$ (red). (a) $\varphi = 3\pi/2$. (b) $\varphi = \pi/2$. (c) $\varphi = \pi$.

| quantity | vacuum state | thermal state | coherent state | squeezed vacuum state |
|--------------------------------------|---------------|---|---------------------------|---|
| $\langle \hat{n} \rangle$ | 0 | $\frac{1}{\exp\left(\frac{hf}{k_B T}\right) - 1}$ | $ \alpha ^2$ | $\sinh^2 r$ |
| $\langle \hat{q} \rangle$ | 0 | 0 | $\Re(\alpha)$ | 0 |
| $\langle \hat{p} \rangle$ | 0 | 0 | $\Im(\alpha)$ | 0 |
| $\langle (\Delta \hat{n})^2 \rangle$ | 0 | $\langle \hat{n} \rangle^2 + \langle \hat{n} \rangle$ | $\langle \hat{n} \rangle$ | $2(\langle \hat{n} \rangle^2 + \langle \hat{n} \rangle)$ |
| $\langle (\Delta \hat{q})^2 \rangle$ | $\frac{1}{4}$ | $\frac{\langle \hat{n} \rangle}{2} + \frac{1}{4}$ | $\frac{1}{4}$ | $\frac{e^{2r}}{4} \sin^2 \frac{\varphi}{2}$ $+ \frac{e^{-2r}}{4} \cos^2 \frac{\varphi}{2}$ |
| $\langle (\Delta \hat{p})^2 \rangle$ | $\frac{1}{4}$ | $\frac{\langle \hat{n} \rangle}{2} + \frac{1}{4}$ | $\frac{1}{4}$ | $\frac{e^{2r}}{4} \cos^2 \frac{\varphi}{2}$ $+ \frac{e^{-2r}}{4} \sin^2 \frac{\varphi}{2}$ |

Table 2.1: Summary of state properties. \Re and \Im denote the real and imaginary part, respectively.

a coherent state. The state is of super-Poissonian statistics if the photon number variance attains a larger value than its mean photon number. This is the case for thermal and squeezed vacuum states. For a squeezed vacuum state, the value of $\langle (\Delta \hat{n})^2 \rangle$ is twice that of a thermal state with the same photon number.

2.4 Detection of microwave quantum correlations

In the optical domain, efficient single-photon detectors and optical homodyning are established measurement techniques to investigate quantum correlations [49]. However, despite theoretical [50–52] and recent experimental efforts [53–55], the translation of these methods to the microwave regime remains difficult because of the low photon energy. Thus, quantum state reconstruction of weak propagating microwaves to date requires the use of linear amplifiers. The properties of the latter allow us to distinguish between two fundamentally different approaches for the

reconstruction of microwave states. In the first class of methods, off-the-shelf noisy linear amplifiers are used and both quadratures are simultaneously measured. The latter demands for an equal treatment of both quadratures which is the characteristics of phase-insensitive amplifiers. These are obliged to add at least half a photon of noise to the signal [81]. Current implementations do not reach this standard quantum limit and add on the order of 10–20 noise photons at approximately 6 GHz. In our method, effects of this unavoidable noise contribution are canceled with the help of signal recovery techniques. This technique provides access to the undisturbed signal moments, from which the Wigner function is reconstructed. In the second class, phase-sensitive Josephson parametric amplifiers allow for an almost noiseless detection of a single generalized quadrature q_θ [56]. Since only one quadrature is accessible the marginal distributions of q_θ have to be collected for a set of angles forming a so called tomogram. From the latter the Wigner function is retrieved by applying an inverse Radon transformation [49] or maximum likelihood reconstruction. We note that the relations between tomogram and moments have been investigated in Ref. [78].

In this work, we concentrate on methods of the first class since the operation of off-the-shelf amplifiers is technically straight forward and promising. Furthermore, the noise properties of cryogenic HEMT amplifiers have been continuously improved. Therefore, we have proposed and experimentally implemented the dual-path method for quantum microwave reconstruction based on two independent amplification paths and cross-correlation techniques [57]. Subsequently, this detection scheme was extended to determine $g^{(2)}$ intensity correlations of the quantum states by another group [13]. Later, a different reconstruction technique using only a single amplification path and deconvolution based on a reference measurement was demonstrated [28]. We will introduce an extension of this method in Sec. 2.9 and use it for the detection of entanglement between signals propagating along separated paths (cf. Sec. 5.4). In what follows, we describe the mathematical details on the dual-path method both for the classical and quantum case.

2.5 Dual-path state reconstruction – classical treatment

In this section, we follow closely our work [57] and introduce the dual-path state reconstruction scheme which, even in the presence of significant amplifier noise, allows one to measure, in principle, all amplitude moments of propagating microwaves

based on cross-correlations from a dual-path amplification setup. Simultaneously, the detector noise properties are determined, allowing for tomography. Here, we use a classical description whereas in the next section we will dedicate ourselves to a straightforward extension of this theory to the quantum regime.

The reconstruction of the Wigner function [49] or density matrix of a propagating quantum field represents a cornerstone in quantum optical measurement theory and experiments. In quantum-optical homodyne tomography [47, 49], for example, the signal is combined with a local oscillator in a beam splitter and the intensities at the output ports are subtracted to produce the measurement of the amplified field quadratures in terms of a histogram. The latter gives access to all quadrature moments, or, equivalently, the Wigner function [49]. In quantum-optical homodyne tomography experiments [47], the signals at the beam splitter output pass directly to efficient photodetectors without the need of linear amplification¹. In contrast, in the 1–10 GHz range, which has become highly relevant due to the advent of circuit quantum electrodynamics (QED) [12, 14, 17, 18, 29, 82–85], the detection of few-photon microwave signals requires linear amplification. Within well-established off-the-shelf technology, cryogenic high electron mobility transistor (HEMT) amplifiers lend themselves to this purpose. They offer flat gain over a broad frequency range, but they obscure the signals by adding random noise [81, 86] of 10–20 photons at 5 GHz. Nevertheless, we here prove that it is still possible to measure all moments of few-photon propagating microwaves in this situation. Furthermore, we show that our proposed reconstruction method also produces a measurement of all moments of the detector noise. In this sense, moving from a single amplification chain to a dual-path configuration constitutes a step beyond pure state reconstruction and towards the complete calibration of the measurement device, i.e., detector tomography [87]. We note that previous to our work only state reconstruction of the intra-cavity field has been demonstrated in circuit QED [14]. However, quantum states of propagating microwaves themselves can be valuable in quantum information processing [88] and their full reconstruction represents an important issue.

In the following, we develop a theory for the measurement of all moments of both a propagating quantum microwave signal and the noise added by the detector. The basic idea is illustrated in Fig. 2.5. A signal a is equally split at low temperatures by means of a four-port 50-50 microwave beam splitter. The functionality of the latter is well-established for classical signals and was recently demonstrated also

¹We note that the extension of an optical homodyning scheme with phase-insensitive linear amplifiers does not allow for the detection of quantum states.

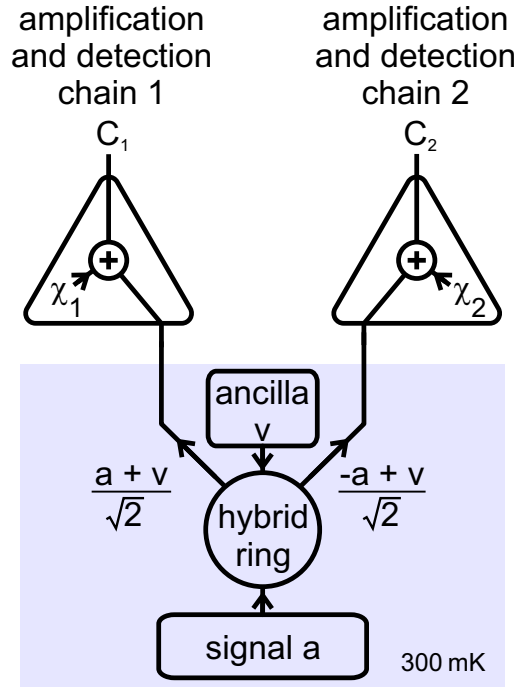


Figure 2.5: Schematics of the dual-path amplification and detection setup. The ancilla port of the 180° -hybrid ring is terminated by a $50\ \Omega$ -load at $T = 300\ \text{mK}$. The split signals are amplified and detected in separate chains (rounded triangular symbols), which add the noise χ_1 and χ_2 to the signal. Reprinted adopted figure with permission from Ref. [57]. Copyright (2010) by the American Physical Society.

for the quantum regime [13, 57, 58]. The beam splitter outputs are amplified and synchronously digitized. During this process, the amplifiers add the independent noise contributions χ_1 and χ_2 to the split signals in the detection chains 1 and 2, respectively. Assuming a 180° -hybrid ring [58, 89] as a beam splitter (cf. Sec. 3.1.2), the recorded time traces are

$$\begin{aligned}
 C_1 &= \sqrt{\frac{\tilde{G}}{2}}(a + v + \sqrt{2}\chi_1) = \sqrt{G}(a + v + V_1) \quad \text{and} \\
 C_2 &= \sqrt{\frac{\tilde{G}}{2}}(-a + v + \sqrt{2}\chi_2) = \sqrt{G}(-a + v + V_2), \quad (2.29)
 \end{aligned}$$

where $\chi_{1,2}$ are the noise contributions added by the amplification and detection chains and \tilde{G} their power gain, both referred to the input of the chains. Referred to the input of the beam splitter these variables are given by $V_{1,2} = \sqrt{2}\chi_{1,2}$ and $G = \tilde{G}/2$. Other choices for the beam splitter such as Wilkinson power dividers are possible as long as they provide enough isolation between the output ports.

The equivalent of Eqs. (2.29) can in principle be calculated for any beam splitter. The ancilla state present in the fourth port of the hybrid ring is called v . Since we assume full knowledge of v , an obvious choice for the ancilla is the vacuum or a weak thermal state. Vacuum or thermal states at gigahertz frequencies are prepared reliably in an experiment by controlling the temperature [58, 90]. We note that the moments of the ancilla state can not be detected by our method, which is not a restriction in practice. In the next step, we compute suitable correlations of the form $\langle C_1^\ell C_2^m \rangle$, where ℓ, m are non-negative integers and the brackets denote ensemble averaging. In contrast to Hanbury Brown–Twiss experiments based on intensity (power) correlations [90], our method is devoted to the correlations of field quadratures (voltages). For the first signal moment, the mean values $\langle V_1 \rangle$ and $\langle V_2 \rangle$ vanish and one obtains $\langle a \rangle = \langle C_1 \rangle / \sqrt{G} - \langle v \rangle = -\langle C_2 \rangle / \sqrt{G} - \langle v \rangle$. All higher moments of signal and noise can now be calculated by induction:

$$\begin{aligned} \langle a^n \rangle &= - \langle C_1^{n-1} C_2 \rangle / G^{n/2} \\ &\quad - \sum_{k=1}^{n-1} \sum_{j=0}^k \binom{n-1}{k} \binom{k}{j} \langle a^{n-k} \rangle \langle v^j \rangle \langle V_1^{k-j} \rangle \\ &\quad + \sum_{k=0}^{n-1} \sum_{j=0}^k \binom{n-1}{k} \binom{k}{j} \langle a^{n-k-1} \rangle \langle v^{j+1} \rangle \langle V_1^{k-j} \rangle, \end{aligned} \quad (2.30)$$

$$\begin{aligned} \langle V_1^n \rangle &= + \langle C_1^n \rangle / G^{n/2} \\ &\quad - \sum_{k=1}^n \sum_{j=0}^k \binom{n}{k} \binom{k}{j} \langle V_1^{n-k} \rangle \langle a^{k-j} \rangle \langle v^j \rangle, \end{aligned} \quad (2.31)$$

$$\begin{aligned} \langle V_2^n \rangle &= + \langle C_2^n \rangle / G^{n/2} \\ &\quad - \sum_{k=1}^n \sum_{j=0}^k \binom{n}{k} \binom{k}{j} (-1)^{k-j} \langle V_2^{n-k} \rangle \langle a^{k-j} \rangle \langle v^j \rangle. \end{aligned} \quad (2.32)$$

We note that our assumption of equal gain in both chains and a perfect 180°-hybrid ring is not a restriction in practice. In the derivation of the above formulas, the mutual statistical independence of a , v , V_1 , and V_2 is crucial because it implies $\langle a^\beta v^\gamma V_1^\delta V_2^\epsilon \rangle = \langle a^\beta \rangle \langle v^\gamma \rangle \langle V_1^\delta \rangle \langle V_2^\epsilon \rangle$ for non-negative integers $\beta, \gamma, \delta, \epsilon$. The latter formula also shows that Eqs. (2.30), (2.31), and (2.32) are suitable for quantum signals, where a , v , V_1 and V_2 have to be interpreted as operators (cf. Sec. 2.6).

Explicit expressions for moments of signal and detector noise are calculated from Eqs. (2.30), (2.31), and (2.32). We assume $\langle v^{2j+1} \rangle = 0$ (j being a non-negative integer) for the ancilla as in the case of vacuum or thermal states. We note that for

the initial correlation $\langle C_1^\ell C_2^m \rangle$ choices other than $\ell = n-1$ and $m = 1$ are possible, as long as $\ell+m = n$ for positive integers ℓ, m . Typically, balanced products with $\ell \approx m$ result in simpler expressions because of higher symmetry. Starting from $\langle C_1 C_2 \rangle$, $\langle C_1^2 C_2 \rangle$, and $\langle C_1^2 C_2^2 \rangle$, we obtain:

$$\begin{aligned} G^{1/2} \langle a \rangle &= \langle C_1 \rangle = -\langle C_2 \rangle, \\ G \langle a^2 \rangle &= -\langle C_1 C_2 \rangle + G \langle v^2 \rangle, \\ G^{3/2} \langle a^3 \rangle &= -\langle C_1^2 C_2 \rangle - \langle C_1 \rangle (\langle C_1^2 \rangle + \langle C_1 C_2 \rangle - 3G \langle v^2 \rangle), \\ G^2 \langle a^4 \rangle &= -G^2 \langle v^4 \rangle - 6G \langle v^2 \rangle \langle C_1 C_2 \rangle + 6G^2 \langle v^2 \rangle^2 \\ &\quad + \langle C_1 C_2 \rangle^2 + \langle C_1^2 C_2^2 \rangle - \langle C_1^2 \rangle \langle C_2^2 \rangle, \end{aligned}$$

$$\begin{aligned} \langle V_1 \rangle &\equiv 0, \\ G \langle V_1^2 \rangle &= \langle C_1^2 \rangle + \langle C_1 C_2 \rangle - 2G \langle v^2 \rangle, \\ G^{3/2} \langle V_1^3 \rangle &= \langle C_1^3 \rangle + \langle C_1^2 C_2 \rangle - 2\langle C_1 \rangle (\langle C_1^2 \rangle + \langle C_1 C_2 \rangle), \\ G^2 \langle V_1^4 \rangle &= \langle C_1^4 \rangle - 12G \langle v^2 \rangle \langle C_1 C_2 \rangle - 12G \langle v^2 \rangle \langle C_1^2 \rangle \\ &\quad + 6\langle C_1 C_2 \rangle \langle C_1^2 \rangle + 5\langle C_1 C_2 \rangle^2 + 12G^2 \langle v^2 \rangle^2 \\ &\quad - 4\langle C_1 \rangle \langle C_1^3 \rangle - 4\langle C_1 \rangle \langle C_1^2 C_2 \rangle + 8\langle C_1 \rangle^2 \langle C_1^2 \rangle \\ &\quad + 8\langle C_1 \rangle^2 \langle C_1 C_2 \rangle - \langle C_1^2 C_2^2 \rangle + \langle C_1^2 \rangle \langle C_2^2 \rangle. \end{aligned}$$

Similar formulas are derived for V_2 . Furthermore, we assume the first moment of the detector noise to vanish for both chains throughout the experimental part of this work. Practically, this implies an offset correction (cf. Sec. 3.1.3). Finally, the central moments are retrieved from the binomial transformation

$$\langle (a - \langle a \rangle)^n \rangle = \sum_{k=0}^n \binom{n}{k} (-1)^{n-k} \langle a^k \rangle \langle a \rangle^{n-k}. \quad (2.33)$$

2.6 Dual-path state reconstruction – quantum treatment

As our object of study is inherently quantum, we need to extend the formalism of the dual-path method presented in the last section to the quantum regime. This extension has been in large part developed by Roberto Di Candia. For quantum microwaves, we need to take into account the orthogonal signal quadratures $I_{1,2}$ and $Q_{1,2}$ measured at the outputs of IQ mixers. We now define the dimensionless

complex envelope functions

$$\xi_{1,2} \equiv (I_{1,2} + iQ_{1,2})/\sqrt{\kappa}, \quad (2.34)$$

where κ is the photon number conversion factor introduced in Sec. 3.3.4. The corresponding operators,

$$\hat{\xi}_{1,2} \equiv (\hat{I}_{1,2} + i\hat{Q}_{1,2})/\sqrt{\kappa}, \quad (2.35)$$

can, in this situation, be expressed as [42]

$$\hat{\xi}_{1,2} = \hat{O}_{1,2} + \hat{v}_{1,2}^\dagger. \quad (2.36)$$

Here, $\hat{O}_{1,2}$ is the bosonic annihilation operator of the input signal into the IQ mixer. The noise added by the latter is represented by its bosonic creation operator $\hat{v}_{1,2}^\dagger$. We now have $[\hat{\xi}_{1,2}, \hat{\xi}_{1,2}^\dagger] = 0$, and the correlations $\langle \hat{\xi}_1^{j'} (\hat{\xi}_1^\dagger)^{m'} \hat{\xi}_2^{k'} (\hat{\xi}_2^\dagger)^{n'} \rangle = \langle (\hat{\xi}_1^\dagger)^{m'} \hat{\xi}_1^{j'} (\hat{\xi}_2^\dagger)^{n'} \hat{\xi}_2^{k'} \rangle$ can be expressed in terms of the measured $\langle I_1^j I_2^k Q_1^m Q_2^n \rangle$ via Eq. (2.34) by identifying $\hat{\xi}_{1,2}$ with $\xi_{1,2}$ and $\hat{\xi}_{1,2}^\dagger$ with $\xi_{1,2}^*$. We note that, while in general, $j', k', m', n', j, k, m, n \in \mathbb{N}_0$, in this work we restrict ourselves to $j + k + m + n \leq 4$ or, equivalently, $j' + k' + m' + n' \leq 4$. Using the beam splitter relations and the standard quantum model for linear amplifiers [81], we now write

$$\hat{\xi}_1 = \sqrt{\frac{G_{d1}}{2}} (+\hat{a} + \hat{v}) + \sqrt{G_{d1} - 1} \hat{h}_1^\dagger + \hat{v}_1^\dagger \quad (2.37)$$

$$\hat{\xi}_2 = \sqrt{\frac{G_{d2}}{2}} (-\hat{a} + \hat{v}) + \sqrt{G_{d2} - 1} \hat{h}_2^\dagger + \hat{v}_2^\dagger \quad (2.38)$$

for our setup. Here, \hat{a} and \hat{v} are bosonic annihilation operators. They describe the modes incident on the signal and the $50\ \Omega$ -terminated input port of the beam splitter, respectively. The noise fields added by each amplification path are represented by the bosonic creation operators $\hat{h}_{1,2}^\dagger$. Their effective temperature is mainly determined by the noise temperatures of the cold HEMT amplifiers and the cable losses between beam splitter and HEMT amplifier. $G_{d1,2}$ are the gains of the output paths, which are calibrated as described in Sec. 3.3.4. In order to simplify the notation, we also define the operators

$$\hat{V}_{1,2} \equiv \sqrt{\frac{2}{G_{d1,2}}} \left(\sqrt{G_{d1,2} - 1} \hat{h}_{1,2}^\dagger + \hat{v}_{1,2}^\dagger \right) \quad (2.39)$$

$$\hat{S}_{1,2} \equiv \sqrt{\frac{2}{G_{d1,2}}} \hat{\xi}_{1,2}. \quad (2.40)$$

We note that $\hat{V}_{1,2}/\sqrt{2}$ is a bosonic operator, as $[\hat{V}_{1,2}/\sqrt{2}, \hat{V}_{1,2}^\dagger/\sqrt{2}] = 1$. In this way, we arrive at the simple expressions

$$\hat{S}_1 = +\hat{a} + \hat{v} + \hat{V}_1^\dagger \quad (2.41)$$

$$\hat{S}_2 = -\hat{a} + \hat{v} + \hat{V}_2^\dagger. \quad (2.42)$$

Here, the operators $\hat{V}_{1,2}$, \hat{a} , and \hat{v} , and therefore also $\hat{S}_{1,2}$, are referred to the input of the beam splitter. With these definitions, we can generalize the dual-path state reconstruction technique (cf. Sec. 2.5) in a way that it becomes applicable to quadratures. Making the reasonable assumptions that \hat{v} is a weak thermal state with a measured temperature of 40 mK and that

$$\langle \hat{V}_1 \rangle = \langle \hat{V}_2 \rangle = 0 \quad (2.43)$$

for the noise added by the amplification paths, we recursively obtain the signal moments

$$\begin{aligned} \langle (\hat{a}^\dagger)^l \hat{a}^m \rangle_{l_1, m_1} &= (-1)^{l-l_1+m-m_1} \langle (\hat{S}_1^\dagger)^{l_1} (\hat{S}_2^\dagger)^{l-l_1} \hat{S}_1^{m_1} \hat{S}_2^{m-m_1} \rangle \\ &- \sum_{k_1=0}^{l_1} \sum_{k_2=0}^{l-l_1} \sum_{j_1=0}^{m_1} \sum_{j_2=0}^{m-m_1-1} \sum_{k'_1=0}^{l_1-k_1} \sum_{k'_2=0}^{l-l_1-k_2} \sum_{j'_1=0}^{m_1-j_1} \sum_{j'_2=0}^{m-m_1-j_2} \binom{l_1}{k_1} \binom{l-l_1}{k_2} \binom{m_1}{j_1} \binom{m-m_1}{j_2} \\ &\times \binom{l_1-k_1}{k'_1} \binom{l-l_1-k_2}{k'_2} \binom{m_1-j_1}{j'_1} \binom{m-m_1-j_2}{j'_2} (-1)^{l-l_1+m-m_1+j_2+k_2} \\ &\times \langle (\hat{a}^\dagger)^{k_1+k_2} \hat{a}^{j_1+j_2} \rangle \langle (\hat{v}^\dagger)^{k'_1+k'_2} \hat{v}^{j'_2+j'_1} \rangle \langle \hat{V}_1^{l_1-k_1-k'_1} (\hat{V}_1^\dagger)^{m_1-j_1-j'_1} \rangle \\ &\times \langle \hat{V}_2^{l-l_1-k_2-k'_2} (\hat{V}_2^\dagger)^{m-m_1-j_2-j'_2} \rangle \\ &- \sum_{k_1=0}^{l_1} \sum_{k_2=0}^{l-l_1} \sum_{j_1=0}^{m_1-1} \sum_{k'_1=0}^{l_1-k_1} \sum_{k'_2=0}^{l-l_1-k_2} \sum_{j'_1=0}^{m_1-j_1} \binom{l_1}{k_1} \binom{l-l_1}{k_2} \binom{m_1}{j_1} \binom{l_1-k_1}{k'_1} \binom{l-l_1-k_2}{k'_2} \\ &\times \binom{m_1-j_1}{j'_1} (-1)^{l-l_1+k_2} \langle (\hat{a}^\dagger)^{k_1+k_2} \hat{a}^{j_1+m-m_1} \rangle \langle (\hat{v}^\dagger)^{k'_1+k'_2} \hat{v}^{j'_1} \rangle \\ &\times \langle \hat{V}_1^{l_1-k_1-k'_1} (\hat{V}_1^\dagger)^{m_1-j_1-j'_1} \rangle \langle \hat{V}_2^{l-l_1-k_2-k'_2} \rangle \\ &- \sum_{k_1=0}^{l_1} \sum_{k_2=0}^{l-l_1-1} \binom{l_1}{k_1} \binom{l-l_1}{k_2} (-1)^{l-l_1+k_2} \langle (\hat{a}^\dagger)^{k_1+k_2} \hat{a}^m \rangle \langle \hat{V}_1^{l_1-k_1} \rangle \langle \hat{V}_2^{l-l_1-k_2} \rangle \\ &- \sum_{k_1=0}^{l_1-1} \binom{l_1}{k_1} \langle (\hat{a}^\dagger)^{k_1+l-l_1} \hat{a}^m \rangle \langle \hat{V}_1^{l_1-k_1} \rangle \end{aligned} \quad (2.44)$$

for $l, m, l_1, m_1 \in \mathbb{N}_0$ from the measured noisy correlations. In this process, we also

have to compute the noise moments

$$\begin{aligned}
\langle \hat{V}_1^r (\hat{V}_1^\dagger)^s \rangle &= \langle (\hat{S}_1^\dagger)^r \hat{S}_1^s \rangle \\
&- \sum_{k_1=0}^r \sum_{j_1=0}^{s-1} \sum_{k'_1=0}^{r-k_1} \sum_{j'_1=0}^{s-j_1} \binom{r}{k_1} \binom{s}{j_1} \binom{r-k_1}{k'_1} \binom{s-j_1}{j'_1} \langle (\hat{a}^\dagger)^{k'_1} \hat{a}^{j'_1} \rangle \langle (\hat{v}^\dagger)^{r-k_1-k'_1} \hat{v}^{s-j_1-j'_1} \rangle \\
&\quad \times \langle \hat{V}_1^{k_1} (\hat{V}_1^\dagger)^{j_1} \rangle \\
&- \sum_{k_1=0}^{r-1} \binom{r}{k_1} \langle (\hat{a}^\dagger)^{r-k_1} \rangle \langle \hat{V}_1^{k_1} (\hat{V}_1^\dagger)^s \rangle
\end{aligned} \tag{2.45}$$

and

$$\begin{aligned}
\langle \hat{V}_2^r (\hat{V}_2^\dagger)^s \rangle &= \langle (\hat{S}_2^\dagger)^r \hat{S}_2^s \rangle \\
&- \sum_{k_1=0}^r \sum_{j_1=0}^{s-1} \sum_{k'_1=0}^{r-k_1} \sum_{j'_1=0}^{s-j_1} \binom{r}{k_1} \binom{s}{j_1} \binom{r-k_1}{k'_1} \binom{s-j_1}{j'_1} (-1)^{k'_1+j'_1} \langle (\hat{a}^\dagger)^{k'_1} \hat{a}^{j'_1} \rangle \\
&\quad \times \langle (\hat{v}^\dagger)^{r-k_1-k'_1} \hat{v}^{s-j_1-j'_1} \rangle \langle \hat{V}_2^{k_1} (\hat{V}_2^\dagger)^{j_1} \rangle \\
&- \sum_{k_1=0}^{r-1} \binom{r}{k_1} (-1)^{r-k_1} \langle (\hat{a}^\dagger)^{r-k_1} \rangle \langle \hat{V}_2^{k_1} (\hat{V}_2^\dagger)^s \rangle
\end{aligned} \tag{2.46}$$

associated with both amplification paths for $r + s > 1$ and $r, s \in \mathbb{N}_0$, again in a recursive fashion. In other words, the formulas for the moments of order $l + m$ are established using those of the moments of order $l + m - 1$. The formulas obtained in this way are not unique, they depend on the specific choices of l_1 and m_1 . We find that the statistical uncertainty in our results is minimized by using the mean value of all formulas found for constant $l + m$.

We end this section with a remark regarding the difference in notation between the classical and quantum treatment. In the classical description the power of the ancilla state fluctuations is given by $\langle v^2 \rangle$ whereas in the quantum-mechanical description $\langle \hat{v}^\dagger \hat{v} \rangle$ is the correct expression. Thus, one cannot simply replace v by \hat{v} in the formulas of the classical treatment to retrieve the quantum-mechanical expressions. Nevertheless, we emphasize that the fundamental strategy of the dual-path state reconstruction is completely analogous for weak classical and quantum signals.

2.7 Wigner function reconstruction

In the case of infinitely many reconstructed moments $\langle (\hat{a}^\dagger)^l \hat{a}^m \rangle$, the Wigner function $W(q, p)$ of an arbitrary state can be completely reconstructed. However, in

this work we record these moments only up to fourth order, $l + m \leq 4$. As we find that the higher moments are consistent with those of Gaussian states, we are allowed to restrict ourselves to moments with $l + m \leq 2$. In Ref. [76] and Ref. [91], Bužek *et al.* analyzed how the Wigner function of a quantum state can be partially reconstructed from a finite number of moments. For our observation level [92] $\mathcal{O}_2 \equiv \{\hat{a}^\dagger \hat{a}, (\hat{a}^\dagger)^2, \hat{a}^2, \hat{a}^\dagger, \hat{a}\}$ this analytic approach based on Jaynes principle [93, 94] of maximum entropy yields

$$W(q, p) = \frac{1}{\pi \sqrt{(\nu + 1/2)^2 - |\mu|^2}} \times \exp \left[-\frac{(\nu + 1/2)|\zeta - \langle \hat{a} \rangle|^2 - (\mu^*/2)(\zeta - \langle \hat{a} \rangle)^2 - (\mu/2)(\zeta^* - \langle \hat{a}^\dagger \rangle)^2}{(\nu + 1/2)^2 - |\mu|^2} \right], \quad (2.47)$$

with $\zeta \equiv q + ip$, $\mu \equiv \langle \hat{a}^2 \rangle - \langle \hat{a} \rangle^2$, and $\nu \equiv \langle \hat{a}^\dagger \hat{a} \rangle - |\langle \hat{a} \rangle|^2$. As explained in Sec. 2.6, we have chosen our definitions such that phase space variables q and p are dimensionless and their value represents the square root of a photon number. Since any Gaussian state can be written as a displaced squeezed thermal state, we can also extract the effective mode temperature analytically from the reconstructed input state moments [76, 91]. We note that this effective temperature may contain contributions from the physical temperature as well as contributions from losses.

2.8 Path entanglement via a beam splitter

The generation of path entanglement is an important task, since the entanglement of signals propagating along different paths serves as a key resource in fascinating quantum information and communication protocols. Here, the exploitation of entanglement promises significant performance gains over classical implementations [3–5], since its presence can, for example, increase the channel capacity [95] and the channel efficiency [96]. In this section, we consider the generation of microwave path entanglement via a beam splitter. Kim *et al.* [60] have shown that a necessary prerequisite for this scheme is that at least one input state is non-classical. The action of a 50:50 beam splitter on a pure squeezed state and a vacuum state is given by [60]

$$\hat{B} \hat{S}_a(\xi) |0, 0\rangle = \hat{S}_a \left(\frac{\xi}{2} \right) \hat{S}_b \left(\frac{\xi}{2} \right) \hat{S}_{ab} \left(-\frac{\xi}{2} \right) |0, 0\rangle, \quad (2.48)$$

where $\hat{B} = \exp[\frac{\pi}{4}(\hat{a}\hat{b}^\dagger - \hat{a}^\dagger\hat{b})]$ is the beam splitter operator and $\hat{S}_{ab}(\xi) = \exp(-\xi\hat{a}\hat{b} + \xi^*\hat{a}^\dagger\hat{b}^\dagger)$ the two-mode squeeze operator. Thus, the resulting state is a two-mode squeezed state with two additional local squeeze operations. The latter have no influence on the degree of entanglement which therefore is given by that of an ideal two-mode squeezed state. Furthermore, in Ref. [60] the superposition of a squeezed thermal state and a vacuum via a beam splitter is investigated in theory. The results are of high relevance for our work because they imply that the thermal state has to be squeezed below the vacuum in order to retrieve an entangled output state.

2.9 Reference-state method for the detection of path entanglement

In order to detect the entanglement between the two paths independently from the dual-path reconstruction of the input state, we cannot assume that the hybrid ring is working as a beam splitter. We therefore follow a different route: we reconstruct the moments of the output state by means of a calibration against a well-known reference signal [28, 44]. The obvious choice for this reference signal is the two-mode vacuum. In this way, the beam splitter is treated as a black box device which, for a vacuum state at each input, produces uncorrelated vacuum states at each output port. This rather general assumption holds well for the temperatures measured for attenuator and termination, 40 – 50 mK. In this situation, the complex envelope operator becomes

$$\hat{\xi}_1 = \sqrt{G_{r1}} \hat{s}_1 + \sqrt{G_{r1} - 1} \hat{h}_1^\dagger + \hat{v}_1^\dagger \quad (2.49)$$

$$\hat{\xi}_2 = \sqrt{G_{r2}} \hat{s}_2 + \sqrt{G_{r2} - 1} \hat{h}_2^\dagger + \hat{v}_2^\dagger. \quad (2.50)$$

Here, $\hat{s}_{1,2}$ is referred to the output of the beam splitter, and $G_{r1,2}$ is the effective gain of the amplification paths. Note that the $G_{r1,2}$ in the reference-state formulas are numerically different from the gains $G_{d1,2}$ in the dual-path equations because they do not contain the beam splitter losses. After defining the operators

$$\hat{V}_{1,2} \equiv \sqrt{\frac{1}{G_{r1,2}}} \left(\sqrt{G_{r1,2} - 1} \hat{h}_{1,2} + \hat{v}_{1,2} \right) \quad (2.51)$$

$$\hat{S}_{1,2} \equiv \sqrt{\frac{1}{G_{r1,2}}} \hat{\xi}_{1,2}, \quad (2.52)$$

we again arrive at the simplified expressions

$$\hat{S}_1 = \hat{s}_1 + \hat{V}_1^\dagger \quad (2.53)$$

$$\hat{S}_2 = \hat{s}_2 + \hat{V}_2^\dagger. \quad (2.54)$$

We now evaluate the correlations between the two channels,

$$\begin{aligned} & \langle (\hat{S}_1^\dagger)^{l_1} \hat{S}_1^{m_1} (\hat{S}_2^\dagger)^{l_2} \hat{S}_2^{m_2} \rangle \\ &= \langle (\hat{s}_1^\dagger + \hat{V}_1^\dagger)^{l_1} (\hat{s}_1 + \hat{V}_1^\dagger)^{m_1} (\hat{s}_2^\dagger + \hat{V}_2^\dagger)^{l_2} (\hat{s}_2 + \hat{V}_2^\dagger)^{m_2} \rangle \\ &= \sum_{k_1=0}^{l_1} \sum_{k_2=0}^{l_2} \sum_{j_1=0}^{m_1} \sum_{j_2=0}^{m_2} \binom{l_1}{k_1} \binom{l_2}{k_2} \binom{m_1}{j_1} \binom{m_2}{j_2} \langle (\hat{s}_1^\dagger)^{l_1-k_1} \hat{s}_1^{m_1-j_1} (\hat{s}_2^\dagger)^{l_2-k_2} \hat{s}_2^{m_2-j_2} \rangle \\ & \quad \times \langle \hat{V}_1^{k_1} (\hat{V}_1^\dagger)^{j_1} \hat{V}_2^{k_2} (\hat{V}_2^\dagger)^{j_2} \rangle. \end{aligned} \quad (2.55)$$

With the terms $\langle (\hat{s}_1^\dagger)^{l_1-k_1} \hat{s}_1^{m_1-j_1} (\hat{s}_2^\dagger)^{l_2-k_2} \hat{s}_2^{m_2-j_2} \rangle$, which can be calculated straightforwardly for our reference state, Eq. (2.55) forms a system of linear equations. The latter allows us to extract the noise terms $\langle \hat{V}_1^{k_1} (\hat{V}_1^\dagger)^{j_1} \hat{V}_2^{k_2} (\hat{V}_2^\dagger)^{j_2} \rangle$ related to our amplification paths by algebraic inversion [28]. Once knowing these noise terms, we extract the signal correlations for the squeezed state input again from Eq. (2.55) and algebraic inversion. We note that also more sophisticated reference states and device models, such as thermal states incident at a beam splitter, can be chosen as reference state. Depending on the pre-characterization of the used components, this approach might account better for experimental imperfections. Although the latter typically tend to reduce the degree of entanglement, our entanglement detection turns out to be quite robust against them as discussed in Sec. 5.4.

Altogether, the method described above would, in principle, allow for a reconstruction of the output state as far as this is possible with four moments. We note that from such a reconstruction also all entanglement properties could be derived. However, as shown in Secs. 2.10 and 2.11, we choose a more robust approach for this purpose.

2.10 Entanglement witness

The detection of entanglement requires substantially less information than a full state reconstruction. Indeed, there exists an infinite number of witnesses and criteria which allow one to decide whether or not a state is entangled. Each of these criteria uses only a small amount of information about the examined state. In this work,

we use the witness matrix [97]

$$\mathbf{M}^{(2)} \equiv \begin{pmatrix} 1 & \langle \hat{s}_1 \rangle & \langle \hat{s}_1^\dagger \rangle & \langle \hat{s}_2^\dagger \rangle & \langle \hat{s}_2 \rangle \\ \langle \hat{s}_1^\dagger \rangle & \langle \hat{s}_1^\dagger \hat{s}_1 \rangle & \langle (\hat{s}_1^\dagger)^2 \rangle & \langle \hat{s}_1^\dagger \hat{s}_2^\dagger \rangle & \langle \hat{s}_1^\dagger \hat{s}_2 \rangle \\ \langle \hat{s}_1 \rangle & \langle \hat{s}_1^2 \rangle & 1 + \langle \hat{s}_1^\dagger \hat{s}_1 \rangle & \langle \hat{s}_1 \hat{s}_2^\dagger \rangle & \langle \hat{s}_1 \hat{s}_2 \rangle \\ \langle \hat{s}_2 \rangle & \langle \hat{s}_1 \hat{s}_2 \rangle & \langle \hat{s}_1^\dagger \hat{s}_2 \rangle & \langle \hat{s}_2^\dagger \hat{s}_2 \rangle & \langle \hat{s}_2^2 \rangle \\ \langle \hat{s}_2^\dagger \rangle & \langle \hat{s}_1 \hat{s}_2^\dagger \rangle & \langle \hat{s}_1^\dagger \hat{s}_2^\dagger \rangle & \langle (\hat{s}_2^\dagger)^2 \rangle & 1 + \langle \hat{s}_2^\dagger \hat{s}_2 \rangle \end{pmatrix}, \quad (2.56)$$

which contains up to second order moments of the beam splitter output state. If $\mathbf{M}^{(2)}$ has at least one negative eigenvalue, the state is entangled. The absence of a negative eigenvalue implies separability only in the case of Gaussian states.

2.11 Negativity

For a bipartite system, the amount of entanglement between the subsystems A and B can be quantified by means of the negativity

$$\mathcal{N}(\rho) \equiv \frac{\|\rho^{T_B}\|_1 - 1}{2}, \quad (2.57)$$

where ρ is the density matrix of the total system, and $\|\rho^{T_B}\|_1 = \text{Tr}|\rho^{T_B}|$ is the trace norm of the partial transpose of ρ with respect to subsystem B, ρ^{T_B} . If $\mathcal{N}(\rho) > 0$, the state is entangled. For a maximally entangled state, $\mathcal{N}(\rho) \rightarrow \infty$.

In the case of Gaussian states, all measures of entanglement are equivalent, and they are defined by the covariance matrix

$$\boldsymbol{\sigma} = \begin{pmatrix} \boldsymbol{\alpha} & \boldsymbol{\gamma} \\ \boldsymbol{\gamma}^T & \boldsymbol{\beta} \end{pmatrix}. \quad (2.58)$$

Here, we define the matrices

$$\boldsymbol{\alpha} \equiv \begin{pmatrix} \alpha_1 & \alpha_3 \\ \alpha_3 & \alpha_2 \end{pmatrix}, \boldsymbol{\beta} \equiv \begin{pmatrix} \beta_1 & \beta_3 \\ \beta_3 & \beta_2 \end{pmatrix}, \boldsymbol{\gamma} \equiv \begin{pmatrix} \gamma_{11} & \gamma_{12} \\ \gamma_{21} & \gamma_{22} \end{pmatrix} \quad (2.59)$$

with

$$\alpha_1 = \langle \hat{s}_1^2 \rangle + \langle (\hat{s}_1^\dagger)^2 \rangle + 2\langle \hat{s}_1^\dagger \hat{s}_1 \rangle - \langle \hat{s}_1 + \hat{s}_1^\dagger \rangle^2 + 1 \quad (2.60)$$

$$\alpha_2 = -\langle \hat{s}_1^2 \rangle - \langle (\hat{s}_1^\dagger)^2 \rangle + 2\langle \hat{s}_1^\dagger \hat{s}_1 \rangle + \langle \hat{s}_1 - \hat{s}_1^\dagger \rangle^2 + 1 \quad (2.61)$$

$$\alpha_3 = i(-\langle \hat{s}_1^2 \rangle + \langle (\hat{s}_1^\dagger)^2 \rangle + \langle \hat{s}_1 \rangle^2 - \langle \hat{s}_1^\dagger \rangle^2) \quad (2.62)$$

$$\beta_1 = \langle \hat{s}_2^2 \rangle + \langle (\hat{s}_2^\dagger)^2 \rangle + 2\langle \hat{s}_2^\dagger \hat{s}_2 \rangle - \langle \hat{s}_2 + \hat{s}_2^\dagger \rangle^2 + 1 \quad (2.63)$$

$$\beta_2 = -\langle \hat{s}_2^2 \rangle - \langle (\hat{s}_2^\dagger)^2 \rangle + 2\langle \hat{s}_2^\dagger \hat{s}_2 \rangle + \langle \hat{s}_2 - \hat{s}_2^\dagger \rangle^2 + 1 \quad (2.64)$$

$$\beta_3 = i(-\langle \hat{s}_2^2 \rangle + \langle (\hat{s}_2^\dagger)^2 \rangle + \langle \hat{s}_2 \rangle^2 - \langle \hat{s}_2^\dagger \rangle^2) \quad (2.65)$$

$$\begin{aligned} \gamma_{11} &= \langle \hat{s}_1 \hat{s}_2 + \hat{s}_1 \hat{s}_2^\dagger + \hat{s}_1^\dagger \hat{s}_2 + \hat{s}_1^\dagger \hat{s}_2^\dagger \rangle / 2 \\ &\quad + \langle \hat{s}_2 \hat{s}_1 + \hat{s}_2 \hat{s}_1^\dagger + \hat{s}_2^\dagger \hat{s}_1 + \hat{s}_2^\dagger \hat{s}_1^\dagger \rangle / 2 \\ &\quad - \langle \hat{s}_1 + \hat{s}_1^\dagger \rangle \langle \hat{s}_2 + \hat{s}_2^\dagger \rangle \end{aligned} \quad (2.66)$$

$$\begin{aligned} \gamma_{12} &= \langle \hat{s}_1 \hat{s}_2 - \hat{s}_1 \hat{s}_2^\dagger + \hat{s}_1^\dagger \hat{s}_2 - \hat{s}_1^\dagger \hat{s}_2^\dagger \rangle / 2i \\ &\quad + \langle \hat{s}_2 \hat{s}_1 + \hat{s}_2 \hat{s}_1^\dagger - \hat{s}_2^\dagger \hat{s}_1 - \hat{s}_2^\dagger \hat{s}_1^\dagger \rangle / 2i \\ &\quad + i \langle \hat{s}_1 + \hat{s}_1^\dagger \rangle \langle \hat{s}_2 - \hat{s}_2^\dagger \rangle \end{aligned} \quad (2.67)$$

$$\begin{aligned} \gamma_{21} &= \langle \hat{s}_1 \hat{s}_2 + \hat{s}_1 \hat{s}_2^\dagger - \hat{s}_1^\dagger \hat{s}_2 - \hat{s}_1^\dagger \hat{s}_2^\dagger \rangle / 2i \\ &\quad + \langle \hat{s}_2 \hat{s}_1 - \hat{s}_2 \hat{s}_1^\dagger + \hat{s}_2^\dagger \hat{s}_1 - \hat{s}_2^\dagger \hat{s}_1^\dagger \rangle / 2i \\ &\quad + i \langle \hat{s}_1 - \hat{s}_1^\dagger \rangle \langle \hat{s}_2 + \hat{s}_2^\dagger \rangle \end{aligned} \quad (2.68)$$

$$\begin{aligned} \gamma_{22} &= \langle -\hat{s}_1 \hat{s}_2 + \hat{s}_1 \hat{s}_2^\dagger + \hat{s}_1^\dagger \hat{s}_2 - \hat{s}_1^\dagger \hat{s}_2^\dagger \rangle / 2 \\ &\quad + \langle -\hat{s}_2 \hat{s}_1 + \hat{s}_2 \hat{s}_1^\dagger + \hat{s}_2^\dagger \hat{s}_1 - \hat{s}_2^\dagger \hat{s}_1^\dagger \rangle / 2 \\ &\quad + \langle \hat{s}_1 - \hat{s}_1^\dagger \rangle \langle \hat{s}_2 - \hat{s}_2^\dagger \rangle \end{aligned} \quad (2.69)$$

and γ^T being the transpose of γ . Finally, the negativity becomes [98]

$$\mathcal{N} = \max \left\{ 0, \frac{1 - \nu}{2\nu} \right\} \equiv \max \left\{ 0, \tilde{\mathcal{N}} \right\}, \quad (2.70)$$

where $\nu \equiv \sqrt{(\Delta(\boldsymbol{\sigma}) - \sqrt{\Delta^2(\boldsymbol{\sigma}) - 4 \det \boldsymbol{\sigma}}) / 2}$ and $\Delta(\boldsymbol{\sigma}) \equiv \det \boldsymbol{\alpha} + \det \boldsymbol{\beta} - 2 \det \boldsymbol{\gamma}$.

Note that, despite not being a measure, the negativity kernel $\tilde{\mathcal{N}}$ is a witness for arbitrary bipartite entanglement. In fact, if a non-Gaussian state has the same first and second moments as an entangled Gaussian state, it is entangled [99]. Consequently, $\tilde{\mathcal{N}} > 0$ implies entanglement for any bipartite state.

2.12 Gaussianity and higher order cumulants

In order to check whether the states we reconstruct are consistent with Gaussian states, we evaluate the $(l+m)^{\text{th}}$ order cumulants $\langle\langle (\hat{a}^l)^\dagger \hat{a}^m \rangle\rangle$ for $l+m \leq 4$ and $l, m \in \mathbb{N}_0$. Equivalently to the moments, the cumulants describe a probability distribution. The definition of cumulants for a quantum state with density matrix ρ

can be written as [100]

$$\langle\langle(\hat{a}^l)^\dagger \hat{a}^m\rangle\rangle \equiv \frac{\partial^l}{\partial(i\beta^*)^l} \frac{\partial^m}{\partial(i\beta)^m} \left[\frac{\beta\beta^*}{2} + \ln \text{Tr} \left(e^{(i\beta^*\hat{a}^\dagger + i\beta\hat{a})} \rho \right) \right]_{\beta, \beta^*=0}. \quad (2.71)$$

Only Gaussian states have a finite number of non-zero cumulants. More specifically, all their cumulants vanish for $l+m > 2$. In other words, finding a non-zero cumulant of 3rd or higher order implies that the state is not Gaussian. Despite not being a strict proof, the fact that the 3rd and 4th order cumulants are very small or vanish in an experimental reconstruction constitutes a reasonable indication that the reconstructed state is Gaussian.

As an example, we spell out the 3rd order cumulants as functions of the moments at the beam splitter outputs reconstructed with the reference-state method. We find [101]

$$\langle\langle\hat{s}_{1,2}^3\rangle\rangle = \langle\hat{s}_{1,2}^3\rangle - 3\langle\hat{s}_{1,2}^2\rangle\langle\hat{s}_{1,2}\rangle + 2\langle\hat{s}_{1,2}\rangle^3 \quad (2.72)$$

$$\begin{aligned} \langle\langle\hat{s}_{1,2}^\dagger \hat{s}_{1,2}^2\rangle\rangle &= \langle\hat{s}_{1,2}^\dagger \hat{s}_{1,2}^2\rangle - \langle\hat{s}_{1,2}^\dagger\rangle\langle\hat{s}_{1,2}^2\rangle \\ &\quad - 2\langle\hat{s}_{1,2}^\dagger \hat{s}_{1,2}\rangle\langle\hat{s}_{1,2}\rangle + 2\langle\hat{s}_{1,2}^\dagger\rangle\langle\hat{s}_{1,2}\rangle^2. \end{aligned} \quad (2.73)$$

Chapter 3

Experimental techniques

Experiments with propagating quantum microwaves are technically demanding since devices based on nanostructures have to be operated at microwave frequencies, very low temperatures (a few tens of millikelvins), and in very low-noise environments. Cutting edge of state-of-the-art microwave technology in combination with our signal recovery concepts empower us to deal with ultra-weak signals with powers of a few attowatts.

In this chapter, we discuss the experimental techniques which we have developed, implemented, and applied to generate and detect states of classical and quantum microwaves as well as path entanglement. In order to demonstrate the suppression of the amplifier noise and the access to higher moments with the dual-path method, we first describe the generation of sophisticated mixtures of weak microwave signals. Next, we present the dual-path setup for weak propagating microwaves, which is the basis for proof-of-principle experiments of the dual-path state reconstruction method and for Planck spectroscopy. Subsequently, in Sec. 3.2, we introduce the Josephson parametric amplifier (JPA) and the experimental setups used to characterize its amplification and squeezing properties. In Sec. 3.3, we consider a setup applied for the reconstruction of quantum microwaves and the detection of path entanglement. Finally, in Sec. 3.4, we consider the stabilization of the experimental setup.

3.1 Dual-path setup for weak propagating microwaves

So far, we have discussed in Sec. 2.5 our powerful dual-path concept. The logical next step is to implement this conception in a setup and to characterize it with

proof-of-principle experiments. In this section, we describe the fundamental dual-path setup in detail. Based on this setup, we demonstrate in Sec. 4.2 the suppression of the amplifier noise and show that the reconstruction of the signal is possible at the same time as tomography of the amplifier noise. Here, we, first, consider the generation of classical mixtures of weak microwave pulses at room temperature. Next, in Sec. 3.1.2 we discuss the cryogenic setup and in Sec. 3.1.3 the cross-correlation detector. Finally, in Sec. 3.1.4, we introduce the calibration techniques which we have developed for precise measurements.

3.1.1 Generation of classical mixtures of weak coherent states

It is our goal to predict whether the dual-path setup is adequate for the reconstruction of quantum signals by conducting proof-of-principle experiments. Here, higher order central moments play an important role since they describe quantum states. Consequently, we need suitable signals to investigate these moments. However, deterministic signals do not possess non-zero central moments because $\langle (f(t) - \langle f(t) \rangle)^n \rangle = 0$ holds. As a solution, we use sophisticated statistical mixtures, whose generation is explained in detail in the following.

We build an ensemble of phase-modulated microwave pulses. The latter are created with a R&S SMF100A (SMF) microwave source in combination with a Tektronix DTG5334 data timing generator (DTG). The microwave source is equipped with a pulse and a phase modulator. The former allows to switch on and off the microwaves on a timescale of 10 ns, whereas the latter changes the phase proportional to an externally applied control voltage. The phase shift φ of the microwave pulses is tunable as shown in Fig. 3.1 and is determined by the voltage at the input of the phase modulator in the SMF and the set value of the phase modulation sensitivity.

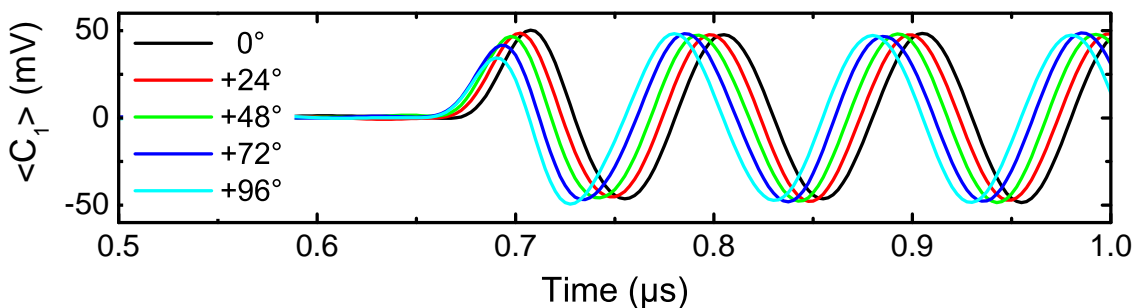


Figure 3.1: Microwave pulses with various phase shifts. The amplitude of the control voltage is constant and the phase modulation sensitivity is varied.

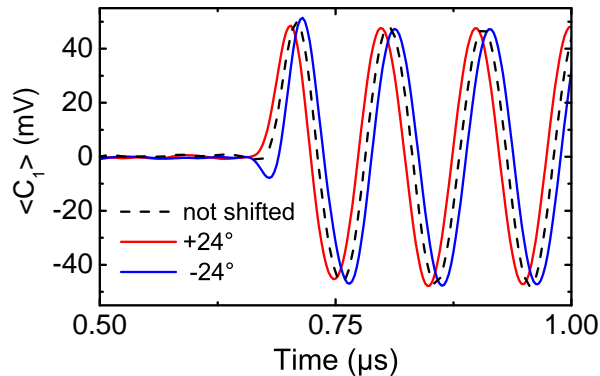


Figure 3.2: Phase-shifted microwave pulses. The red and blue curves are phase-shifted by $+24^\circ$ and -24° , respectively. For the black dashed line the phase modulator was switched off.

For constant phase modulation sensitivity, we can shift the pulse by $+\varphi$ and $-\varphi$ depending on the polarity of the phase control voltage (cf. Fig. 3.2 for an example). From these microwave pulses, we build an ensemble, where the weights of the $-\varphi$ - and $+\varphi$ -states are adjustable. These weights and the phase shift φ are control parameters that are constant for a specific ensemble. By sending a suitable pulse pattern to the modulation inputs of the SMF, ensembles with flat or skewed distribution are created. For example, a sequence of coherent microwave pulses with alternating phase shifts $\pm\varphi$ is generated with the pattern shown in Fig. 3.3(a). This pattern results in a statistical mixture with an equally distributed histogram. For a skewed distribution, which is necessary to investigate non-vanishing third order central moments, the phase control pulse is created in every fourth period¹ [cf. Fig. 3.3(b)].

We note that the individual states, of which the ensemble is built up, can be investigated by changing the pulse pattern of Fig. 3.3(a) in such a way that the acquisition trigger pulse is created only in every second period. The state $+\varphi$ or $-\varphi$ is then selected by the polarity of the phase control channel, which can be inverted. In this way, the data presented in Fig. 3.1 and Fig. 3.2 was taken.

In Fig. 3.3(c), the pulse pattern with the timings applied in the experiment is displayed. The repetition rate of 50 kHz is limited by the response time of the phase modulator. In the Diploma thesis by P. Eder [102], which was created under the supervision of the author of this work, this limitation was further investigated and it was confirmed that the phase adjustment has been completed at the time the signal

¹This is achieved by setting the vector rate of the according channel at the DTG to 1/4.

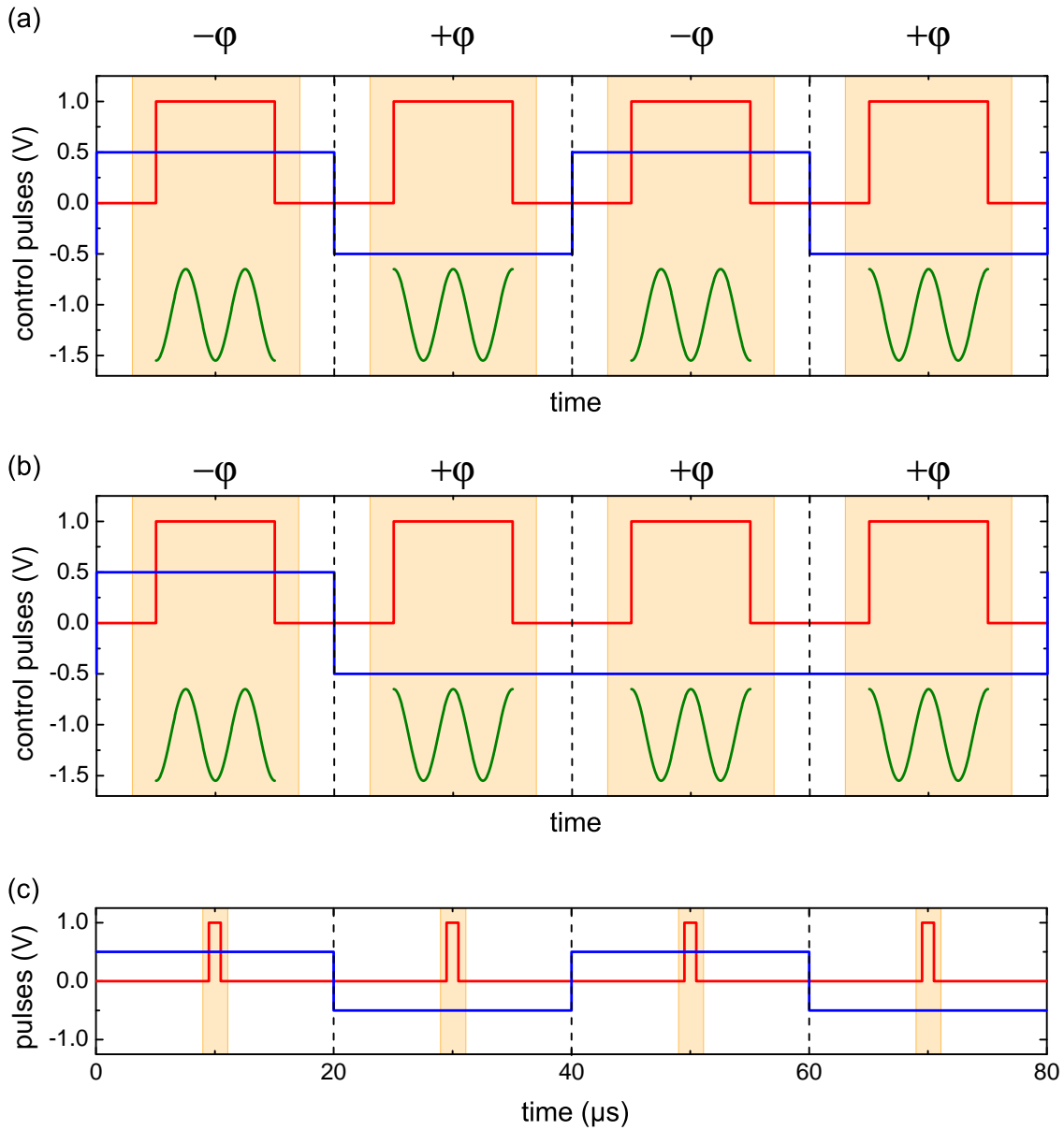


Figure 3.3: Control pulses for the generation of classical mixtures of phase-shifted microwave pulses. (a) Pulse pattern for an equally distributed mixture. The timing of the microwave pulse envelope is controlled by the red curve. The light orange areas mark the measurement windows. The pulses of the control voltage for the phase modulator (blue) are generated in every second period (vector rate is one half) and have the same length as the base period (vertical dashed lines). The green curves symbolize the generated microwave pulses. (b) Pattern for a skewed distribution (25% of the pulses are shifted by $-\varphi$ and 75% by the phase $+\varphi$). The vector rate of the control voltage for the phase modulator (blue) is one fourth. (c) Pulse pattern of panel (a) with the timing used in our experiments.

pulse is created.

It is of utmost importance that the individual states of the ensemble, e.g., the $+\varphi$ -states, are created in a reproducible way so that the phase of the digitized signal is well defined. If this is not the case, phase randomizing effects may cause the signal to vanish during averaging. In order to obtain a well-defined phase, the frequency of the measured signal must be commensurable with the repetition frequency of the generated microwave pulses. Furthermore, the DTG and the microwave sources have to be phase-locked. In our setup, we use a 10 MHz Rubidium frequency standard (Stanford Research Systems FS725) for this purpose.

In order to clean the signals from room temperature thermal noise, they are sent through a series of cold attenuators (Aeroflex Inmet 18AH) which, in good approximation, restrict the thermal contribution to that of a broadband $50\ \Omega$ -resistor anchored to the base plate of the dilution refrigerator. The signal power at the end of the input line P_{in} is determined by the set value of the microwave source and the attenuation of the input line. The calibration of the latter is described in Sec. 3.1.4. We relate P_{in} to an equivalent number of signal photons on average (POA) by dividing the pulse energy $P_{\text{in}}T_{\text{pulse}}$ by the photon energy hf . Here, f is the signal frequency and the pulse duration T_{pulse} of $1\ \mu\text{s}$ mimics standard cavity decay times in circuit QED experiments [85].

3.1.2 Cryogenic setup

For our experiments, we use two setups which mainly differ in the cryogenic beam splitter. In the one we call “HR setup” we make use of a 180° -hybrid ring, whereas in the “WPD setup” we utilize a Wilkinson power divider. Before we devote ourselves to the description of the cryogenic setups, we want to introduce these beam splitters as important elements of our toolbox for quantum optics on a chip.

Microwave beam splitters

Microwave beam splitters divide an input signal while possibly adding phases to their outputs. However, in order to be lossless, matched, and reciprocal, these devices must necessarily have four ports [103]. In a quantum-mechanical picture, this implies that a second, possibly hidden input port is always present [58] (cf. Sec. 4.1.2). In our work, we use two different kinds of beam splitters, a 180° -hybrid ring and a Wilkinson power divider. These devices are often classified as reactive power dividers and provide, in the ideal case, a coupling of 3 dB between the input and each of the

two output ports. In contrast, resistive power dividers based on a resistor network have a coupling of 6 dB between input and output ports due to dissipation.

A sketch of the 180° -hybrid ring microwave beam splitter, which has four external ports, is shown in Fig. 3.4(a). Our device (CPL-5850-100-SMA) was custom-made by MITEQ Estonia and consists of gold microstrip transmission lines on a dielectric substrate encased in a copper housing. Its functionality is best understood as follows: at a wavelength λ , the signals incident at the input ports form an interference pattern in the ring with antinodes at the output ports and nodes at the input ports [103]. This was experimentally demonstrated in Ref. [89], where also typical transmission characteristics are shown. The signals from the two input ports are evenly split and superposed in the two output ports. In this superposition, the component from one of the inputs acquires a 180° phase shift between the output ports, while that from the other one remains in phase. The center frequency of our hybrid ring is 5.75 GHz. In the frequency range used in our experiments, the hybrid ring has a coupling of 3.5 dB between input and output ports and an isolation of at least 38 dB between any two input or output ports. The magnitude imbalance between the two output ports is only 0.03 dB.

The other beam splitter we utilize is a multisection Cohn-type power divider [104] containing several transmission lines of different lengths and resistors to achieve

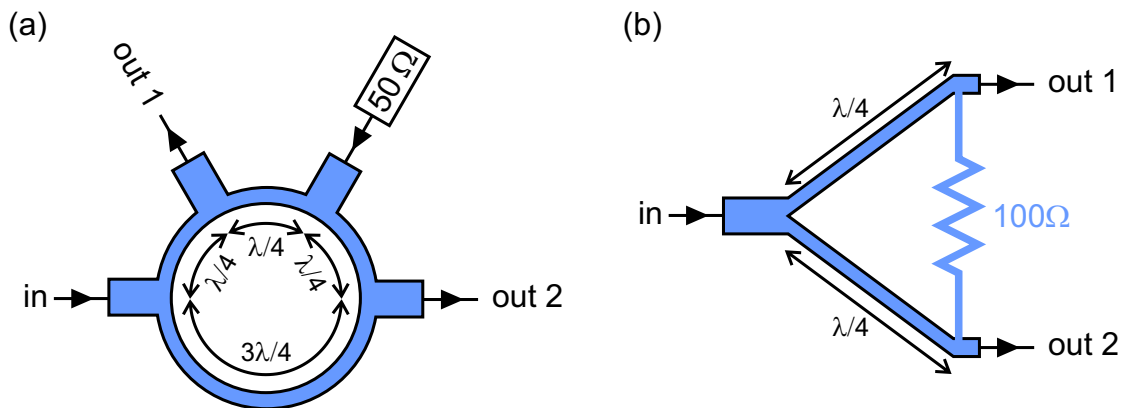


Figure 3.4: Sketch of the beam splitters used in our experiments. (a) 180° -hybrid ring. The split signals from the input (in) acquire a 180° phase shift with respect to each other, while the split signals from the $50\ \Omega$ -termination remain in phase. The microstrip (blue) width encodes the impedance: Z_0 for the straight connections and $\sqrt{2}Z_0$ for the ring. λ refers to the wavelength corresponding to the optimal operation frequency (“center frequency”). (b) Wilkinson power divider. The $100\ \Omega$ -resistor in combination with the $\lambda/4$ transmission lines ensures matching of and isolation between the output ports. Here, we assume a characteristic impedance $Z_0 = 50\ \Omega$.

large bandwidths. For pedagogic reasons,² we present a simplified schematic of a Wilkinson power divider (WPD) in Fig. 3.4(b), which is the one-section limit of the Cohn-type configuration. It equally splits the input signals to the output ports, which are isolated from each other, and provides matching of all ports [106]. In contrast to the hybrid ring, the WPD has only three external ports. However, the resistor that is internally connected between the two output ports in order to provide matching and isolation acts as the termination of a hidden fourth port [58, 105]. The lack of an external fourth port prevents to superpose two input signals in two output paths which is a necessity for the generation of a two-mode squeezed state without additional local squeeze operations. Compared to the hybrid ring, the power divider MITEQ PD2-2000/18000-30S provides a larger bandwidth extending from 2 to 18 GHz at the cost of lower isolation with a nominal value of 14 dB. The insertion loss is specified as 0.8 dB. The large bandwidth is important for the Planck spectroscopy experiments discussed in Sec. 4.1.

The $^3\text{He}/^4\text{He}$ -dilution refrigerator

Our aim is to recover non-classical propagating microwave fields, which so far require superconducting circuits for their generation. Therefore, a cryogenic environment providing millikelvin temperatures is natural for our experimental setup. We use a $^3\text{He}/^4\text{He}$ -dilution refrigerator which was designed and constructed at the Walther-Meißner-Institut by K. Uhlig, A. Marx, C. Probst, S. Höss, and the team of our workshop. Depending on the number of installed microwave lines, the base temperature inside the mixing chamber varies from 12 to 18 mK. At these temperatures, the thermal population for a microwave tone at approximately 6 GHz is negligible and only vacuum fluctuations (shot noise) have to be taken into account. Furthermore, low temperatures allow reducing unavoidable cable losses between components at different temperature stages by using superconducting materials. Losses have to be minimized since they always diminish the signal-to-noise ratio or, in the case of quantum states, mix them with thermal or vacuum fluctuations. For the operation principle and a detailed description of our dilution refrigerator, we refer the reader to the Diploma thesis of M. Á. Araque Caballero [107], which was supervised by the author of this work. At this point, we just want to motivate why the combination of millikelvin temperatures and low-loss microwave circuitry is a technological and

²We note that for the Cohn-type power divider the noise properties of the resistive network can be hard to analyze with simple circuit theory [105]. However, since the WPD and the Cohn-type power divider differ only in the usable frequency range, it is expected that both are described by the same scattering matrix [105]

experimental challenge. Since the cryogenic part of the experimental setup is placed in an inner vacuum chamber, custom-made hermetic feedthroughs for microwaves withstanding the stress of thermally cycling have to be used [105]. The latter can also make the inner conductor of the cables between room temperature and 4.2 K-stage to move even if the cables are specified for cryogenic use. In first experiments, we utilize ULT-05 cables manufactured by Keycom containing a copper foil for better transmission properties. After several cooldowns, the inner conductor moves to an extent such that electrical contact can be lost. For this reason, we use astro-cobra-flex 31086S cables in later experiments. These cables are mechanically stable due to the convoluted design of the outer conductor. As a remedy for uncontrolled changes of the cable transmission during fridge cooldown and warmup, we develop an *in situ* calibration technique which is discussed in Sec. 3.1.4.

When designing the cryogenic setup, one has to respect the limited cooling power of the refrigerator and disburden lower temperature stages from excessive heat load. In the case of the input lines, this can be achieved by thermally anchoring attenuators to various temperature stages of the cryostat. In this way, also the inner conductor of a coaxial cable is cooled. However, for output lines the use of attenuators would diminish the signal-to-noise ratio and thus is not desirable. Therefore, only the outer conductor is thermally anchored by soldered copper wires (1.2 K-pot) or clamped braids (100 mK-stage). Furthermore, circulators anchored to the still (700 mK) thermalize both conductors of the coaxial line, the inner one via a $50\ \Omega$ -load. The high electron mobility transistor (HEMT) amplifiers are thermally anchored to the He-bath (4.2 K), since their dissipated power does not allow operating them at lower temperatures. In the following, we discuss the details on the dual-path setups shown in Fig. 3.5 and in Fig. 3.6.

Attenuated input line

In order to verify that our dual-path method is suitable for the detection of weak propagating microwaves, we conduct proof-of-principle experiments (cf. Sec. 4.2) with sophisticated statistical mixtures generated at room temperature (cf. Sec. 3.1.1). A series of cold attenuators ensures that the thermal noise at the signal port of the hybrid ring is restricted to that of an effective $50\ \Omega$ -termination at the base temperature. Furthermore, these attenuators thermally anchor the inner conductor of the coaxial cables and thus reduce the heat load on the lower temperature stages. For the input lines at temperatures below 4.2 K, we use thin cables with niobium inner and cupro-nickel outer conductor (SC-119/50-Nb-CN) manufactured

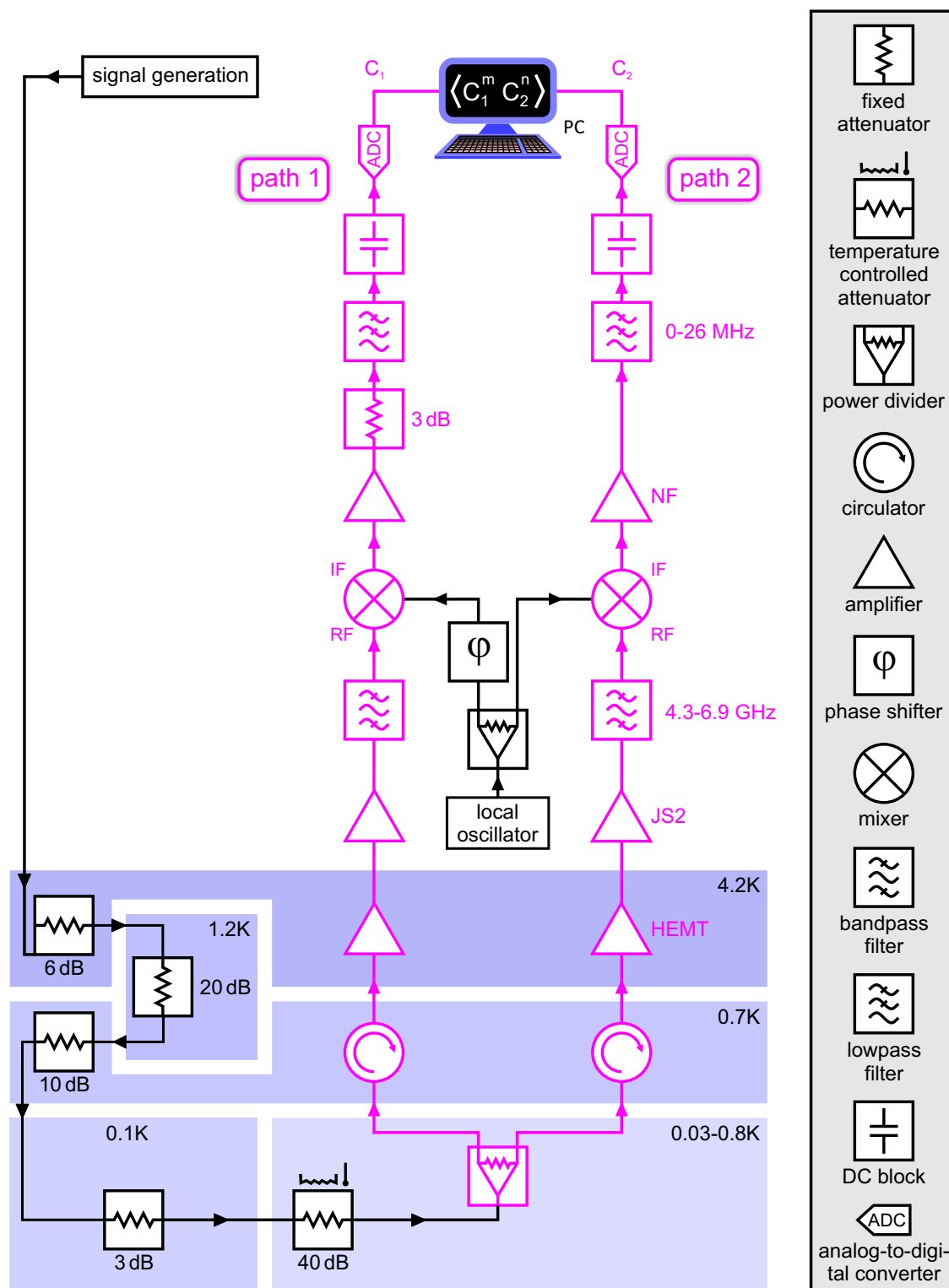


Figure 3.6: Schematics of the WPD setup. The amplification and detection paths are marked in magenta. The 3 dB-bandwidths of the filters are stated close to their symbols. The colored boxes denote the temperature stages inside the fridge.

by Coax Co., Ltd., Japan. These Nb/CuNi-cables have an outer diameter of 1.2 mm (UT47 standard). The total attenuation of the input line between microwave source and beam splitter input is 94 dB for the HR setup and 97 dB for the WPD setup. The difference in the attenuation in the two setups is attributed to the thermal cycling, which changes the transmission properties of the cables between room temperature and 4.2 K by movement of the inner conductor. For details on the applied calibration technique we refer the reader to Sec. 3.1.4.

Millikelvin stage

The central element at the millikelvin stage is the beam splitter, either a 180°-hybrid ring or a power divider. It is thermally anchored to a silver base plate attached to the mixing chamber. For good thermal conduction, we remove the varnish of the power divider box and apply a thin layer of vacuum grease to the contact surface. In Fig. 3.7, the base plate of the HR setup and that of the WPD setup are shown.

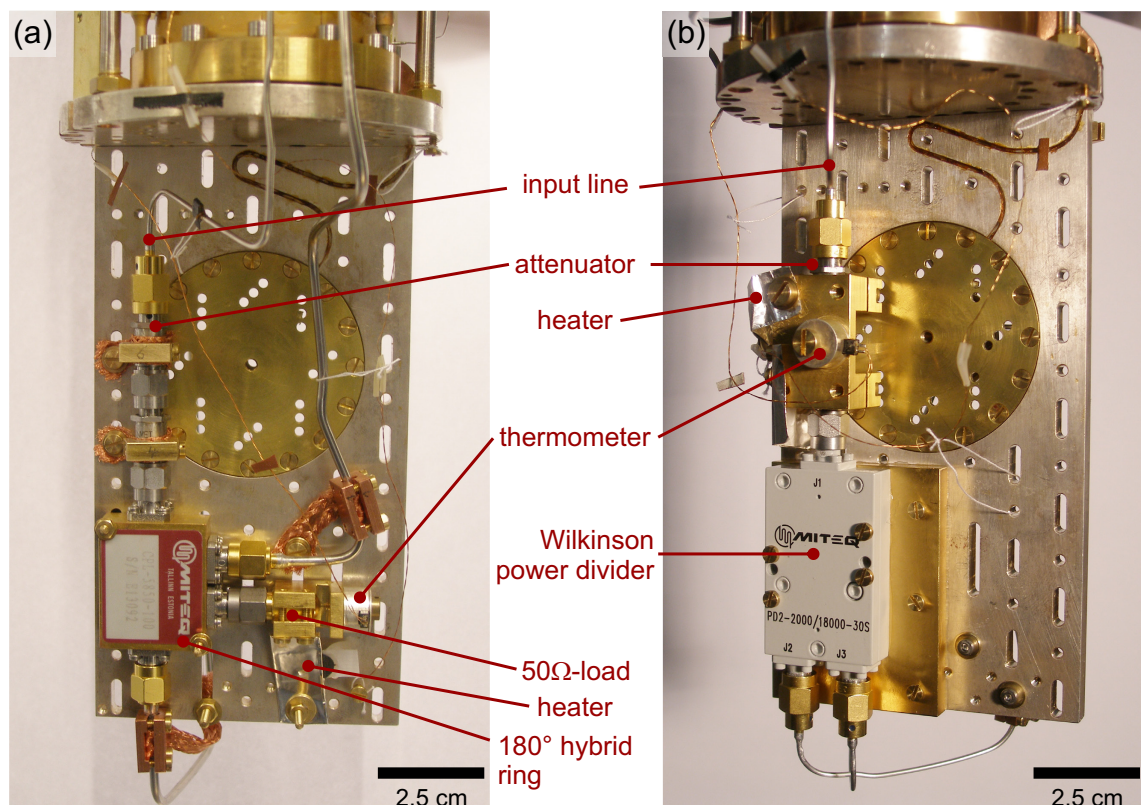


Figure 3.7: Photographs of the dual-path setups. (a) Base temperature plate of the hybrid ring setup. (b) Base temperature plate of the Wilkinson power divider setup.

The last attenuator (40 dB) of the input line, physically a serial combination of two 20 dB-attenuators, and the load of the beam splitter (HR: external, WPD: internal), are thermally anchored to the base plate. Their temperature can be stabilized by a PID controller (Picowatt TS-530A) in combination with a resistive heater. The heater consists of a SMD 0402 100 Ω -resistor glued with black Stycast between a folded silver foil, and electrically isolated from the latter with cigarette paper. The temperature is measured by a RuO thermometer read out with a Picowatt AVS-47A AC resistance bridge. Inside the silver box of the thermometer the leads are thermalized³. The thermometer is attached to the 40 dB-attenuator (WPD setup) or to the load of the hybrid ring (HR setup) by a gold-plated oxygen-free highly-conductive (OFHC) copper clamp. To ensure good thermal contact, we coat the surfaces with a thin layer of vacuum grease and press them firmly together using screws. The creation of a thermal state at the input of the beam splitter allows for a gain calibration of the amplification and detection chains as presented in Sec. 3.1.4.

Output lines

The signal provided by the attenuated input line is divided by the beam splitter and guided by Nb/CuNi coaxial lines to the circulators anchored at the still. We prefer to use thick Nb/CuNi-cables (Coax Co., Ltd. SC-219/50-Nb-CN) with an outer diameter of 2.2 mm (UT85 standard) in the output lines, because their loss is lower compared to thin cables. The loss between the beam splitter output and the HEMT amplifier input is crucial since it can reduce the signal-to-noise ratio considerably. However, thicker cables are more rigid, harder to bend, and more demanding to install. In the case of the HR setup, the output lines are 2.2 mm thick, whereas in the WPD setup the cables are interrupted at the mixing chamber plate by a female/male-connection. The lower, shorter part of the cable is 1.2 mm and the upper, longer part is 2.2 mm thick.

Before the signals are amplified they have to pass a circulator which is a non-reciprocal three-port device. It transmits microwaves in a circular manner, e.g., from port 1 to port 2, from port 2 to port 3, and from port 3 to port 1, whereas it isolates in the opposite direction. It is built from a T junction on which a ferrite post is placed. The ferrite is biased by the static field of a permanent magnet and interacts with the microwave field. Thereby, the time-reversal symmetry is broken resulting in the non-reciprocal transmission behavior. Our circulators (Pamtech

³This silver-box thermometer was designed, built, and precisely calibrated by K. Neumaier (permanent guest at the Walther-Meißner-Institut) .

CTH1392KS2) are magnetically shielded to suppress stray fields. They provide, on the one hand, a better impedance matching to the cryogenic HEMT amplifiers and, on the other hand, isolate the base plate components from the HEMT noise by at least 21 dB in the frequency range from 5.35 to 6.35 GHz. Although not specified, their transmission and isolation properties allow for their operation in a broader bandwidth with marginal degradation of the isolation. However, the white noise of their loads anchored at the still with a temperature of approximately 0.7 K is not hindered from propagating down the output lines. The isolation of the beam splitter in combination with the one of a single circulator prevents the existence of noise which is correlated between the two chains. Figure 3.8 shows a photograph of the still and 4.2 K-stage of our cryostat.

Next, the signals are fed into the cryogenic HEMT amplifiers each anchored at 4.2 K by an annealed Cu plate screwed to the amplifier's housing and connected to the vacuum flange by two soldered copper braids. The amplifiers are connected to the circulators via Nb/CuNi-cables. Halfway in between, their 1.2 mm thick outer conductor is thermally anchored to the 1.2 K-pot by means of soldered copper wires. The cryogenic HEMT amplifiers were manufactured in the Group for Advanced Receiver Development (GARD) at Onsala Space Observatory and at Chalmers Univer-

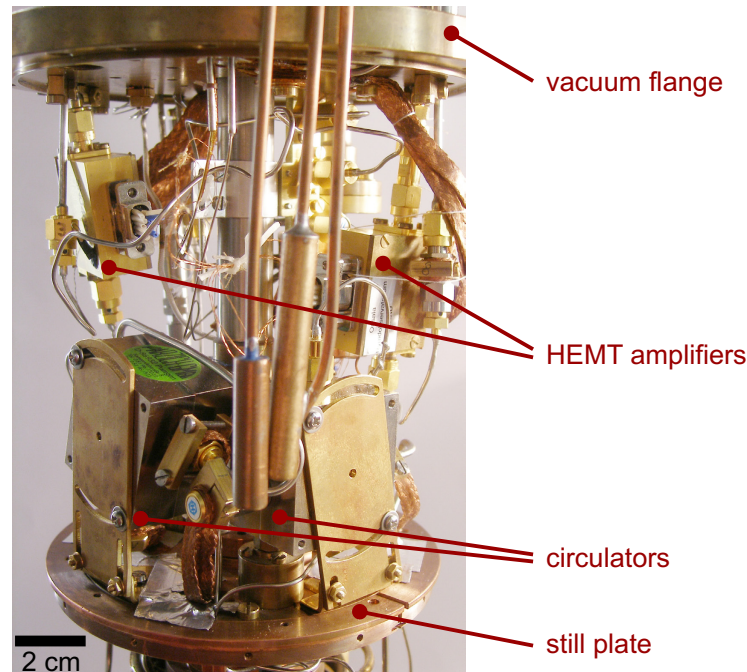


Figure 3.8: Photograph of the still and 4.2 K-stage of the cryogenic dual-path setups. The circulators and their $50\ \Omega$ -loads are thermally anchored to the still plate (0.7 K). The HEMT amplifiers are anchored to the vacuum flange (4.2 K).

sity of Technology, Gothenburg, Sweden. They consist of two amplification stages with HEMTs based on GaAs technology. Their operation bandwidth extends from 4 to 8 GHz. The two amplifiers provide a gain of 24 and 25 dB, respectively, and a noise temperature of nominally 6 ± 1 K for our operation frequency of approximately 6 GHz. The noise temperature was measured at an ambient temperature of 12 K by the manufacturer. At 4.2 K, we expect similar or even lower values. Our amplification and detection chains are designed in such a way that their noise temperature is dominated by the cryogenic HEMT amplifiers. The room temperature components of these chains are discussed in the next section.

3.1.3 Cross-correlation detector

In this section, we first discuss why a direct acquisition with analog-to-digital converters is not suitable for our application and then introduce the cross-correlation detector.

A direct detection of our microwave frequency signals would require fast digitizing rates of at least 12 gigasamples per second to obey the Nyquist-Shannon sampling theorem [108–110]. While analog-to-digital converters are commercially available with the required sampling rates, they are limited in the vertical bit resolution to typically 8 bits and are quite expensive. A further complication are the resulting high data rates which have to be efficiently processed. In a computer-based architecture the data has to be buffered and then evaluated. This results in long dead times. Furthermore, acquisition boards equipped with field programmable gate arrays for data processing in real time do not support the required sampling rates for direct detection. Therefore, one has to shift the signal frequency to a range where the signals can be handled more easily. Since our signals have a narrow bandwidth of the order of some 10 MHz, this is possible without any loss of information. The core component for this task is a mixer which downconverts the gigahertz frequencies to the megahertz regime. It is a non-linear device based on fast switching diodes that are biased by a microwave tone called local oscillator (LO). Effectively, the mixer multiplies the input microwave signal (RF port) by the LO sinusoidal wave. Thereby, difference and sum frequencies are created. The latter are eliminated by internal lowpass filters.

In the following, we describe the signal flow through the cross-correlation detector (cf. Fig. 3.5 and Fig. 3.6). The output signals of the cryogenic setup are further processed by MITEQ JS2-02000800-08-0A (JS2) low-noise amplifiers with a noise temperature of nominally 60 K and a gain of 24 – 25 dB. In the HR setup, an-

other amplifier (MITEQ AFS5-00100800-14-10P-5) is connected in series to the JS2. The signals are then bandpass-filtered (Mini-Circuits VBFZ-5500+) to reduce noise outside the bandwidth of interest. Next, mixers (Marki Microwave M3-0312LP) downconvert the microwaves to an intermediate frequency (IF). In the case of coherent input signals, an IF of 10 MHz is chosen by setting the LO frequency 10 MHz lower than the signal frequency. The IF signal is fed into NF Corporation SA-421F5 amplifiers with a gain of 46 dB and a bandwidth of 30 Hz–30 MHz. However, in the HR setup the total amplification is so large that additional attenuators in front of the NF amplifiers have to be used to prevent compression effects. For a good linear performance of the amplifier the input signal power has to be suitably below the 1 dB-compression point. The same is true for a mixer. In our case, the power level at the RF input of the mixers is far too low to cause compression effects. In the WPD setup, the AFS amplifiers and the associated attenuators are removed. The overall lower total gain is compensated by a different sensitivity setting of the acquisition board. Before digitizing, the signals are lowpass-filtered with a Mini-Circuits SLP-21.4 used as an anti-aliasing filter. DC blocks (Aeroflex Inmet 8535) suppress DC offsets possibly caused by the mixers or the NF amplifiers. We note that the measurement bandwidth of the cross-correlation detector is twice the one of the lowpass filter since the image band (RF frequency lower than the LO frequency) is also detected, i.e., $|f_{\text{RF}} - f_{\text{LO}}| \leq f_{\text{lowpass}}$ holds. Due to the DC blocks, the RF and LO frequency have to be different to produce a measurable IF signal and therefore the setup is classified as a heterodyne receiver.

Data acquisition and processing

The IF signals are synchronously sampled by an Acqiris DC440 digitizer board with nominally 12 bit resolution at 400 megasamples per second. The oversampling allows for a display of the traces with good time resolution and lowers the demands on the anti-aliasing filter. The digitizer is placed in an external enclosure to avoid the noisy environment inside a personal computer (PC). The data is transferred to the PC by a cabled PCI bus. The measurements are controlled by LabVIEW invoking a dynamic link library (DLL) written in C++ by the author of this work. This program acquires the data, calculates the moments $\langle C_1^\ell C_2^m \rangle$, where $0 < \ell + m \leq 3$, and averages the ensemble. Despite the use of DC blocks, slowly drifting offsets, e.g., due to the ADCs, may be still present. We suppress such offsets by the following protocol. The raw data is divided into segments of 4128 traces equivalent to 0.5 s measurement time. For each of these segments, the time average is subtracted from

each data point before any other manipulation. Effectively, this procedure acts as a highpass filter eliminating slow drifts in the data. Since the C++ code is quite efficient the bottleneck is not the data processing but the data transfer between the digitizer and the PC. This problem can be solved by a field programmable gate array (FPGA) based architecture as discussed in the next section. We refer to the unit of heterodyne receiver, data acquisition board, and processing DLL as cross-correlation detector.

With respect to the cross-correlation detector, a good balancing of the experimental setup regarding amplitude and phase is a prerequisite for successful experiments. A pre-balancing of the amplitude is done by an attenuator in one of the lines. In the HR setup, the phase difference has been tuned by changing the cable length at the RF input of the mixer with the help of adapters close to 180° . By using a phase shifter in the local oscillator line of one of the two mixers, the phase difference can be set more precisely in the WPD setup. There, we use a phase balancing of 0° since this is the phase shift between the signals at the outputs of a WPD. Further details on the balancing are presented in the next section.

3.1.4 Calibration

In this section, we present calibration techniques which form the basis for precise measurements. Our calibration methods provide effective means to compensate changes in the experimental setup, which can be induced, for example, by mechanical stress during the refill of the cryostat's dewar with liquid helium. In order to avoid decorrelation effects, the signals in the two amplification and detection chains have to be aligned regarding phase. A balancing of the signal amplitude implies equal gain of the two chains and results in simpler equations for the signal reconstruction (cf. Sec. 2.5). Furthermore, a calibration of the power of the classical signals is necessary to investigate the resolution limits of our implementation of the dual-path method.

Amplitude and phase balancing of the two chains

To investigate the balancing of the dual-path setup, a coherent test signal is injected into the beam splitter. Amplitude pre-balancing is achieved by means of a 3 dB-attenuator in one of the two paths. We compensate the residual gain imbalance (<1 dB) by applying a numerical compensation factor during data acquisition before the moments are calculated. This factor is determined by comparing the IF ampli-

tude of the two channels C_1 and C_2 in the ensemble averaged first moments. Next, the phase difference between the two channels is calibrated to 0° (WPD setup) or 180° (HR setup) by aligning the curves of C_1 and C_2 or of C_1 and $-C_2$, respectively.

Calibration of the input line attenuation

In our setup, the attenuated input line can be calibrated *in situ* by determining the total transmission from the source to the digitizer and the gain of the amplification and detection chains. For the gain calibration, known thermal states are injected into the input ports of the beam splitter and the dependence of the measured power at the digitizer on the temperature of the thermal state is analyzed. To this end, the $50\ \Omega$ -load at the ancilla port of the hybrid ring (HR setup), respectively the attenuator at the input of the power divider (WPD setup), is temperature-controlled using a heater and a thermometer. Since heating is faster than cooling in our setup, we use the following downsweep protocol. The temperature of the load and base plate is stabilized to 800 mK for half an hour, the heating is switched off, and the measurement is started. Due to the strong thermal coupling between the load and the base plate the heat capacity is significant and cooling is slow enough to allow for a well-defined temperature of each measurement point. We can safely assume the beam splitter, ancilla load, and effective $50\ \Omega$ -load at the signal port to have the same temperature. Both loads inject thermal voltage fluctuations into the beam splitter. The auto-variance of these fluctuations follows the well-known Planck function. The gains G_1 , G_2 and noise temperatures $T_{N,1}$, $T_{N,2}$ of the amplification and detection chains are inferred from a numerical fit of the power at the digitizer

$$\frac{\langle (C_i - \langle C_i \rangle)^2 \rangle}{R} = G_i B \left(\frac{hf}{\exp\left(\frac{hf}{k_B(T - \delta T_i)}\right) - 1} + \frac{hf}{2} + k_B T_{N,i} \right), \quad i = 1, 2 \quad (3.1)$$

with the fitting parameters gain G_i , $T_{N,i}$, and δT_i . Here, $R = 50\ \Omega$ is the termination load of the ADC input, f is the center of the detected frequency band and B is the measurement bandwidth. The latter is known from a measurement with a spectrum analyzer ($B = 51\ \text{MHz}$). The parameter δT accounts for small differences between the measured temperature and the electronic temperature of the load. For the HR setup, we find gains of approximately 110 dB for both chains, where small residual gain asymmetries have been absorbed in a compensation factor already. With this result, the 0.5 dB loss of the hybrid ring, and the total transmission from source to digitizer, we calculate an input line attenuation of 94 dB. The latter allows us to

determine the signal power P_{in} at the input of the beam splitter. For the WPD setup, we retrieve an attenuation of the input line of 97 dB and a gain of the amplification chains of 90 dB.

3.2 Josephson Parametric Amplifier

Since the advent of circuit quantum electrodynamics [6, 17–19], the demand for ultra-low-noise amplifiers in the gigahertz regime is increasing. As phase-sensitive amplifiers [81], Josephson parametric amplifiers [23, 111–119] (JPA) are allowed to amplify a single quadrature of a signal without adding noise to it. For this reason, they are very attractive devices for studies on propagating quantum microwaves [56]. Furthermore, the excellent noise properties allow for the investigation of quantum objects such as superconducting qubits [7, 15, 114, 120–122] or nano-mechanical resonators [123]. In addition, we want to note that there is a close analogy between vacuum amplification effects in quantum field theory and parametric amplification in microwave circuits [124]. As an example, the dynamical Casimir effect has been observed in such a system [34]. Although in practice internal losses may limit the noise performance of a JPA, it can nevertheless be used to beat the standard quantum limit for phase-insensitive amplifiers [23]. The ability to do so is a prerequisite to generate squeezed vacuum states [23–25, 44, 56, 125–127], which have potential applications in the realm of quantum information processing. Prominent examples in the optical regime are the generation of distributable unconditional entanglement [5] or memories for entangled continuous-variable states [128].

In our experiments, we make use of a flux-driven JPA [117] to generate propagating quantum microwaves by squeezing vacuum, thermal or coherent states. First, in Sec. 3.2.1, we introduce the basic operation principle. Subsequently, in Sec. 3.2.2, we give details on the sample. In Sec. 3.2.3, we discuss a setup for the characterization of the amplification and squeezing properties of the JPA. Finally, in Sec. 3.2.4, we consider the optimization of the operation point.

3.2.1 Principle of operation

We illustrate the working principle of a parametric amplifier by the analogy to a playground swing. There, a child increases the oscillation amplitude by a modula-

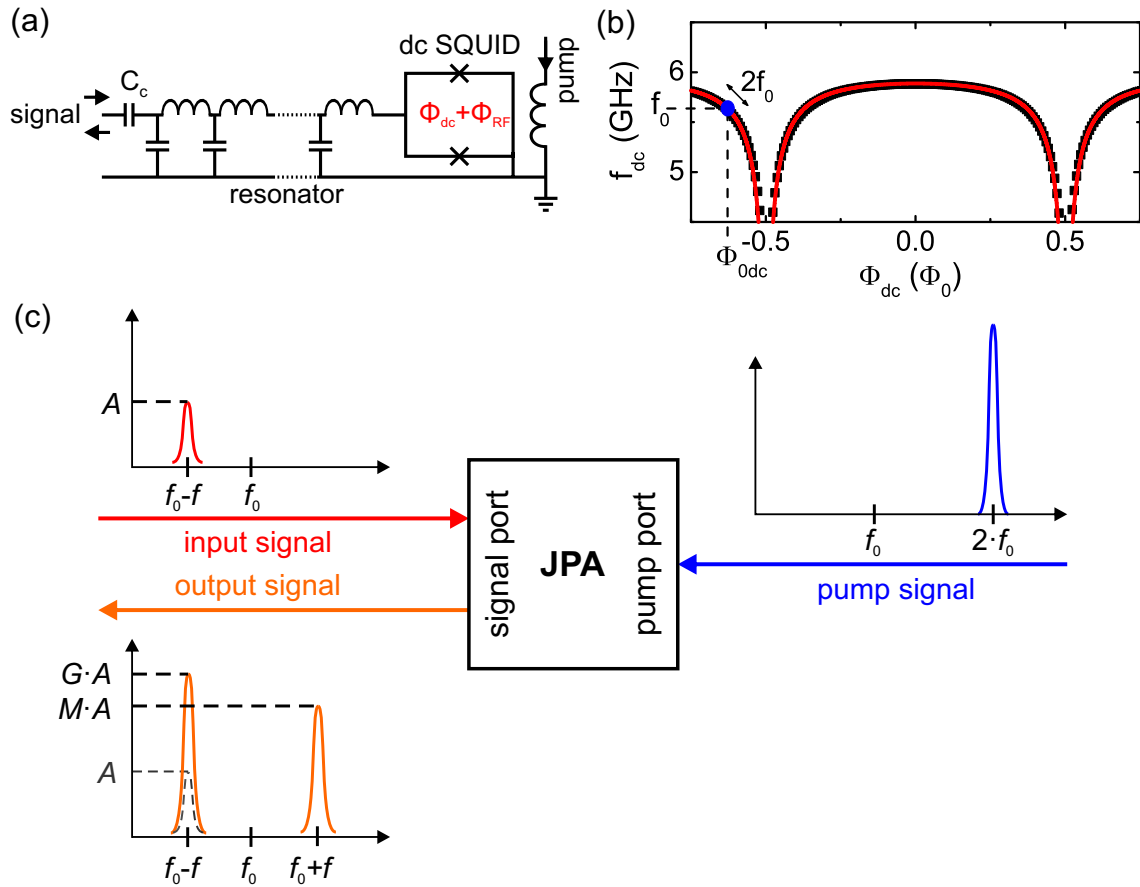


Figure 3.9: Flux-driven JPA. (a) Circuit diagram. The transmission line resonator is shunted by a dc SQUID (loop with crosses denoting Josephson junctions) at one end. A magnetic flux $\Phi_{\text{dc}} + \Phi_{\text{RF}}$ penetrating the dc SQUID thereby modulates the resonant frequency. (b) JPA resonance frequency f_{dc} as a function of the applied dc flux Φ_{dc} . Black symbols: data. Red line: fit (cf. Ref. [129] for details). Blue dot: operating point $f_0 = 5.637$ GHz. (c) Operation principle adopted from Ref. [129]

tion of the swing length⁴. The latter is most efficient if the modulation frequency amounts to twice the oscillation frequency of the swing. In the case of a flux-driven JPA, whose circuit diagram is depicted in Fig. 3.9(a), the oscillator is represented by a superconducting coplanar waveguide resonator. In order to achieve a parametric effect, the resonance frequency f_{dc} of the quarter wavelength resonator is modulated. To this end, a dc superconducting quantum interference device (SQUID) – a superconducting loop interrupted by two Josephson junctions – is inserted between the center conductor and the ground plane at the shorted end of the resonator. Because

⁴More precisely, a child standing on a swing varies its center of mass by bending its knees and thus modulates the effective length of the swing [124, 130]. This situation is analog to parametric amplification, whereas a child sitting on a swing and moving its legs is better described by driving the oscillator than parametrically pumping the latter [131].

the SQUID acts as a flux-tunable inductor, the resonance frequency of the resonator can be changed with the help of an external magnetic field [cf. Fig. 3.9(b)]. Via an external coil, we first set a quasistatic bias corresponding to a JPA operating frequency f_0 . When we apply a fast modulation at $2f_0$ (pump tone) via an on-chip antenna, parametric amplification is achieved. A signal at $f_0 - f$ impinging at the signal port is amplified by the signal gain G and reflected back out of the signal port. At the same time, an idler mode at $f_0 + f$ is created, whose amplitude is determined by the intermodulation gain M . This operation principle is depicted in Fig. 3.9(c). For vacuum fluctuations as input signal, this process is the analog of spontaneous parametric downconversion in optics, where a pump photon is split into a signal and an idler photon. Therefore, strong quantum correlations between the signal and the idler mode are established which finally lead to squeezing.

In comparison to other implementations, we want to stress an important advantage of the flux-driven design [117]: The pump tone is well separated from the signal regarding frequency and thus does not contaminate the signal. Furthermore, there is a large isolation of 28 dB between the pump and signal port of the JPA at the signal frequency hindering noise from the pump line to enter the resonator. Contrarily, in JPAs based on Kerr-non-linearities the pump and signal frequencies are degenerate [116]. Thus, when a clean state is needed the strong pump tone has to be eliminated by an interference technique [56]. The flux-driven design renders this technique obsolete and reduces the experimental complexity, e.g., the number of required input lines.

Though the study of the JPA is an interesting topic on its own, we do not want to delve into details on a theoretical description of the JPA that is based on input-output formalism [132] and refer the interested reader to the appendix of Ref. [129]. Of course, this theory proved to be quite useful in predicting key characteristics such as the signal bandwidth in the design process of the JPA. Within the frame of this work, we want to apply the JPA as an element of our toolbox for quantum optics on a chip solving the task of squeezed state generation. Thus, we concentrate on a detailed experimental characterization of the JPA and ensure that the sample is working correctly and provides squeezing. Knowing key parameters is especially helpful to design the path entanglement cross-correlation detector correctly. For example, the JPA signal gain bandwidth determines the choice of the measurement bandwidth of the detector for mode matching.

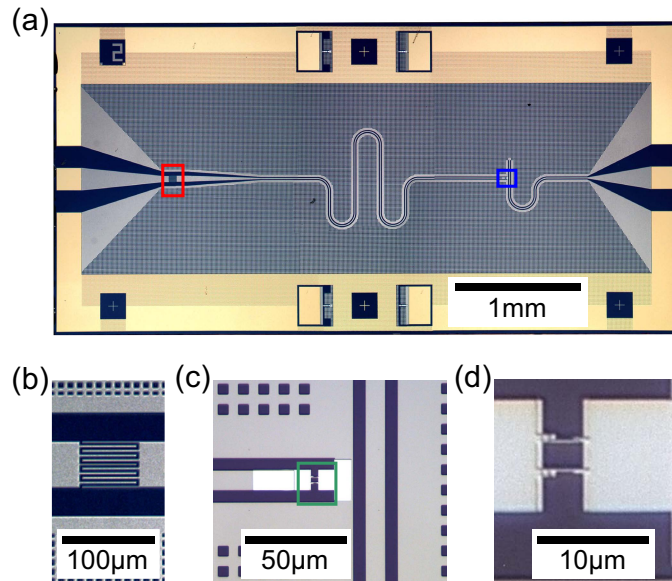


Figure 3.10: Micrographs of the JPA sample #2-1c used in our experiments. (a) Sample chip. (b) Zoom on the region marked with the red rectangle in panel (a), showing the coupling capacitor $C_c = 30$ fF (design value). (c) Pump line and dc SQUID. Zoom on the region marked with the blue rectangle in panel (a), showing the pump line and the dc SQUID. (d) Zoom on the region marked with the green rectangle in panel (c), showing the dc SQUID. The size of the loop is $4.2 \times 2.4 \mu\text{m}^2$. Reprinted adopted figure from Ref. [59].

3.2.2 The JPA sample

The JPA samples have been designed by T. Yamamoto and fabricated by K. Inomata in the group of Y. Nakamura at NEC Smart Energy Research Laboratories, Japan. We have investigated two samples with different design values of the external quality factor $Q_{\text{ext}} = 300$ and $Q_{\text{ext}} = 30$ implemented by distinct values of the coupling capacitance C_c [cf. Fig. 3.9(a)]. As the $Q_{\text{ext}} = 30$ sample broke during a thermal cycle its squeezing properties could not be investigated. Therefore, we concentrate on the sample #2-1c with $Q_{\text{ext}} = 300$ in this work. For a comparative study of the amplification properties of the two samples we refer the interested reader to the Diploma thesis of A. Baust [129], which was supervised by the author⁵. Micrographs of the device used in our experiments are shown in Fig. 3.10. The resonator and antenna are patterned from a sputtered 50 nm thick Nb film. At the contacts, 95 nm of gold on a 5 nm titanium bonding layer are deposited on top. As substrate, we use thermally oxidized (300 nm) silicon with a thickness of 300 μm . The dc SQUID is fabricated in the last step using aluminum technology

⁵In Reference [129], the overall performance of the JPA is lower than in this work, because a different procedure for setting the operation point is applied (cf. Sec. 3.2.4 for details).

and shadow evaporation [133]. The Al electrodes have a thickness of 50 nm each. From Fig. 3.9(b), we estimate a Josephson coupling energy $E_J = h \times 650$ GHz for each junction⁶, where $h = 6.63 \times 10^{-34}$ Js is the Planck constant. At the operation frequency $f_0 = 5.637$ GHz the external quality factor is measured as $Q_{\text{ext}} = 312$. We determine an isolation between antenna and resonator of more than 28 dB at the signal frequency f_0 . The sample chip is placed between two small alumina printed circuit boards inside a gold-plated copper box.

3.2.3 Characterization setup

In this section, we describe the setup used to determine the amplification properties and for first squeezing experiments. After a description of how to generate the dc magnetic field bias, we present the cryogenic and room temperature setups in detail.

Superconducting coil and persistent current switch

In order to tune the JPA frequency a static flux is used. The magnetic field is generated by a superconducting coil equipped with a persistent current switch. The latter allows to freeze a persistent current in the coil. This provides an effective isolation from current noise possibly present on the coil leads. Details on the superconducting coil and persistent current switch are presented in Appendix A.

Spectroscopy setup for measurements of amplification properties

The experimental setup sketched in Fig. 3.11(a), allows for the characterization of two JPA samples in the same cooldown making use of microwave switches to select between the samples and a calibration short. The switches have been developed in cooperation with Agilent technologies resulting in the new option C02 of the N18xx series optimized for the use at cryogenic temperatures. This option is characterized by removing any grease inside the switches that may block them at low temperatures and by excluding current interrupts. In order to limit heat dissipation, the switches are of latching-type and are operated by current pulses. The latter are provided by an electronics [129] developed by U. Guggenberger⁷, the author, and A. Baust⁸.

⁶We note that this value of E_J was retrieved from a lumped element model of the JPA. Considering the distributed character of the transmission line resonator [134], we determine a Josephson coupling energy $E_J = h \times 1305$ GHz for each junction.

⁷Walther-Meißner-Institut, Bayerische Akademie der Wissenschaften, D-85748 Garching, Germany

⁸Walther-Meißner-Institut, Bayerische Akademie der Wissenschaften, D-85748 Garching, Germany

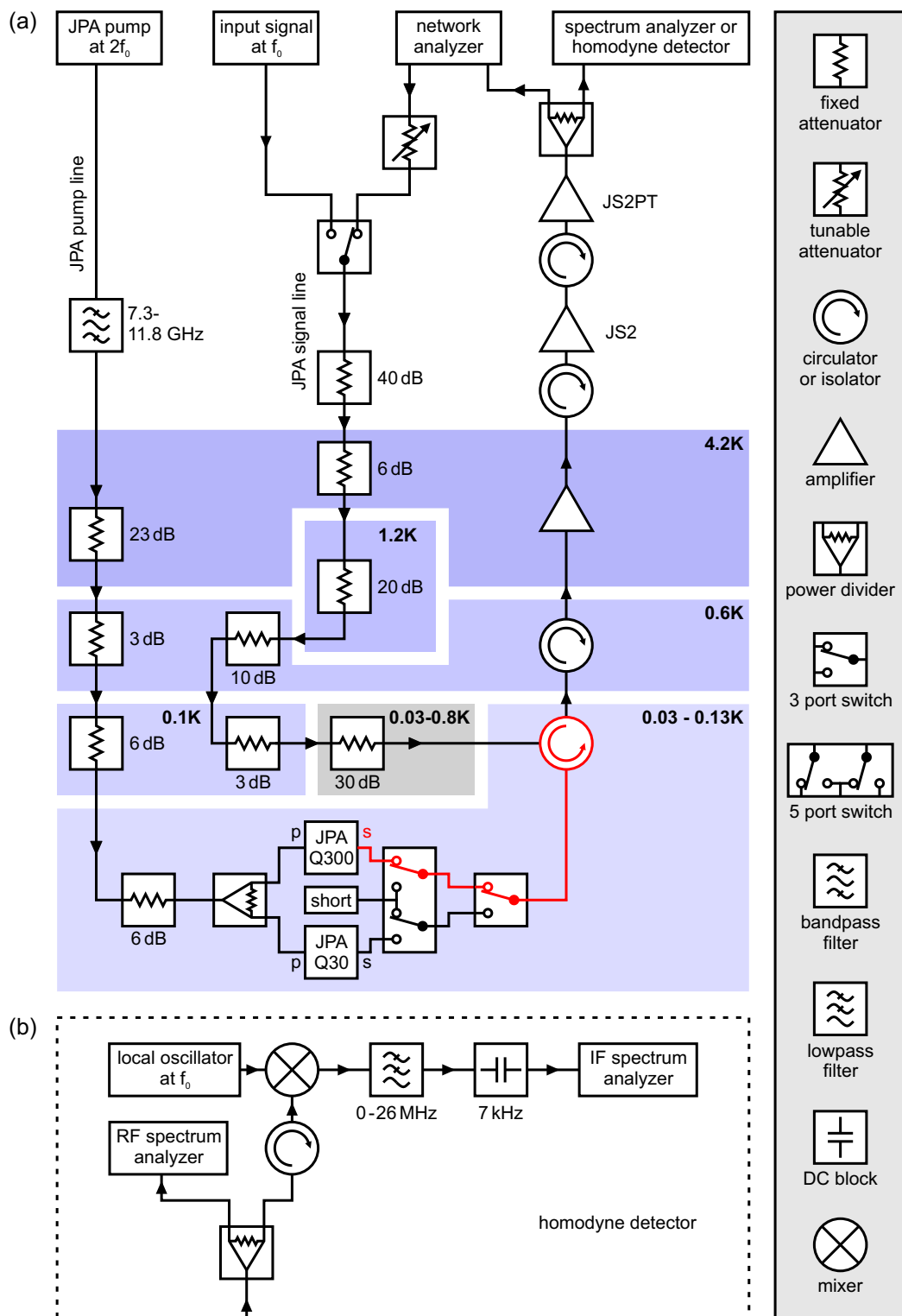


Figure 3.11: Schematic of the JPA characterization setups. (a) Spectroscopy setup for the characterization of amplification properties. (b) For the investigation of squeezing, the homodyne detector replaces the spectrum analyzer in (a). The numbers close to the filters state the 3 dB-bandwidths.

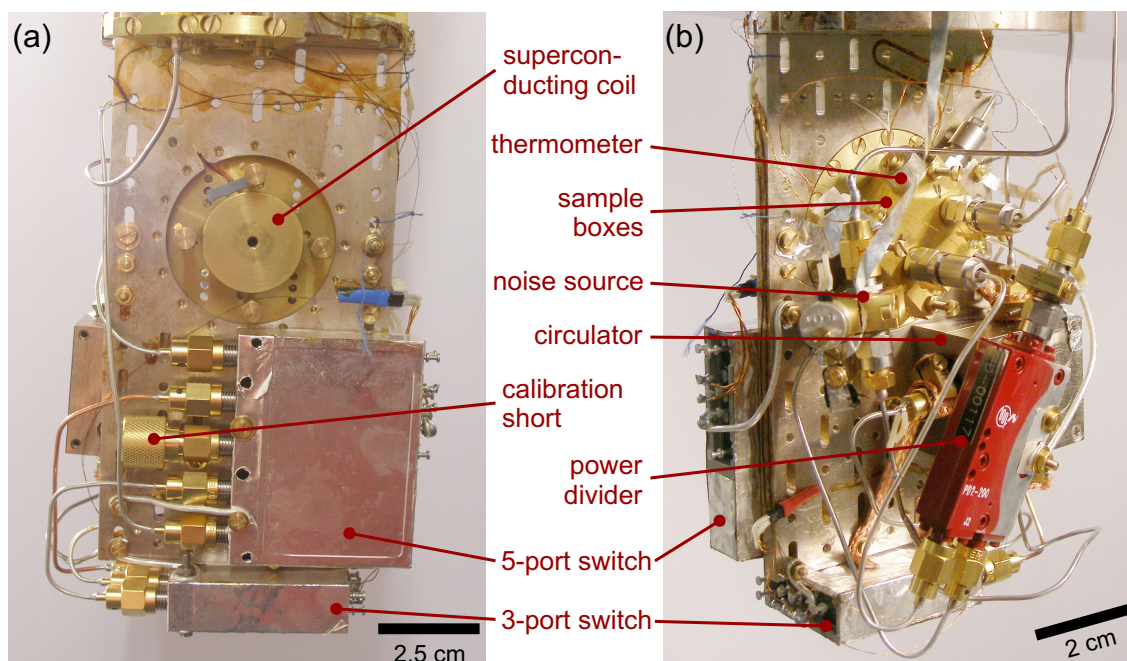


Figure 3.12: Photographs of the base plate of the JPA characterization setup. (a) Rear view. (b) Front view.

Figure 3.12 showing photographs of the sample plate conveys an impression that fitting all the components is challenging.

The signal, generated either by a microwave source or the vector network analyzer (VNA), passes a series of warm and cold attenuators. The signal power levels stated in Sec. 5.1 are referred to the output of the 30 dB-attenuator acting as thermal noise source. The loss of the input line is calibrated with the method described in Sec. 3.1.1. The noise source is thermally decoupled from the base plate and is discussed in detail in Sec. 3.3.1. For gain measurements, a coherent signal generated either by a microwave source or a VNA is fed through the attenuated input line via the measurement circulator to the JPA. This circulator separates the outgoing from the incoming signal and isolates the JPA from the noise generated by the amplifiers in the output line. The amplified output signal can be detected by a VNA or a spectrum analyzer. The VNA allows one to investigate the complex reflection coefficient of the JPA. The spectrum analyzer is used to investigate the idler gain and the degenerate operation of the JPA (cf. Sec. 5.1.6). We note that in all JPA characterization experiments we make use of continuous-wave signal and pump tones without pulse modulation because of the used measurement devices. Sub-harmonics of the pump tone, which can distort the signal, are suppressed by a serial combination of four Mini-Circuits VHF-7150+ bandpass filters. For noise

temperature measurements, the same setup is used, and by heating the weakly anchored 30 dB-attenuator a thermal state is injected into the JPA.

As the cross-talk of the on-chip pump line and the resonator of the JPA is not known during the design phase of the experimental setup, we choose a pump line attenuator configuration providing a compromise between heat dissipation and rejection of thermal noise from higher temperature stages. This results in a sample box temperature of approximately 70 mK, when the JPA is continuously pumped. However, the temperature drops, when the JPA is deactivated. Therefore, the temperature of the JPA box is controlled and stabilized to 90 mK. Since in these experiments, only one resistance bridge and temperature controller is available, the JPA box temperature is not stabilized when the noise source is used. We note that due to the higher pump power dissipation, in this setup the JPA box temperature is higher than in the path entanglement setup, where the JPA box temperature is stabilized at 50 mK.

Homodyne detection setup for squeezing measurements

For homodyne squeezing measurements, the same cryogenic setup is used. In the room temperature detection setup, the spectrum analyzer of Fig. 3.11(a) is replaced by the circuit depicted in Fig. 3.11(b). The signal is split and measured by a RF spectrum analyzer and a homodyne detector. The former provides information on the signal power whereas the latter allows to detect a single quadrature. This phase-sensitive detection is a prerequisite for squeezing measurements. The homodyne detector consists of a local oscillator microwave source and a mixer to downconvert the microwaves. The LO frequency is set to half the pump frequency so that the signal and idler mode are mapped onto the same intermediate frequency detected by a R&S FSV 30 spectrum analyzer. The resulting interference reveals the strong correlations established between the idler and signal mode by the JPA. Depending on the phase difference between signal and idler mode, which can be controlled by the phase of the LO, the interference is constructive or destructive. For the latter case, fluctuations are decreased and this is referred to as squeezing.

Losses of the cryogenic setup

The level of squeezing and the noise temperature of the JPA depend on the losses present in the setup. Therefore, we determine the relevant losses by transmission measurements at 4.2 K in a vacuum chamber cryostat. In order to reduce the number of cooldowns to a practicable amount, the transmission through suitable combina-

tions of parts is measured. The transmission through an individual component can be retrieved by solving a system of linear equations.

3.2.4 Optimization of the operation point

The methods of how to set the operation point have advanced over time. In first experiments [129], the pump frequency is set to twice the resonator frequency, where the latter is determined from a phase-vs.-frequency characteristics without pumping. Later, we observe that the resonance frequency shifts, when the JPA is pumped. Consequently, the operation point can be optimized by tuning the pump frequency, while measuring the signal gain with a network analyzer. However, for the path entanglement measurements a different approach is more suitable. As the cross-correlation detector is calibrated for a specific frequency (cf. Sec. 3.3.4), the operation point is optimized by tuning the flux. Finally, the determination of the optimal operation point is automated applying the following sequence.

1. The pump power is calculated from the set value of the signal gain and applied. To this end, a phenomenological formula describing the dependence of the signal gain on the pump power is found.
2. A fine flux sweep is carried out while measuring the signal gain. The retrieved data is analyzed with a Gaussian fit.
3. The maximum of the fitted curve is compared to the set value of the signal gain and the pump power is adjusted accordingly.
4. Another flux sweep is measured and analyzed. The flux is set to the abscissa value of the maximum of the fitted curve.
5. After setting the flux to persistent mode, a control measurement is taken.

Figure 3.13 shows the second flux sweep for a set value of the signal gain of 10 dB. The result of the flux control sweep is 10.05 dB.

3.3 Dual-path setup for propagating quantum microwaves and path entanglement

When detecting actual quantum correlations or quantum states rather than weak classical mixtures, quadratures have to be measured instead of signal amplitudes.

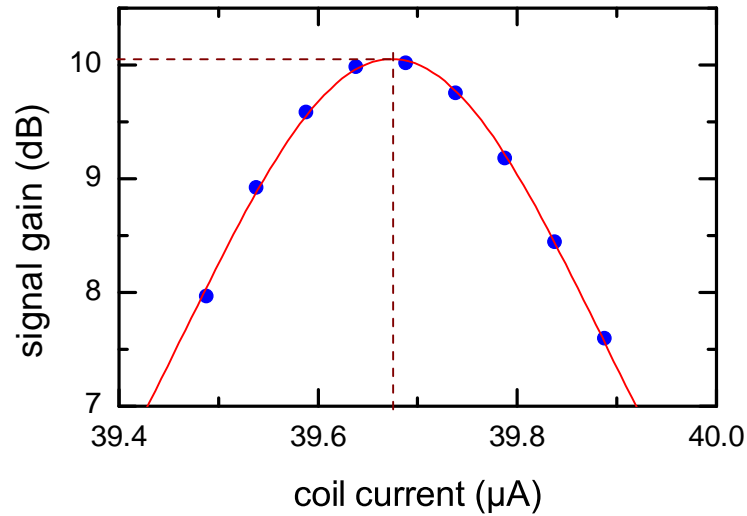


Figure 3.13: Second flux sweep for optimization of signal gain. Blue points: measured signal gain. Red curve: Gaussian fit. Brown dashed lines denote the maximum of the Gaussian fit.

Furthermore, the stability of the dual-path setup is significantly improved by thermally isolating the noise source from the mixing chamber and an FPGA logic allows for real time data processing. In Sec. 3.3.1, we describe the cryogenic setup. Next, in Sec. 3.3.2, we discuss the IQ cross-correlation detector and, in Sec. 3.3.3, the data acquisition and the FPGA logic. Finally, in Sec. 3.3.4, we consider the calibration of the setup.

3.3.1 Cryogenic setup

The complexity of the cryogenic setup required for reliable and clean preparation of squeezed states implies a large number of quite bulky microwave components at the base plate of the dilution fridge. A detailed sketch of the experiment is shown in Fig. 3.14. However, the limited space in our fridge (cf. Fig. 3.7) does not allow us to place these components. Therefore, we enlarge the base plate length from 13 cm (cf. Fig. 3.7) to 48 cm (cf. Fig. 3.15), demanding for the redesign and production or acquisition of a number of parts such as a silver base plate extension, the still radiation shield, the vacuum chamber, the Cryoperm magnetic shield, the He Dewar, and the room temperature Mu-metal shields. In this way, we make room for mounting multiple experiments in a single cooldown. As a consequence, our millikelvin resources can be used more efficiently: During the time needed for data analysis or improvement of room temperature setups, the fridge is used by a different

person carrying out another experiment. The fridge provides now 40 twisted-pair lines, 7 high-bandwidth coaxial input lines, and 4 high-bandwidth coaxial output lines. The latter are equipped with a cryogenic HEMT amplifier each. Rather than bothering the reader with an endless description of all the work leading to a well equipped and stably performing fridge, we mention that four PhD students including the author and two student trainees worked one year on the reconstruction. The increased sample throughput has made this time investment worthwhile already within another year. In the following, we present the main components of the cryogenic setup for experiments with quantum microwave states.

Noise source for the generation of thermal states

We use a temperature-controlled load to generate thermal microwave states. These are required for the calibration of the gain of our amplification and detection chains and for the investigation of squeezed thermal states. In contrast to the WPD and HR setups, where a strong coupling of the load to the base plate changes the temperature of the whole millikelvin setup, we have decoupled the load thermally from the base plate. To this end, we use a UT47 Nb/CuNi-cable between the temperature-controlled 30 dB-attenuator and the input port of the measurement circulator. Figure 3.15 displays a photograph of the base plate setup. Furthermore, we utilize an annealed silver ribbon with a cross-sectional area of $4 \text{ mm} \times 40 \text{ }\mu\text{m}$ and 15 cm length as weak thermal link between the noise source and the lower step exchanger. This configuration has a number of advantages:

1. The heat capacity of the noise source, which is much smaller than that of the base plate, allows for a much faster thermal cycling of the noise source and decreases the waiting time between calibration and measurements. Due to the fast cooling rate, the downsweep protocol described in Sec. 3.1.4 is impractical. Therefore, we make use of upsweeps, where each temperature is set and stabilized. Thus, in contrast to downsweeps, the cooling rate does not influence the measurements. As the cooling rate decreases with time, the number of acquired points and thus the statistical uncertainty is temperature-dependent in a downsweep measurement. This does not pose a problem for Planck spectroscopy experiments. However, in path entanglement experiments with squeezed thermal states the measurement takes so long that the temperature would not be well defined. With the help of temperature-controlled upsweeps, the conditions for the measurements become significantly more reproducible.

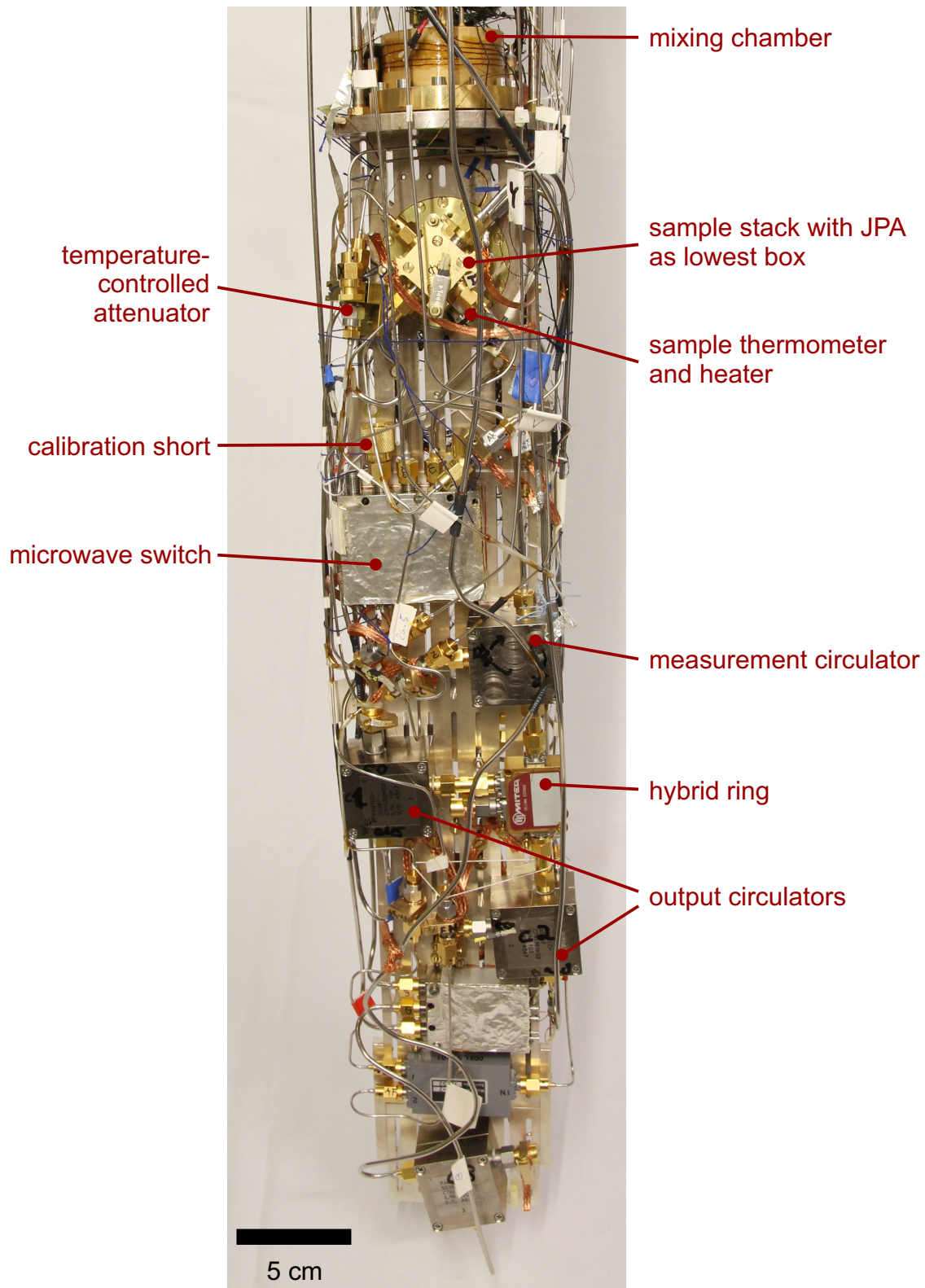


Figure 3.15: Photograph of the sample plate of the path entanglement setup. Unlabeled components are part of other experimental setups.

2. The temperature range of the noise source is extended by the thermal decoupling and ranges from 50 to 800 mK. In the WPD and HR setups, due to the downsweep protocol the upper limit for the temperature is approximately 350 mK.
3. With the decoupled noise source, fridge parameters such as the condenser pressure hardly change during a temperature sweep. As a consequence, the still temperature remains constant. In contrast, in the downsweep measurements with strongly coupled load, the fridge is driven into a non-equilibrium condition. As a result, the still temperature changes by approximately 50 mK, which affects the noise generated by the circulator load.
4. The base plate temperature can be stabilized independently of the load temperature with the help of a second temperature controller at 50 mK and stays constant up to a noise source temperature of 700 mK. This is of major importance when using a JPA since its operating point shifts with temperature. The stable base plate temperature guarantees that microwave losses in the cryogenic setup and in the output lines are constant. Variable temperature gradients occur only in the short cable connecting the noise source with the measurement circulator. This localization allows one to model the effects of the temperature gradients in order to obtain a more precise gain calibration.

Generation of squeezed states and path entanglement

For the generation of squeezed states, we make use of a JPA. Its signal line is heavily attenuated at various temperature stages, whereas the pump line is only moderately attenuated to disburden the fridge from dissipation caused by the much larger power levels. The low attenuation of the pump line is made possible by the large isolation of more than 28 dB between the pump line and the resonator on the JPA chip. The reduced heat load compared to the JPA characterization setup enables us to stabilize the base plate temperature at 50 mK measured on the JPA sample box. As the JPA is operated in reflection, a measurement circulator is used to separate the JPA input and output signals. The latter is sent into the hybrid ring acting as the beam splitter of the dual-path detection setup. JPA, 50 Ω -terminated hybrid ring, and measurement circulator are anchored to the base plate. Near the 50 Ω -termination of the hybrid ring, we measure a temperature of 40 mK.

For the propagating microwave state impinging at the input of the 180°-hybrid ring we have several options: We can apply strongly attenuated coherent states

generated by a microwave source (SMF) at room temperature by directing them through the measurement circulator to the inactive JPA (pump off). There, they are reflected and sent back through the circulator to the input of the beam splitter. Thermal or vacuum states are produced by the temperature-controlled noise source as described above. When we switch on the JPA by applying a suitable pump tone, we can squeeze the mentioned states and produce squeezed vacuum, squeezed thermal and squeezed coherent states. By superimposing such non-classical states with the vacuum state of a cold load we produce path entanglement between the propagating signals in the output (cf. Sec. 2.8 for theory and Sec. 5.4 for experimental results).

We note that during measurements of squeezed states, the JPA pump at frequency $2f_0$ is operated in pulsed mode. Similarly, we also use pulsed probe signals when measuring coherent states of frequency f_0 , where f_0 is the center frequency of the mode, whose quadrature components are measured by the IQ cross-correlation detector (cf. Sec. 3.3.2). The rise and fall times of the pulse envelopes are approximately 10 ns. As shown in Fig. 3.16, the measurement window always contains an off-region as a reference in addition to the signal. At temperatures below 51 mK, the thermal occupation is less than 0.005 photons at 5.637 GHz and, as a consequence, this reference state can be considered as the vacuum (cf. also Sec. 2.9).

With the help of a microwave switch between the measurement circulator and the JPA, the latter can be replaced by a calibration short with ideal reflection allowing for the determination of the total loss of the combination of JPA, sample box (alumina boards and connectors), and interconnecting cable. However, we note that we use the switch only for this purpose and do not change it in all the other experiments. The reason for this is that switching heats the base plate requiring long waiting times for cooling and increases significantly the probability of flux jumps.

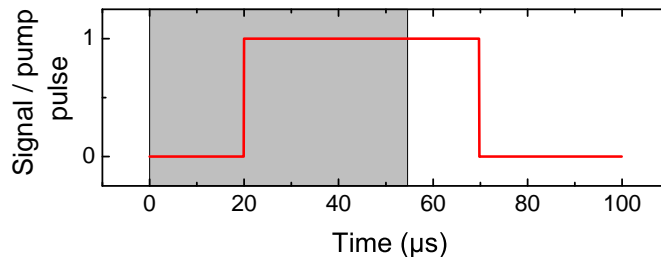


Figure 3.16: Measurement protocol for squeezed and coherent states. During the high time (“1”) of the pulse envelope, either the coherent signal or the JPA pump tone is on, during the low time (“0”) both are off. The shaded area denotes the measurement window.

As shown in the discussion of the generation of classical mixtures in Sec. 3.1.1, phase synchronization is important. Here, the rotationally non-invariant⁹ squeezed states demand for a good phase stability and control (cf. Sec. 3.4.2). To this end, the JPA pump and signal microwave sources, the vector network analyzer, the local oscillator for the IQ mixers, and the clock for the ADCs and the FPGA logic are synchronized with a 10 MHz Rubidium frequency standard (Stanford Research Systems FS725).

The vector network analyzer is used to measure the JPA operating point, signal gain, and idler gain. Finally, in addition to the elements shown in Fig. 3.14, several components such as mechanical microwave switches, power dividers, and a spectrum analyzer are used in the real setup. We omit these elements in the present discussion since they serve purely technical purposes (e.g., debugging or switching to other experiments) and are not essential for the functionality of the IQ cross-correlation detector and the entanglement detection.

Output lines

In the IQ cross-correlation detector, each of the two amplification paths contains a circulator anchored to the base plate and one anchored to the still. The base plate circulators (PAMTECH CTH1932KS2) suppress the noise from the loads of the still circulators by nominally 21 dB in the frequency range from 5.35 to 6.35 GHz. Due to space limitations, the still circulators are mounted as double-circulator assemblies (PAMTECH CTH1365-K18-A, cf. Fig. 3.17). The still circulators provide an isolation of 18 dB from the cryogenic amplifiers (Low Noise Factory LNF-LNC4_8A) within a bandwidth of 4 to 8 GHz. These amplifiers consist of three amplification stages with HEMTs based on InP technology and are thermally anchored to the 4.2 K-flange of the fridge. At our operation frequency of approximately 5.6 GHz, their nominal gain and noise temperature are 43.5 dB and 2 K, respectively. These values were measured by the manufacturer for an ambient temperature of 10 K. In comparison to the cryogenic GARD amplifiers, used in the setups discussed in Sec. 3.1.2 and Sec. 3.2.3, the gain is larger by 19 dB and the noise temperature has improved by a factor of three. This results in a significantly better noise performance of the amplification chains. Notably, the power consumption is only 7 mW and thus less than half of that of the GARD amplifiers.

⁹We refer to the Wigner function representation in phase space.

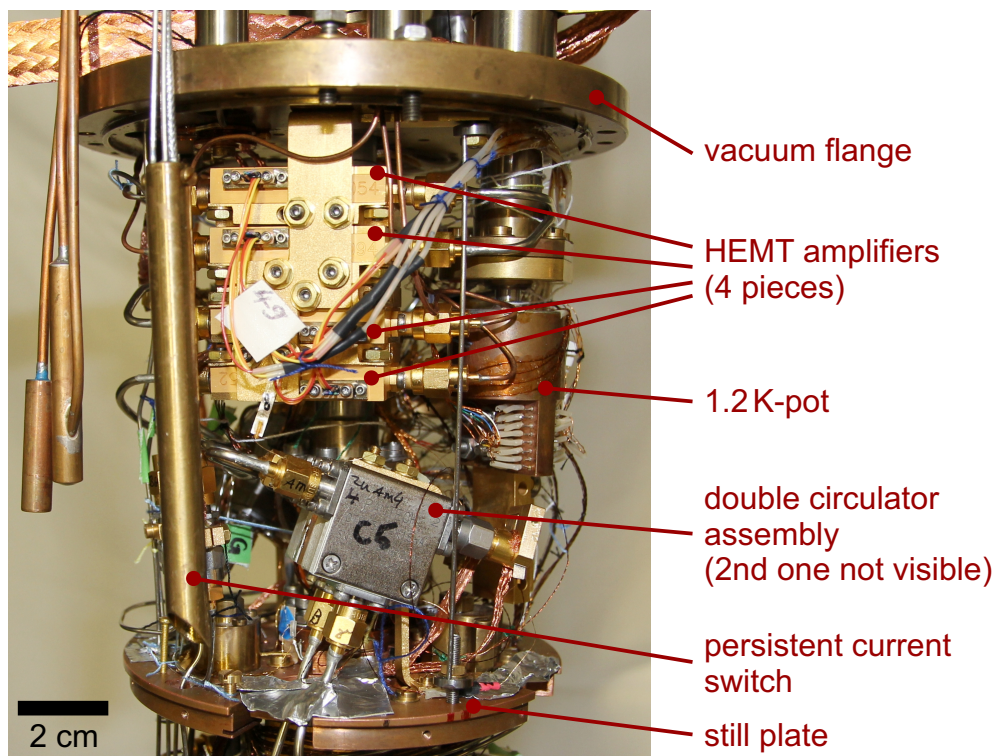


Figure 3.17: Photograph of the cryogenic amplifiers and still circulators. These circulators and their 50Ω -loads are thermally anchored to the still plate (0.7 K). The HEMT amplifiers are anchored to the vacuum flange (4.2 K).

3.3.2 IQ cross-correlation detector

In Fig. 3.18, a simplified sketch of the IQ cross-correlation detector is shown. Along each path, the high frequency (RF) signal emerging from the hybrid ring is linearly amplified, filtered, downconverted to an intermediate frequency (IF) $f_{\text{IF}} = 11$ MHz, and digitized at a sampling rate of 150 MHz by 16 bit analog-to-digital converters. The IQ mixers (Marki microwave IQ4509LXP) used for downconversion are biased by a strong local oscillator (LO) at 5.626 GHz and split each output signal into its in-phase ($I_{1,2}$) and quadrature ($Q_{1,2}$) components – therefore four ADCs are required. The digitized signals are finally fed into an FPGA logic (details can be found in Sec. 3.3.3) which computes all correlations up to the fourth moment in amplitude in real time. Phase synchronization is guaranteed by using a joint local oscillator for downconversion and referencing the clock of the FPGA logic to that of the local oscillator. By means of a phase shifter at the LO input of one of the two IQ mixers, the phase difference of the two paths is pre-balanced to approximately 180° . Finetuning of the phase balance is performed within the FPGA logic. In order to avoid spurious

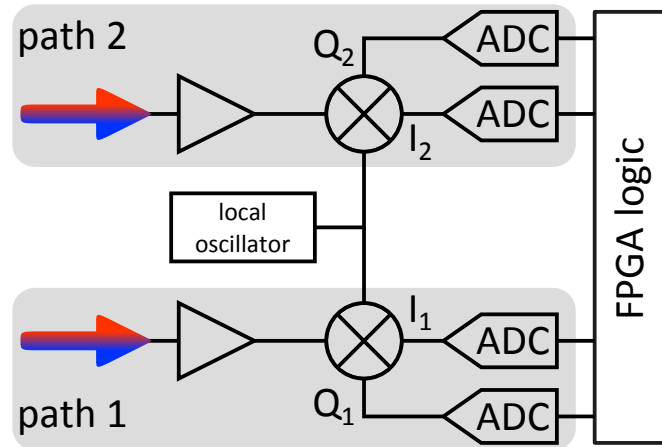


Figure 3.18: Sketch of the IQ cross-correlation detector. Colored arrows: output signals from the hybrid ring. Triangular symbols: amplifiers. Circles with crosses: IQ mixers.

correlated noise contributions, isolators (MCLI IS-19-1/SMO) are inserted at several points in the setup (cf. Fig. 3.14). At room temperature, the output signals are amplified with Miteq JS2-02000800-08-0A (JS2PT) and Mini-Circuits ZX60-6013E amplifiers in the RF path and with Miteq AU-1447 (AU) amplifiers in the IF path. Since the output power of the IF amplifiers is limited, we use Mini-Circuits SBP-10.7+ bandpass filters at their input avoiding compression effects induced by noise outside the region of interest in the frequency spectrum. Furthermore, we place tunable attenuators with a resolution of 0.1 dB (EPX microwave inc. ESA2-1-10/8-SFSF) before the IF amplifiers allowing one to adapt the amplitude of the IF signals to the fixed ± 1.5 V input range of the ADCs and to pre-balance the four channels. The four ADCs and a Xilinx Virtex-5 SX95T FPGA providing 9 million gates are combined in the Innovative Integration X5-RX high performance digitizing and signal processing module. It is connected via a single lane cabled PCIe interface to a host computer, where a measurement server program written by Peter Eder¹⁰ and Matthias Ihmig¹¹ represents the interface to the LabVIEW control software. The author has coordinated and supervised the development process and contributed to the debugging and testing of the measurement server and its interface to LabVIEW. The LabVIEW control program, which contains routines such as the phase stabilization protocol (cf. Sec. 3.4.2), has been developed by the author. Figure 3.19

¹⁰Walther-Meißner-Institut, Bayerische Akademie der Wissenschaften, D-85748 Garching, Germany

¹¹Lehrstuhl für Integrierte Systeme, Technische Universität München, D-80333 München, Germany

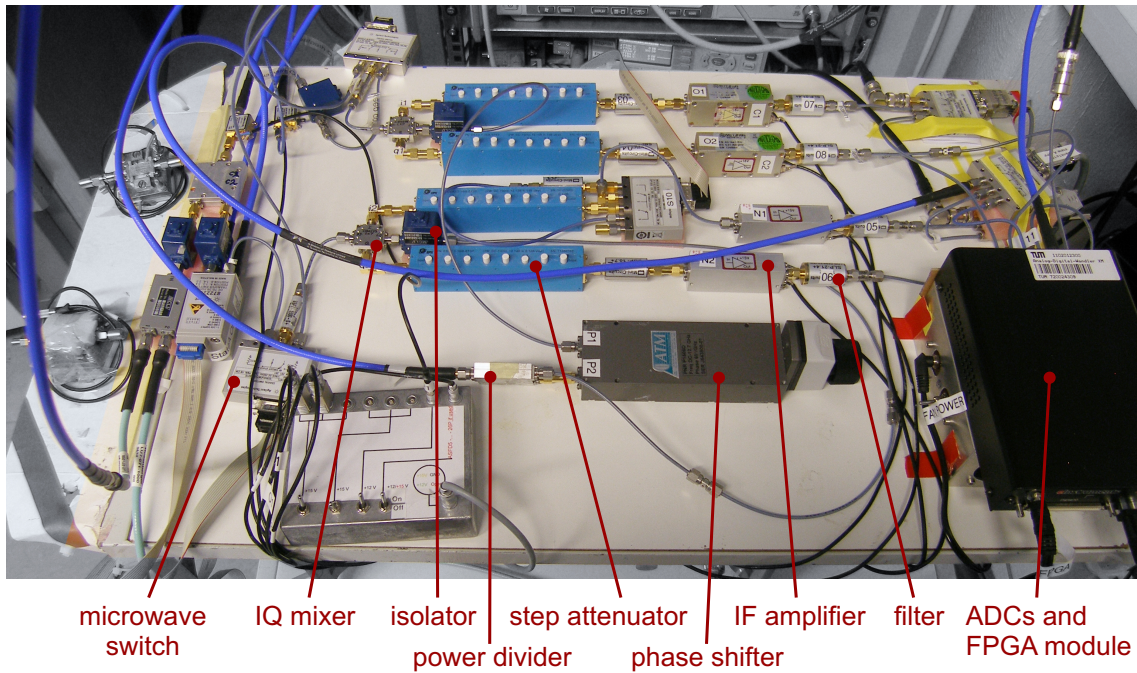


Figure 3.19: Photograph of the IQ cross-correlation receiver.

depicts a photograph of the IQ cross-correlation detector and in Fig. 3.20, the measurement rack is shown. With the help of microwave switches, the cryogenic setup can be bypassed and the receiver inputs are connected to a microwave source using a splitter at room temperature. In this way, the FPGA logic can be tested with large amplitude signals without noise, which is very convenient during debugging.

3.3.3 Data acquisition and processing by FPGA logic

For the reconstruction of quantum microwaves and the detection of path entanglement, we have to measure the complex envelope of two microwave signals, i.e., their orthogonal quadrature voltages by homodyning. To this end, we make use of a two-step approach consisting of an analog heterodyne receiver (cf. Sec. 3.3.2) and a digital downconversion logic. Compared to a purely analog version of homodyning, our method has several advantages:

1. By using intermediate frequencies on the order of 10 MHz and appropriate analog and digital filtering, $1/f$ -noise is effectively suppressed.
2. Imperfections of the IQ mixers such as amplitude and phase imbalances can be corrected for in the digital downconversion scheme.

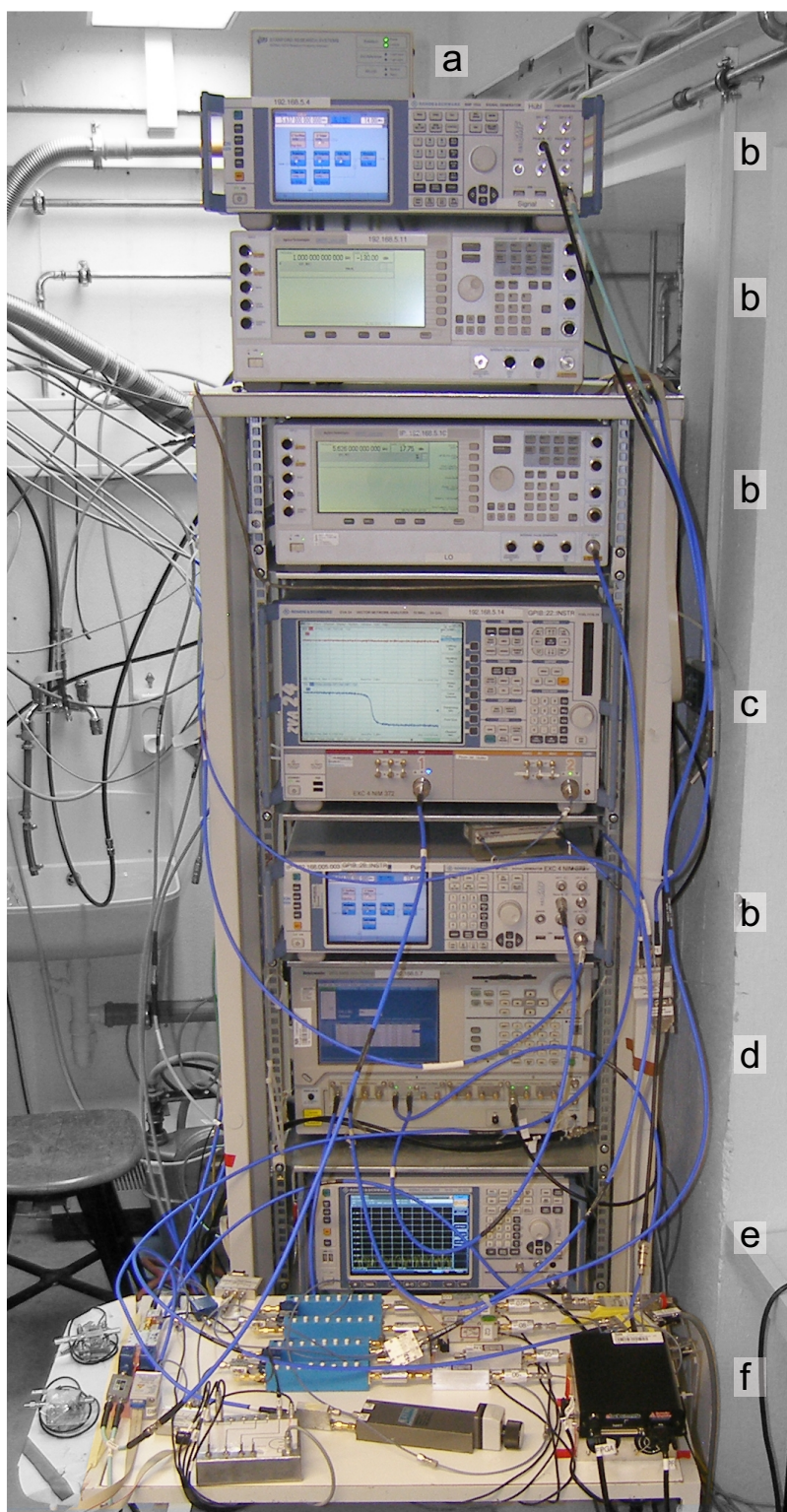


Figure 3.20: Photograph of the measurement devices. (a) Rubidium 10 MHz source for phase locking. (b) Microwave source. (c) Vector network analyzer. (d) Data timing generator. (e) Spectrum Analyzer. (f) IQ cross-correlation receiver.

3. The high-speed ADCs of our FPGA board are AC-coupled with the band starting at nominally 1 MHz. Although our FPGA board is also equipped with ADCs with DC-coupled inputs, these do not fulfill our bandwidth requirements because of their low sampling rate of 250 kHz. Therefore, we use the high-speed ADCs and intermediate frequencies well above 1 MHz.

We want to note that, in principle, single ended analog mixers in combination with digital IQ mixers may be used. However, this method has the disadvantage that the measurement bandwidth is only half of that in our approach [135]. This bandwidth restriction would render future applications such as the analysis of systems with superconducting qubits suffering from decoherence effects difficult. Moreover, as compared to a single mixer setup, the IQ mixer setup has the advantage that it does not require a steep filter (≈ 2 MHz) at the LO frequency $f_0 - f_{\text{IF}}$ in the RF path to remove unwanted frequency components at the mirror frequency $f_0 - 2f_{\text{IF}}$. Such a filter would be difficult to calibrate and fix the setup to that specific frequency f_0 .

For the dual-path reconstruction and the entanglement detection, the orthogonal I and Q quadratures of the noisy signal have to be recorded for both paths and products of the type $\langle I_1^j I_2^k Q_1^m Q_2^n \rangle$, where $0 < j + k + m + n \leq 4$ and $j, k, m, n \in \mathbb{N}_0$, need to be calculated for each recorded data point. However, the presence of the amplifier noise of our paths requires significant averaging. The latter in combination with the high acquisition rate (150 – 400 MHz) results in a large amount of data. As a consequence, data transfer rate and computation time become a serious bottleneck in a computer-based acquisition system. By streaming the data from the ADCs directly into an FPGA logic, we solve these problems and are able to perform the moment calculations in real time. The FPGA logic has been developed by Matthias Ihmig, at which the author has defined specifications and contributed to testing and debugging the logic. In the design process, Simulink and Xilinx System Generator provide a graphical environment clearly representing the logic structure. Once the development is complete, a bitstream is synthesized using the tools of the ISE Design Suite from Xilinx [136]. Finally, this bitstream is loaded into the FPGA.

Figure 3.21 shows the task graph for our FPGA logic. After an external trigger event the four IF signals $I_{1,\text{IF}}$, $Q_{1,\text{IF}}$, $I_{2,\text{IF}}$, $Q_{2,\text{IF}}$ are synchronously sampled at a rate of 150 MHz. For each channel, 8192 raw samples, equivalent to one frame of data, are directly streamed into the physical layer processing chain. The digital front-end consists of the gain balancing (GB), digital mixer (DM), cascaded integrator-comb (CIC) filter and finite impulse response (FIR) filter blocks and converts the IF signals to filtered quadratures by digital homodyning. After this procedure, we

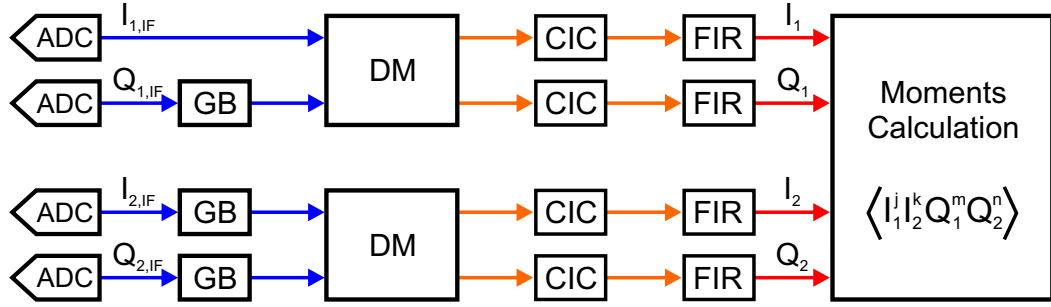


Figure 3.21: Sketch of the physical layer processing chain of the FPGA logic.

are left with 512 preprocessed samples for each of the quadratures I_1 , Q_1 , I_2 , Q_2 (cf. Fig. 3.22). For each preprocessed sample, the 63 moments $\langle I_1^j I_2^k Q_1^m Q_2^n \rangle$ with $0 < j + k + m + n \leq 4$ and $j, k, m, n \in \mathbb{N}_0$ are calculated and added to the ensemble sum registers in a parallel fashion (cf. Fig. 3.22). We note that the DM, CIC, FIR, and moments calculation (MC) blocks can be individually enabled or disabled in the logic at run time. As an example, one can bypass the MC block and stream the digitally processed quadratures for testing purposes.

In the following, we describe the different blocks of the logic (cf. Fig 3.21) in more detail. In the gain balancing blocks, $Q_{1,IF}$, $I_{2,IF}$, and $Q_{2,IF}$ are multiplied each with a constant factor to balance the signal amplitudes. We remark that all values are represented in a fixed-point format in the FPGA logic and considerable care has been taken to keep the full precision during the different mathematical operations and to prevent overflow.

The DM block digitally mixes the I_{IF} and Q_{IF} signals with a local oscillator generated by a direct digital synthesizer (DDS) applying the equations

$$\begin{aligned} I_{1,\text{mix}} &= I_{1,IF} \cos(2\pi f_{\text{DDS},1}t + \phi_{\text{cos},1}) - Q_{1,IF} \sin(2\pi f_{\text{DDS},1}t + \phi_{\text{sin},1}) \\ Q_{1,\text{mix}} &= I_{1,IF} \sin(2\pi f_{\text{DDS},1}t + \phi_{\text{sin},1}) + Q_{1,IF} \cos(2\pi f_{\text{DDS},1}t + \phi_{\text{cos},1}), \end{aligned} \quad (3.2)$$

where $f_{\text{DDS},1}$ is the frequency of the digital local oscillator and $\phi_{\text{sin},1}$, $\phi_{\text{cos},1}$ are phase-offsets for path 1. When thinking of a phasor representation of the IF signal Eq. (3.2) is equivalent to changing into a coordinate system rotating with the frequency of the digital local oscillator. Eq. (3.2) can be written for path 2 by replacing all indices “1” with “2”. We note that our logic provides two independent digital front-ends for the two paths. Consequently, our logic allows us to set different frequencies for the digital local oscillators. In practice, however, we always use an LO frequency of 11 MHz for both digital mixers. At the beginning of each new data frame, the DDS is reset, i.e., it starts at a predefined phase value. In this way, we synchronize the

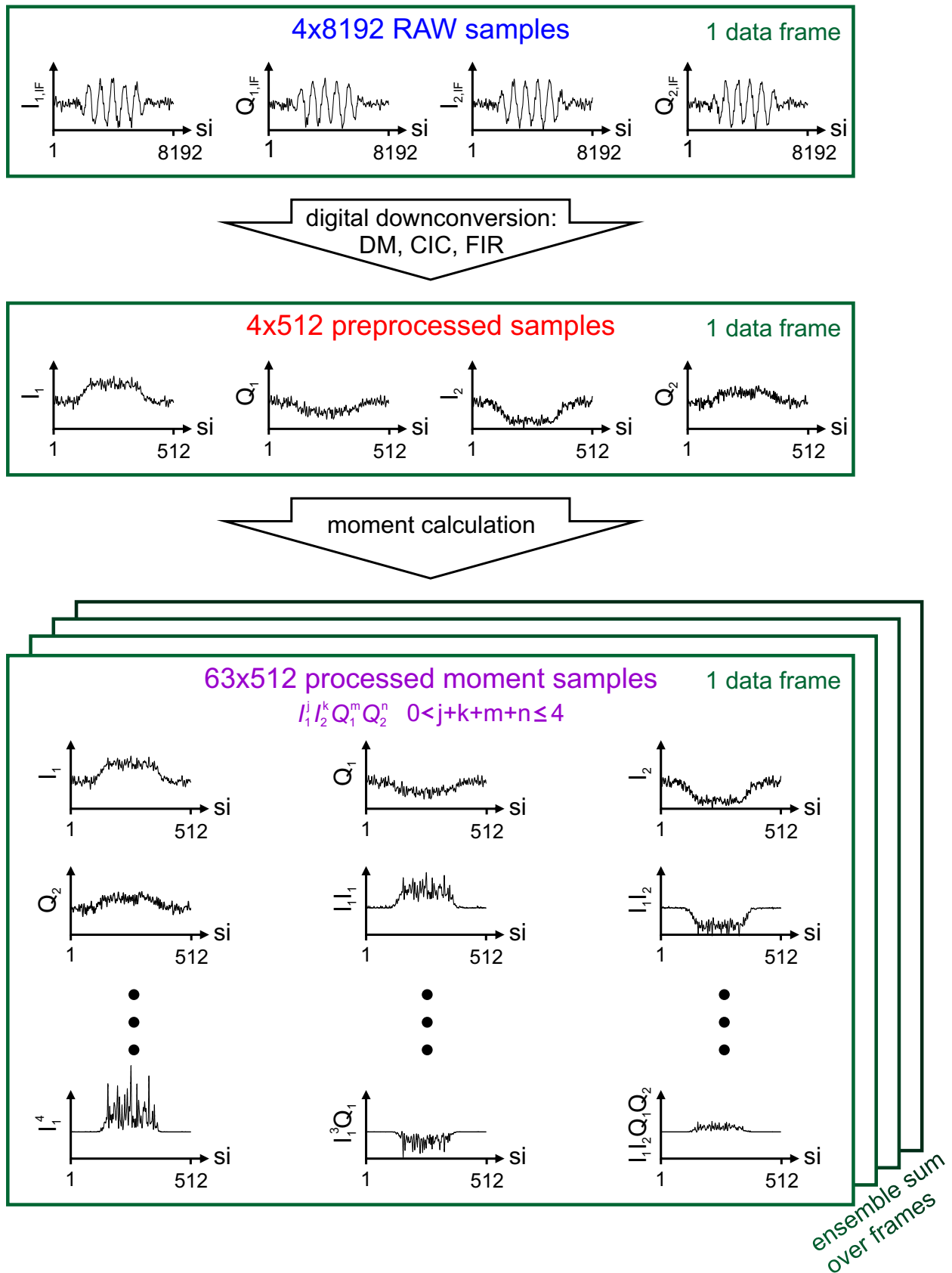


Figure 3.22: Sketch of the data processing in the FPGA logic. The traces symbolize a coherent microwave pulse with very small added amplifier noise contributions. In real experiments, the noise obscures the pulse completely in a single frame. The sample index is abbreviated as “si”. The units of the y-axes are arbitrary.

digital local oscillator to the analog LO of the heterodyne receiver. With the help of the predefined phase shifts $\phi_{\sin,1}$, $\phi_{\cos,1}$, $\phi_{\sin,2}$, $\phi_{\cos,2}$, phase imbalances of the IQ mixers are corrected and the phase difference between the two paths is fine-tuned to 180° .

After the digital mixing, we reject the sum frequency image by digital lowpass filters and restrict our measurement bandwidth further to match the mode of the squeezed state. This is important not to dilute the squeezed vacuum with non-squeezed frequency modes. For JPA signal gains up to 20 dB, the JPA bandwidth is larger than the measurement bandwidth. We use a combination of two digital filters (CIC and FIR) to achieve a narrow filter bandwidth of 489 kHz. Readers not familiar with digital signal processing are recommended to consult Ref. [137]. If one used only a FIR filter, one would need on the order of some hundred filter coefficients which may pose problems regarding numerical errors. Therefore, we reduce the sampling rate by a factor of 16 by applying a CIC down sampling filter before the FIR filter, so that only 61 filter coefficients are required. After each filter there is a divider in order to reduce the bit width again, which has been enlarged in the filter block in order to avoid overflows by multiplications and summations. These filters also determine the measurement bandwidth (noise bandwidth) of $2 \times BW_{\text{filter}} = 2 \times 489 \text{ kHz}$ of the IQ cross-correlation detector. The corresponding transmission characteristics is shown in Fig. 3.23. We note that one of the key advantages of digital filtering is that the frequency dispersion is flat and that the transmission characteristics are exactly equal for all four detection channels. We further want to mention that there is no loss of information due to the lower data rate, since the reduced sampling rate after

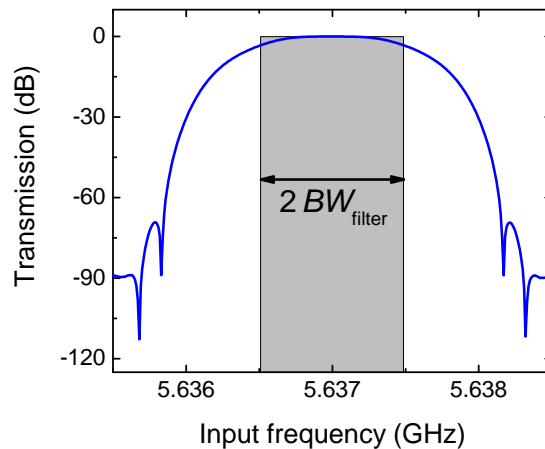


Figure 3.23: Measured transmission characteristics of the IQ cross-correlation detector.

the CIC filter is 9.5 times larger than the measurement bandwidth. An important side effect of the lower data rate is the fact that we can record longer time traces with the same fixed number of time points per moment. In our implementation we are limited to 512 samples resulting from the number of available block RAMs of the FPGA, the number of moments, and the 128 bit width of the ensemble sum registers for each sample. Usually, we measure in pulsed mode to collect data of a reference state and the actual state in the same time trace. Due to the small filter bandwidth the filter ring up time is significant. In the case without sample rate reduction, the measurement time equivalent to the 512 samples is so short that we would be limited to record only the filter transients.

As the last step of the logic, the moments up to fourth order in amplitude are calculated. For each moment and each processed sample, the ensemble sum over a specified number of frames is stored inside the FPGA. The ensemble sums of the processed moments are transferred to a computer, where they are further processed with MATLAB scripts. Due to the phase stabilization protocol, which is described in detail in Sec. 3.4.2, 10 to 60 ensemble sums each based on half a million frames are measured for a specific input state. For the reconstruction of this input state, we apply the dual-path state reconstruction method. First, each of the ensemble sums are processed. To this end, we restrict the analysis to the data portion of the frame, where the squeezed state appears (cf. Fig. 3.16). For each sample, the complex envelope moments are retrieved using Eq. (2.34) and Eq. (2.40). The dual-path corrected signal moments are reconstructed for each sample applying the formulas Eq. (2.44), Eq. (2.45), and Eq. (2.46). Thus, the dual-path correction preserves the time information. Since the moments of the states under investigation are, in principle, time independent, we use their time averages in the further analysis. Derived quantities such as the cumulants, the squeeze angle, and the level of squeezing are calculated from the time averaged corrected signal moments. This analysis is repeated for each ensemble sum. Next, the signal moments and derived measures from the different ensemble sums are averaged and the statistical uncertainty is determined. Finally, the Wigner function is reconstructed from the ensemble averaged corrected signal moments applying Eq. (2.47). For the detection and quantification of path entanglement, the output state is analyzed with the reference-state method. Again, first, each ensemble sum is analyzed. From Eq. (2.34) and Eq. (2.52), the correlations of the complex envelopes are determined from the quadrature moments. The noise terms $\langle \hat{V}_1^{k_1} (\hat{V}_1^\dagger)^{j_1} \hat{V}_2^{k_2} (\hat{V}_2^\dagger)^{j_2} \rangle$ (cf. Sec. 2.9) are retrieved for each sample of the frame, where the reference state is measured. The noise terms are time averaged

and used in Eq. (2.55) to determine the corrected output moments for each sample of the frame, where the squeezed state appears. The corrected output moments are time averaged and the witness matrix and negativity are retrieved. Next, the mean values and statistical uncertainties are determined using the results from the different ensemble sums.

Finally, we want to quantify the data throughput of our logic. Data acquisition is triggered every 100 μs . For each trigger event, 8192 consecutive points are digitized in each of the four channels at a rate of 150 MHz. As shown in Fig. 3.16, this results in a duty cycle of 54.6%. Taking this into account, we get an input data rate of 625 MB/s. When we look at the data rate at the end of the processing chain including the down sampling factor of 16, we get 2.4 GB/s, which is equivalent to a data volume of 8.4 TB in one hour of measurement time. Since the summation is done inside the FPGA memory, only a few megabyte have to be transferred to the PC. Since this takes only fractions of a second, the FPGA is the key to realtime data processing in our experiment. So far we have not optimized the duty cycle to have the same conditions in the measurements and in the tests of the logic. However, in principle, duty cycles of 99% should be achievable with our logic.

3.3.4 Calibration

In this section, we discuss the adapting of the room temperature part of the IQ cross-correlation receiver to the cryogenic setup. Furthermore, we describe calibration procedures which are important for precise measurements. More specifically, we devote ourselves to the balancing of the IQ cross-correlation detector and the determination of the gain.

Amplitude and phase balancing of the IQ cross-correlation detector

First, we check that no active part of the IQ cross-correlation receiver is suffering from compression effects. When we connect the amplification chain to the receiver, we measure with a R&S NRP-Z31 power meter at the input of the IQ mixers, i.e., after the broadband bandpass filters, a noise power of -31.5 dBm. This value is orders of magnitudes lower than the 1 dB-compression point of the IQ mixers of 4 dBm, ensuring that there are no compression effects in front of the IF amplifiers. Next, we determine the correct setting of the tunable attenuators at the input of the IF amplifiers. During this procedure, two conditions have to be kept in mind. One is to limit the gain in such a way that the ADCs are not overloaded and no clipping

occurs. The other one is not to saturate the IF amplifiers. In our current setup, the latter is the limiting condition. As input signal, we use a squeezed thermal state, where the noise source temperature is 800 mK and the JPA signal gain is 10 dB. We choose the IF attenuators to limit the output power of the IF amplifiers to 25 dB below their 1 dB-compression point of 12 dBm. In this way, we ensure that we can exclude compression effects in all of the presented measurements. Figure 3.24 shows a histogram of the IF signal amplitude. We note that our resolution is effectively two bits lower than in the case of a signal spanning the full input range. However, theoretical simulations by P. Summer in his bachelor thesis [138] under the supervision of the author have shown that effects of the bit resolution are negligible for resolutions larger than 5 bit, which is well fulfilled in our case. Furthermore, we can exclude that signals are clipped in our experiments when we consider Fig. 3.24.

After finding the coarse setting of the attenuators, we make a calibration experiment with a coherent test signal while the digital mixer and filter blocks are deactivated. We record an ensemble average to suppress the amplifier noise and consider the first moments of the $I_{IF,1,2}$ and $Q_{IF,1,2}$ signals. We fine tune the attenuators such that the amplitudes of the IF IQ signals are equal with deviations smaller than 0.1 dB. Residual imbalances are compensated by the gain blocks in the FPGA logic. By fitting sinusoids oscillating at the intermediate frequency of 11 MHz to the data, we retrieve DDS start phases to correct for phase imbalances of the IQ mixers

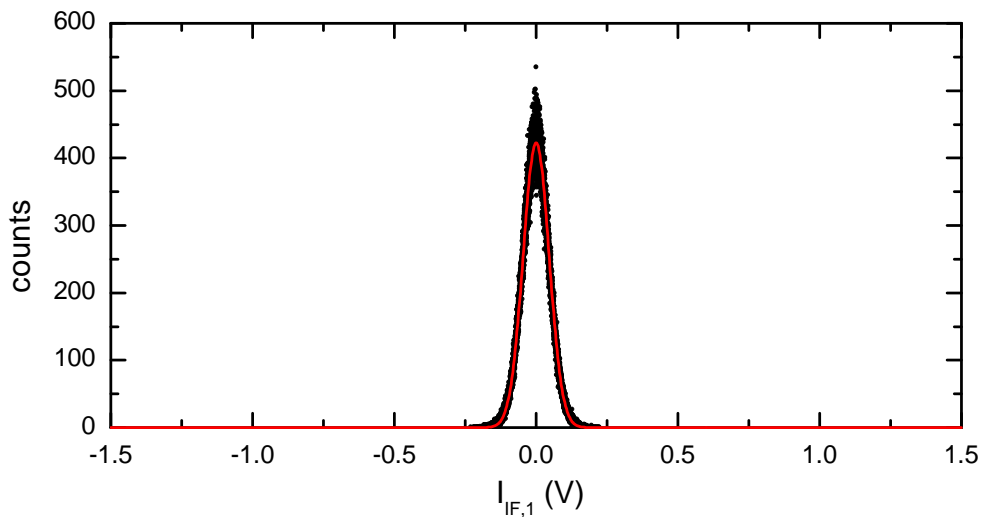


Figure 3.24: Input range of the FPGA board. Black points: Histogram of the digitized $I_{IF,1}$ signal, whereby the temperature of the noise source is stabilized to 800 mK and the JPA is operated at a signal gain of 10 dB. Red curve: Gaussian fit to the data.

and between the two paths. We note that the uncorrected phase imbalances are below 5° since the IQ mixers are of high quality. As a last step, the dividers of the digital filters have to be configured to prevent clipping. It is important to check the dividers with active digital mixing to provide the correct signal band to the filters. First, the divider of the CIC filter is set with active digital mixers and inactive FIR filters and we have determined a value of 2^{23} . Then the divider of the FIR filter is configured with active digital mixer and active CIC and we have found a value of 2^{18} . We calibrate the IQ mixers right before important measurements and after each liquid helium refill of the cryostat's dewar.

Gain calibration of the experimental setup

The coldest attenuator of the JPA signal line (cf. Fig. 3.14) represents the thermal noise source (cf. Sec 3.3.1), which is thermally weakly coupled to both the base plate and the lower step exchanger of the fridge. Its temperature can therefore be controlled in the range $T_{\text{att}} = 50 - 700$ mK, while all other components retain a stable temperature. This attenuator constitutes a broadband microwave black body emitter, which is used to calibrate the gains of the amplification paths in a Planck experiment [58]. The total power of each amplification path detected at the ADCs is

$$\begin{aligned} P_i(T_{\text{att}}) &= \frac{\langle I_i^2 \rangle + \langle Q_i^2 \rangle}{R} \\ &= \frac{\kappa G_i}{R} \left[\frac{1}{2} \coth \left(\frac{hf_0}{2k_B T_{\text{att}}} \right) + n_i \right], \quad i = 1, 2 \end{aligned} \quad (3.3)$$

where $R = 50 \Omega$ is the input resistance of the ADCs and $k_B = 1.38 \times 10^{-23}$ J/K the Boltzmann constant. The product of the gain G_i and the photon number conversion factor $\kappa \equiv R \times 2 \times BW_{\text{filter}} \times hf_0 = 1.83 \times 10^{-16}$ V² relates the measured auto-correlations $\langle I_i^2 \rangle$ and $\langle Q_i^2 \rangle$, which have units of V², to the number of photons of frequency f_0 emitted by the attenuator. The gain G_i and the number of noise photons added by each amplification path, n_i , are retrieved from fitting Eq. (3.3) to the experimentally recorded auto-correlations. For pedagogical reasons, all formulas given in Sec. 2.6 assume equal gains and losses for the I and Q branches within each path. However, in the actual evaluation of the data, we do not make this assumption. We model the losses with beam splitters and also account for temperature gradients along our cables. In this way, we make individual fits for the dependence of $\langle I_1^2 \rangle$, $\langle I_2^2 \rangle$, $\langle Q_1^2 \rangle$, and $\langle Q_2^2 \rangle$ on T_{att} . As an example, we show data and fit for

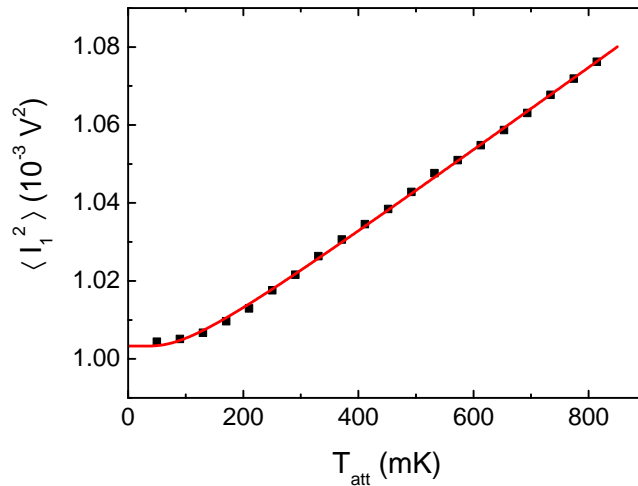


Figure 3.25: Gain calibration using thermal input states. Dependence of the second moment $\langle I_1^2 \rangle$ on the temperature of the attenuator temperature T_{att} . Black symbols: data. Red line: fit.

$\langle I_1^2 \rangle$ in Fig. 3.25. From this figure, we immediately see that the number of thermal photons in the mode f_0 is negligible at 40 – 50 mK. Furthermore, with a total loss of 1.8 dB between attenuator and beam splitter input (upper bound; from calibration measurements; dominating source of error), we retrieve $G_{\text{d1}}/2 = 116.5$ dB and $n_{\text{d1}} = 24.3$ photons. Here, the index “d” denotes that $G_{\text{d1}}/2$ and n_{d1} are referred to the input of the hybrid ring. From our reference-state analysis described in Sec. 2.9, we obtain, with respect to the beam splitter output ports, noise temperatures of 3.00 K and 3.27 K for the two amplification paths. Considering that our beam splitter reduces the input signal by 3.5 dB, the value of 3.00 K is in very good agreement with that of $10^{-0.35} n_{\text{d1}} h f_0 / k_B = 2.94$ K.

3.4 Stability of the experimental setup

In this section, we present methods applied to improve the stability of the experimental setup. The latter is an important prerequisite to successfully run experiments with long averaging times and sensitivities on the quantum level. Therefore, tremendous efforts have been taken to analyze the stability, identify sources for spurious fluctuations and to suppress them. In Sec. 3.4.1, we consider the stabilization of the amplifier gain and cable losses. Finally, in Sec. 3.4.2, we discuss a protocol for the stabilization of phase-sensitive microwave states such as coherent and squeezed states.

3.4.1 Stabilization of amplifier gain and cable losses

In the formalism of the dual-path state reconstruction method and in that of the reference-state method, the gain is assumed to be constant. In practice, this gain is a combination of the gains of the cryogenic and room temperature amplifiers and the losses of the other components building the amplification and detection chain. In reality, disturbances acting on the different parts of the chain can result in gain fluctuations. In the following, we give an overview on measures taken to stabilize the gain.

- Some of the microwave amplifiers dissipate so much power that their operation demands for cooling. For this reason, the amplifiers are water-cooled applying cooling wings originally designed for computer components. In the experiments with classical mixtures of microwave signals, tap water was used for this purpose. However, the temperature of tap water depends on the consumption of the whole institute which is not constant. Therefore, we have replaced it for the path entanglement experiments by a closed cooling cycle managed by a Van der Heijden Cool-Care, which provides a temperature stability of $\pm 0.1^\circ\text{C}$ for the cooling water.
- Microwave devices are sensitive to temperature fluctuations. For example, thermal expansion results in a change of the transmission phase of microwave cables or the transmission of electronic attenuators depends also on their temperature. To suppress variations of the room temperature during the day and to remove the heat generated by the measurement rack and computers (on the order of several kW) the laboratory is equipped with a split-type air conditioning system. It is capable of cooling and heating with a temperature stability of $\pm 1^\circ\text{C}$.
- The power supplies of cryogenic and room temperature amplifiers have been placed in compartments with home-made temperature stabilization realized by fans and a temperature controller. The boxes are isolated from the environment with foam material.
- During the reconstruction of the cryostat system to increase the sample space, a dewar with a larger helium reservoir is installed. This has the positive side effect that the operation time of the fridge per helium refill has been prolonged and effects caused by the continuous dropping of the helium level reduced.

- The cryogenic and part of the room temperature setup including the first two microwave amplification stages are located inside a shielded room, which suppresses spurious signals up to 20 GHz.
- The operation point and, thus, the gain of the JPA are sensitive to the magnetic field threading the SQUID loop. Variations of this field are reduced by three layers of Mu-metal at room temperature and a Cryoperm shield surrounding the inner vacuum chamber at 4.2 K. For details on the superconducting coil system and its persistent operation mode, we refer the reader to Sec. 3.2.3.

3.4.2 Phase stabilization protocol

The phase stability between signal/pump and local oscillator is better than $\pm 0.3^\circ$ for 5×10^5 traces. Hence, reconstructions based on such a number of averages exhibit very good phase control. However, for quantifying the path entanglement properties, an average over $8 \times 10^6 - 3 \times 10^7$ traces is necessary to reduce the influence of the noise added by each amplification path to a negligible amount. In such measurements, the phase stability of our setup is not sufficient. For this reason, we record the data in 5×10^5 trace portions and adjust the relative phase between signal/pump and local oscillator in a way that phase drifts are compensated. The effective stabilization of the phase is shown in Fig. 3.26. With active phase stabilization the standard deviation of the phase error is 0.3° , whereas in this measurement the maximum phase drift without stabilization would have been 6.6° .

After discussing the relevant setups and experimental techniques, which empower us to study propagating quantum microwaves and path entanglement, we analyze the obtained results in the next chapters.

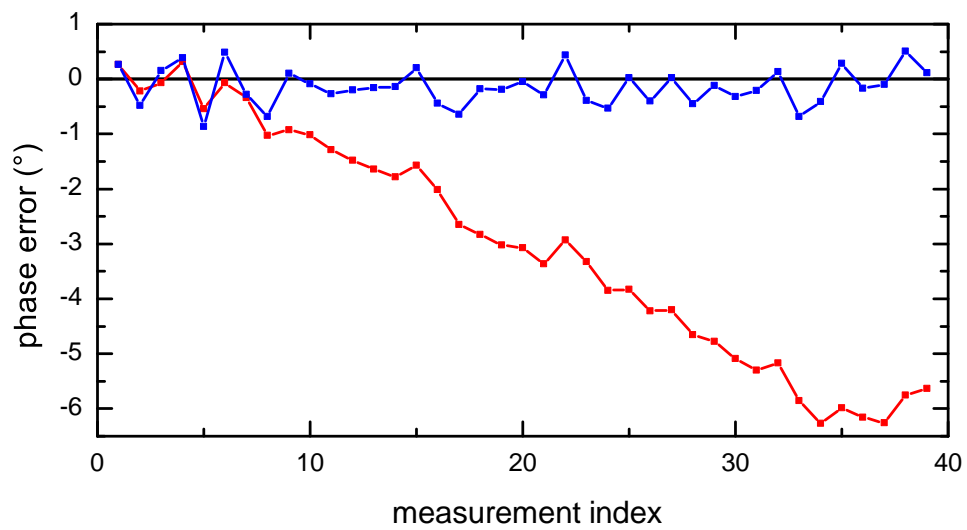


Figure 3.26: Stabilization of squeezed state phase applying our protocol. The JPA produces a squeezed vacuum state (signal gain: 10 dB). Blue curve: Plot of the phase error defined as the deviation of the measured phase from the set value of 45° , where the phase is stabilized using our protocol. We note that there are more negative than positive values in the phase error curve. Red curve: Cumulative sum of the phase error representing the evolution of phase if it is not stabilized. The phase drift is clearly visible.

Chapter 4

Detection of weak propagating microwaves

In this chapter, we present our results on the reconstruction of weak propagating microwaves retrieved with the experimental setups and methods discussed in the last chapter. The chapter is organized as follows. First, in Sec. 4.1, we investigate thermal microwave states with dual-path setups. These experiments lead to the fundamental observation that our beam splitters are working with signals on the quantum level and are, independently of the external configuration, always four-port devices. Furthermore, the cross-over from weak thermal to vacuum fluctuations is investigated with a new technique called Planck spectroscopy. These results are important for the following experiments as they provide an elegant calibration technique and give first hints that the beam splitter is a suitable device for experiments on quantum microwaves. Subsequently, we study the applicability of the dual-path method in proof-of-principle experiments. In Sec. 4.2, we demonstrate the amplifier noise suppression which lies at the heart of the dual-path method. In Sec. 4.3 we infer time-dependent variances and non-zero third moments of statistical mixtures of coherent states with few photons.

4.1 Planck spectroscopy and quantum noise of microwave beam splitters

In the following, we present results of two experiments demonstrating the successful application of our setup to the characterization of weak thermal states. The content of this section has been published in Ref. [58]. In a first experiment de-

noted as Planck spectroscopy we analyze the microwave black body radiation emitted by a $50\ \Omega$ -load resistor as a function of temperature in the frequency regime $4.7 \leq f \leq 7.1$ GHz. Besides confirming that the mean thermal photon number follows Bose-Einstein statistics [25, 90, 105, 139], our data directly show that the quantum crossover temperature T_{cr} shifts with frequency as $T_{\text{cr}} = hf/2k_{\text{B}}$, as it is expected from quantum mechanics because of the existence of vacuum fluctuations. In a second experiment, we use weak thermal states for a detailed experimental characterization of microwave beam splitters at the quantum level. This task is particularly important because microwave beam splitters are key elements in a variety of quantum-optical experiments such as Mach-Zehnder and Hanbury Brown–Twiss interferometry [90, 140].

Figure 4.1 shows the equivalent circuits of the internal and external noise sources for the two types of beam splitters used in our experiments. The experimental setup has been discussed in Sec. 3.1 in detail and we refer the reader to Fig. 3.5 and Fig. 3.6 for sketches of the setup.

As an ideal black body source emitting thermal microwave states [141], we use $50\ \Omega$ -loads whose temperature T can be varied between 20 and 350 mK and measured with a RuO thermometer. The associated quantum voltages can be expressed as $\hat{V}_{\text{th}}^A = V_0(\hat{a}^\dagger + \hat{a})$ and $\hat{V}_{\text{th}}^C = V_0(\hat{c}^\dagger + \hat{c})$, where $V_0^2 = 4BR_0hf/2$, $R_0 = 50\ \Omega$, \hat{a}^\dagger , \hat{c}^\dagger and

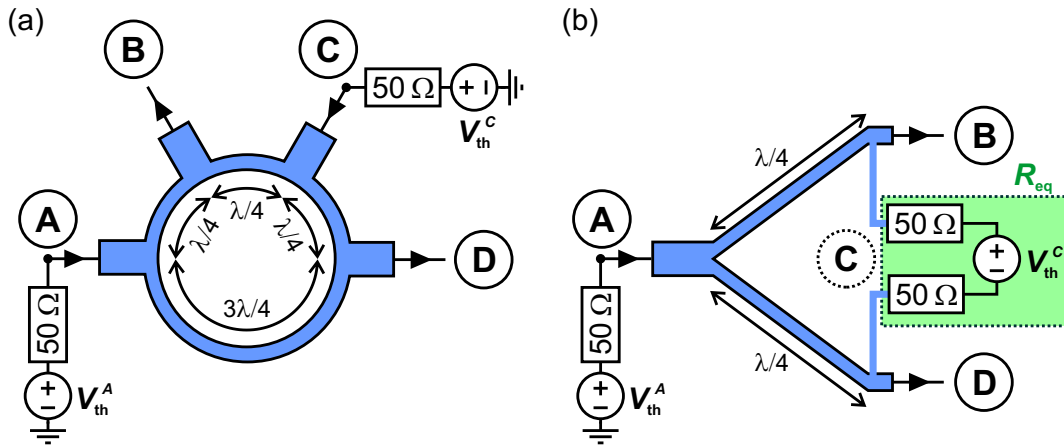


Figure 4.1: Equivalent circuits of the microwave beam splitters. The ports B and D are connected to the inputs of the amplification and detection chains. (a) 180° -hybrid ring (HR). (b) Wilkinson power divider (WPD). For the WPD, port C represents a hidden internal port and R_{eq} an internal distributed resistor, which can be modeled as two equivalent $50\ \Omega$ -loads adding correlated thermal noise via the hidden port C only. Reprinted adopted figure with permission from Ref. [58]. Copyright (2010) by the American Physical Society.

\hat{a} , \hat{c} are bosonic creation and annihilation operators, and B is the bandwidth. The thermal microwave signal is fed into the input ports of a 3 dB beam splitter. We perform experiments on two different beam splitter realizations: a 180° -hybrid ring (HR) with four external ports [cf. Fig. 4.1(a)] and Wilkinson power divider (WPD) with three external ports [cf. Fig. 4.1(b)]. For the WPD, an internal distributed resistor R_{eq} shunting the output ports B and D provides isolation between those ports and impedance matching for port A. In addition, an external $50\ \Omega$ -load is attached to input port A. For the HR, $50\ \Omega$ -loads are attached to both input ports A and C. The input-output relations of the HR are $\hat{V}_B = (\hat{V}_A + \hat{V}_C)/\sqrt{2}$ and $\hat{V}_D = (-\hat{V}_A + \hat{V}_C)/\sqrt{2}$ [103]. We remark that the WPD, although appearing to be a three-port device, has to be treated quantum-mechanically as having an additional “hidden” internal fourth port C, see Fig. 4.1(b), ensuring energy conservation and commutation relations. In this case the input-output relations are $\hat{V}_B = (\hat{V}_A - \hat{V}_C)/\sqrt{2}$ and $\hat{V}_D = (\hat{V}_A + \hat{V}_C)/\sqrt{2}$. Regarding thermal noise, the internal resistor R_{eq} can be modeled as two equivalent matched $50\ \Omega$ -loads. The noise added by these thermal noise sources in the two arms acts as if it were correlated. For a detailed derivation of this model based on circuit theory, we refer the reader to Ref. [105]. If the input signal at port A is large, this additional noise can be neglected and the WPD can be formally treated as a three-port device.

As shown in Fig. 3.5 and Fig. 3.6, the output ports B and D of the beam splitter are connected to two symmetric amplification and detection chains. The noise added by the linear HEMT amplifiers is the dominating amplifier noise in each detection channel and is expressed by $\hat{\chi} = V_0(\hat{w}^\dagger + \hat{w})$, where \hat{w}^\dagger and \hat{w} are bosonic creation and annihilation operators [81]. Since we use a double-sideband receiver, the total bandwidth B in our experiment is twice the bandwidth of the bandpass filter $B_F = 26\ \text{MHz}$.

According to Nyquist [142], the black body radiation emitted by a resistor R_0 within the frequency band of width B and center frequency $f = f_{\text{LO}}$ is given by $\langle V_{\text{th}}^2 \rangle / R_0 = 4B \langle n_{\text{th}} \rangle hf$. Here, $\langle n_{\text{th}} \rangle$ is the average thermal photon population. It has been shown that for conductors with a large number of electronic modes the statistics of the emitted photons is given by a Bose-Einstein distribution [141]. In this case, the well-known result $\langle V_{\text{th}}^2 \rangle / R_0 = 4B \frac{hf}{2} \coth(hf/2k_B T)$ is obtained. The power emitted into a perfectly matched circuit with characteristic impedance Z_0 is reduced by a factor of $1/4$ due to voltage division. Together with the beam splitter input-output relations of the HR, the signal components C_1 and C_2 are given by $C_1 = \sqrt{G_1}(\alpha V_{\text{th}}^A + \beta V_{\text{th}}^C + \chi_1)$ and $C_2 = \sqrt{G_2}(-\alpha V_{\text{th}}^A + \beta V_{\text{th}}^C + \chi_2)$. Here, $G_1 \simeq G_2$

is the total power gain of the amplification chains, $\alpha = \beta = 1/2\sqrt{2}$, and χ_1 and χ_2 are the independent noise contributions of the amplifiers. Equivalently, for the WPD we obtain $C_1 = \sqrt{G_1}(\alpha V_{\text{th}}^A - \beta V_{\text{th}}^C + \chi_1)$ and $C_2 = \sqrt{G_2}(\alpha V_{\text{th}}^A + \beta V_{\text{th}}^C + \chi_2)$. We note that V_{th}^A , V_{th}^C and $\chi_{1,2}$ are classical realizations of the operators given above. By recording a large number of 1 μs -long time traces ($\sim 10^6$), the auto- and cross-correlation functions $\mathcal{R}_{ii}(\tau) = \langle C_i^*(t + \tau) C_i(t) \rangle / Z_0 = \sigma_{ii}^2 \text{sinc}(B\tau) / Z_0$ and $\mathcal{R}_{ij}(\tau) = \langle C_i^*(t + \tau) C_j(t) \rangle / Z_0 = \sigma_{ij}^2 \text{sinc}(B\tau) \cos(\varphi_{\text{LO}}) / Z_0$, respectively, can be calculated ($i, j = 1, 2$). Here, φ_{LO} is the phase difference between the LO signals of the two downconversion mixers. Since $\langle C_i(t) \rangle = 0$ for thermal states, the auto- and cross-correlation functions are equal to the auto-variance $\mathcal{C}_{ii}(\tau) = \mathcal{R}_{ii}(\tau) - \langle C_i \rangle^2$ and cross-variance $\mathcal{C}_{ij}(\tau) = \mathcal{R}_{ij}(\tau) - \langle C_i \rangle \langle C_j \rangle$, respectively. Here, τ is the time shift between two traces being correlated, and σ_{ii}^2 and σ_{ij}^2 are the variance and covariance of the voltage signals C_1 and C_2 .

4.1.1 Planck spectroscopy

We first discuss the Planck spectroscopy experiment [105, 139]. Here, we use only a single amplification chain and determine the auto-correlation function $\mathcal{R}_{11}(\tau)$ or $\mathcal{R}_{22}(\tau)$. Figure 4.2(a) shows the measured $\mathcal{R}_{11}(\tau)$ curve obtained for $T = 30$ mK using a WPD. A very similar result is obtained for $\mathcal{R}_{22}(\tau)$ [cf. Fig. 4.3(d)]. Fitting the data to $\mathcal{C}_{11}(\tau)$ allows us to extract the measurement bandwidth $B \simeq 52$ MHz. Assuming that the signal contributions V_{th}^A and V_{th}^C due to the two load resistors and the noise χ_i of the HEMT amplifier are independent, we can add up their variances and obtain $\mathcal{R}_{ii}(0) = \mathcal{C}_{ii}(0) = \sigma_{ii}^2 = \langle C_i^2 \rangle / Z_0 = G_i [(\alpha^2 + \beta^2) \langle V_{\text{th}}^2 \rangle + \langle \chi_i^2 \rangle] / Z_0$. With $hf/2k_B T_{i,\text{HEMT}} \ll 1$ we can introduce a classical noise temperature $T_{i,\text{HEMT}}$ for the amplifiers and obtain

$$\mathcal{R}_{ii}(0) = G_i^* B \left[\frac{hf}{2} \coth \left(\frac{hf}{2k_B T} \right) + k_B T_{i,\text{HEMT}}^* \right], i \in \{1, 2\}. \quad (4.1)$$

Here, $G_i^* = \gamma G_i$ is the effective gain, G_i the total gain of amplification chain i and $T_{i,\text{HEMT}}^* = T_{i,\text{HEMT}} / \gamma$ is the effective noise temperature representing the amplifier noise temperature relative to the input of the WPD. For both HR and WPD, $\gamma = 4(\alpha^2 + \beta^2) = 1$.

Figure 4.2(b) shows the measured variance $\mathcal{R}_{11}(0)$ as a function of T for $f = 5.3$ GHz in the case of a WPD. In the experiments, T was varied between approximately 20 and 350 mK by means of a resistive heater and continuously monitored with a RuO thermometer. The measured variance is close to a Planck function

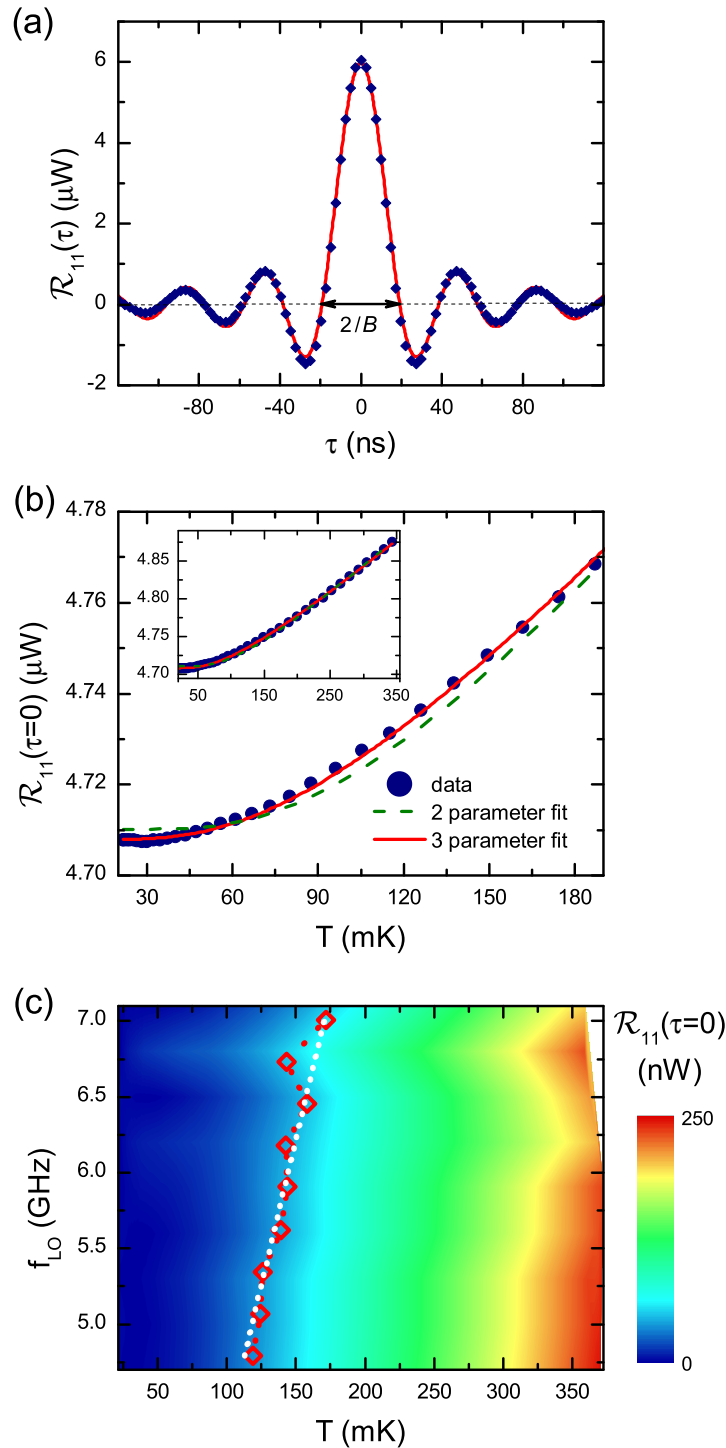


Figure 4.2: Planck spectroscopy of thermal microwave states using a WPD. (a) Auto-correlation function $\mathcal{R}_{11}(\tau)$ at $f = 5.3$ GHz. The line is a fit to the data (symbols). (b) Temperature dependence of the variance $\mathcal{R}_{11}(\tau = 0)$ (Planck function) at $f = 5.3$ GHz. The dashed and full lines are obtained by two- and three-parameter fits, respectively, to the data (symbols). The gain is 90 dB. Inset: Wider temperature range. (c) Planck spectroscopy. Contour plot of $\mathcal{R}_{11}(\tau = 0)$ versus T for different f . The data have been corrected for the frequency-dependent amplifier gain, and the offset due to vacuum and amplifier noise has been subtracted. Symbols and dotted line: Measured and expected quantum crossover temperatures $T_{\text{cr}} = hf/2k_B$, respectively. Reprinted rearranged figure with permission from Ref. [58]. Copyright (2010) by the American Physical Society.

and reproduces the expected crossover temperature from thermal to vacuum noise, $T_{\text{cr}} = hf/2k_B$. A fit of Eq. (4.1) to the data using G_1^* and $T_{1,\text{HEMT}}^*$ as free parameters yields $G_1^* \simeq 90$ dB and $T_{1,\text{HEMT}}^* \simeq 6$ K. The slight deviations between the data and the two-parameter fit can be understood by taking into account that the effective electronic temperature T_{eff} of the load resistors at ports A and C may differ by a small amount δT . By using δT as the third fitting parameter, the solid line in Fig. 4.2(b) is obtained, demonstrating excellent agreement with the experimental data. The δT values obtained by fitting the data are reasonably small and typically range between 1 and 10 mK. The large bandwidth of the HEMT amplifier allows us to perform measurements at frequencies between 4.7 and 7.1 GHz. The result of such Planck spectroscopy is shown in Fig. 4.2(c). Clearly, the crossover temperature T_{cr} shifts to higher values with increasing frequency. Because of the finite uncertainty in T_{eff} , we derive an effective crossover temperature $T_{\text{cr}} + \delta T_{\text{cr}}$, which again slightly deviates from the theoretically expected value, $T_{\text{cr}} = hf/2k_B$ [cf. Fig. 4.2(c)]. The magnitude δT_{cr} quantifies the measurement fidelity $\mathcal{F} \equiv 1 - |\delta T_{\text{cr}}|/T_{\text{cr}}$ of our setup for vacuum fluctuations. Notably, for the entire frequency range $\mathcal{F} \gtrsim 95\%$. In summary, our Planck spectroscopy experiments not only provide clear evidence for the Bose-Einstein statistics of photons emitted by a conductor in the few-photon limit, but also directly demonstrate the frequency dependence of the crossover temperature characterizing the transition between thermal-noise-dominated and vacuum-noise-dominated regime.

4.1.2 Quantum noise of microwave beam splitters

We next turn to the analysis of the microwave beam splitters. Figures 4.3(a)–4.3(d) show the entire correlation matrix. The off-diagonal elements are cross-correlation functions measured choosing φ_{LO} in order to obtain a maximum positive result. This guarantees that the signals associated with the two detection channels are skewed in phase and no unwanted decorrelation is introduced. Since the signal contributions of the thermal noise sources and the amplifier noise are independent, all cross-correlations vanish, e.g., $\langle \hat{\chi}_1 \hat{\chi}_2 \rangle = \langle \hat{\chi}_1 \rangle \langle \hat{\chi}_2 \rangle = 0$. Then, for $\alpha^2 = \beta^2 = 1/8$ the covariance $\mathcal{R}_{12}(0) = \mathcal{C}_{12}(0) = \sigma_{12}^2$ is obtained to

$$\mathcal{R}_{12}(0) = \frac{hf}{4} G_{12} B \left[\coth \left(\frac{hf}{2k_B T_A} \right) - \coth \left(\frac{hf}{2k_B T_C} \right) \right] \quad (4.2)$$

with the power cogain $G_{12} = \sqrt{G_1} \sqrt{G_2}$. We note that the temperatures T_A and T_C of the load resistors at port A and C, respectively, are identical only in the ideal

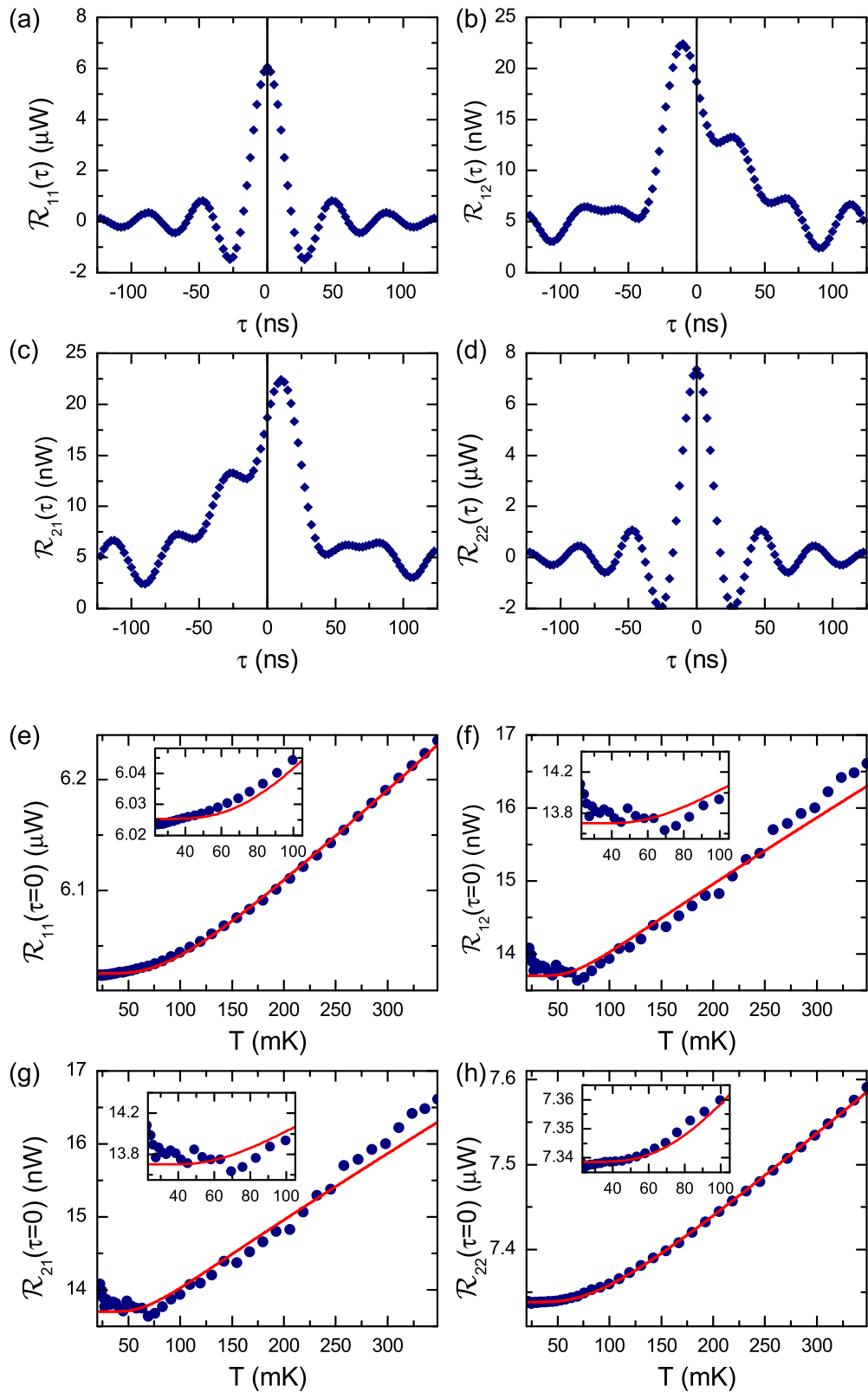


Figure 4.3: Full correlation function and covariance matrices measured at $f = 5.0$ GHz using a WPD ($G_1 \simeq 90.5$ dB, $G_2 \simeq 91.3$ dB, and $G_{12} \simeq 90.9$ dB). (a)–(d) $\mathcal{R}_{ii}(\tau)$ and $\mathcal{R}_{ij}(\tau)$ measured at $T = 30$ mK. (e)–(h) Temperature dependence of $\mathcal{R}_{ii}(0)$ and $\mathcal{R}_{ij}(0)$. The lines are fits to the data (symbols) including a global offset of approximately 0.2 photons in the measurement bandwidth. Reprinted rearranged figure with permission from Ref. [58]. Copyright (2010) by the American Physical Society.

case, resulting in $\mathcal{R}_{12}(0) = 0$ for the HR and WPD. However, in our experiments the temperatures differ slightly, $T_A = T_C(1 - \eta)$. Figures 4.3(e)–4.3(h) show the covariance matrix as a function of T for $f = 5.0$ GHz and a WPD. The diagonal matrix elements $\mathcal{R}_{11}(0)$ and $\mathcal{R}_{22}(0)$ represent variance measurements and are analogous to the results shown in Fig. 4.2(b). The off-diagonal elements, instead, represent covariance measurements. It is evident that both the offset signal at 20 mK and the signal span between 20 and 350 mK for the covariance is reduced by approximately two orders of magnitude as compared to the variance. This suggests that there is a cancellation of both the amplifier noise and the signal when measuring the covariance. The former is due to the fact that the amplifier noises are uncorrelated. The latter is expected from Eq. (4.2). In order to prove this conjecture, we use Eq. (4.2) to fit the experimental data by using the cogain determined from the variance data. Furthermore, we set $T_A = T$, where T is the temperature measured by the thermometer, and use η as a free fitting parameter. We thus obtain the red curves in Figs. 4.3(f) and 4.3(g), which are in excellent agreement with the data. We obtain η values of less than 2% amounting to temperature differences of a few millikelvin. Since Eq. (4.2) explicitly assumes the existence of four ports, the perfect fit of the experimental data provides clear evidence that the WPD effectively behaves as a four-port device. In the quantum limit, the internal fourth port adds vacuum noise to any given input signal. In order to confirm our findings on the WPD, we have measured the temperature dependence of the variance and covariance also for a HR (cf. Fig. 4.4), which is a beam splitter with four external ports. The covariance

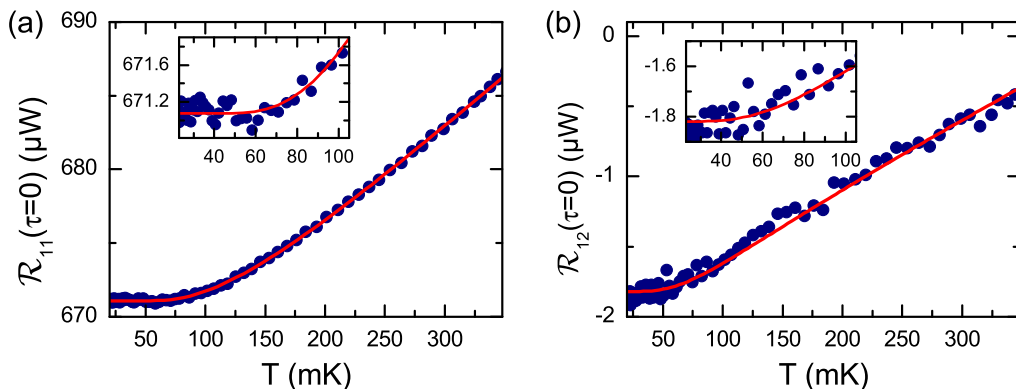


Figure 4.4: Temperature dependence of the (a) variance $\mathcal{R}_{11}(0)$ and (b) covariance $\mathcal{R}_{12}(0)$ measured at $f = 5.85$ GHz using a HR. The different power scale compared to Figs. 4.3(e)–(h) results from a different amplifier configuration resulting in a gain of 110 dB. Reprinted rearranged figure with permission from Ref. [58]. Copyright (2010) by the American Physical Society.

data of Fig. 4.4(b) are in very good agreement with the fitted curve obtained from Eq. (4.2). This clearly demonstrates that, both the HR and WPD are characterized by the same fundamental quantum-mechanical behavior.

In conclusion, we apply a correlation function analysis of the field amplitudes to characterize black body radiation and the quantum properties of microwave beam splitters. Our Planck spectroscopy experiments show that the mean thermal photon number emitted by a load resistor follows Bose-Einstein statistics and that the crossover temperature from a thermal-noise-dominated to a vacuum-noise-dominated regime shifts with frequency according to the relation $T_{\text{cr}} = \hbar\omega/2k_B$. This result can be interpreted as an indirect measurement of microwave vacuum fluctuations. Moreover, we show that a WPD, a beam splitter with only three external ports, must be considered as a four-port device at the quantum level and adds at least the vacuum noise to any input signal.

4.2 Dual-path noise suppression

In this section, we demonstrate the cancellation of the amplifier noise by applying cross-correlation techniques. The content of this and the following section has been published in Ref. [57].

We first emphasize the practical relevance of our dual-path theory (cf. Sec. 2.5) by conducting proof-of-principle experiments with weak classical microwaves. For a detailed description of the setup, we refer the reader to Sec. 3.1. As signals, we use pulsed coherent microwaves with a frequency of 5.85 GHz generated by a source at room temperature. A series of cold attenuators ensures that the thermal noise at the signal port of the hybrid ring is restricted to that of an effective $50\ \Omega$ -termination at the base temperature of 300 mK¹. The source power at the input of the hybrid ring P_{in} is related to an equivalent number of signal photons on average (POA) (cf. Sec. 3.1.1). Figure 4.5(a) shows the ensemble average of a typical signal used in our experiments. The pulse duration of 1 μs mimics standard cavity decay times in circuit QED experiments [85].

We first demonstrate the suppression of the amplifier noise via cross-correlations. The auto-variance $\langle C_1^2 \rangle - \langle C_1 \rangle^2$ of an ensemble of 10^7 pulses is depicted in Fig. 4.5(b), where one immediately notices the large offset of $35.7 \times 10^{-3} \text{ V}^2$ due to the amplifier noise. In the cross-variance $\langle C_1 C_2 \rangle - \langle C_1 \rangle \langle C_2 \rangle$, this offset is efficiently suppressed by

¹Due to a blockage of the condenser line, the base temperature in this experiment is 300 mK. The loss of the input line has been calibrated before the blockage occurred.

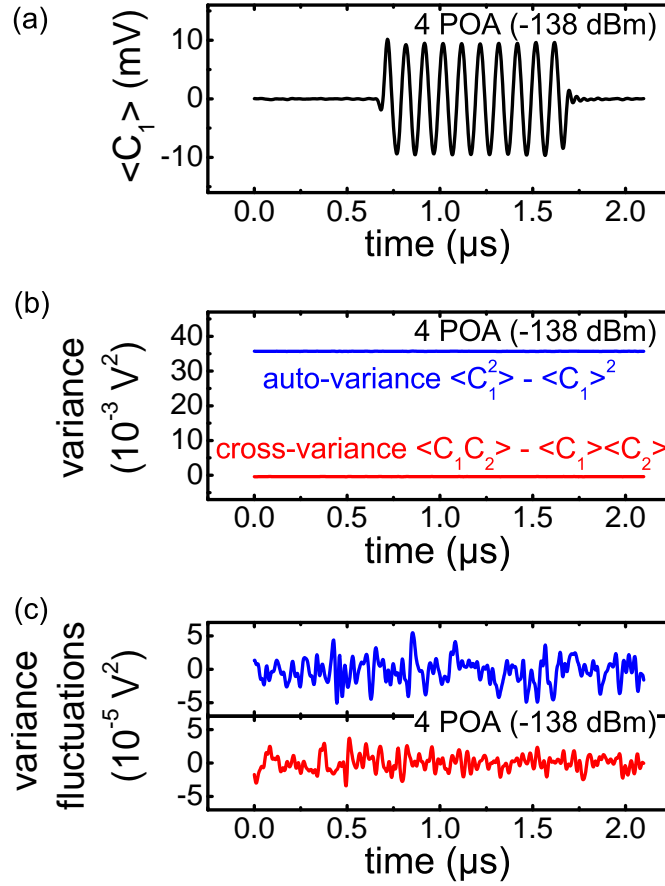


Figure 4.5: Amplifier noise suppression. The signal consists of coherent microwave probing pulses (10^7 traces averaged). (a) Mean value of downconverted signal (10 MHz). (b) Auto-variance (blue) and cross-variance (red). (c) Auto-variance (blue) and cross-variance (red) fluctuations, obtained by subtracting the respective time averages. Reprinted rearranged figure with permission from Ref. [57]. Copyright (2010) by the American Physical Society.

two orders of magnitude. As expected for a coherent signal, the variances are flat and do not allow us to distinguish between the on- and off-regions of the pulses. The fluctuations of the variance signals are smaller for the cross-correlation than for the auto-correlation by a factor of 1.6; cf. Fig. 4.5(c).

Next, we prove that our method works efficiently at the quantum level, i.e., for signals of few photons on average. To this end, we investigate the resolution limits of the constituents of the variance, mean value, and cross-product. In Fig. 4.6(a), the root mean square power inside the pulse region is plotted against the signal power at the input of the hybrid ring. We find a large dynamic range of the mean value extending over six decades down to 0.001 POA. This means that pulse energies as low as 3.7×10^{-26} J (0.01 POA) are still very well detectable. The power dependence of

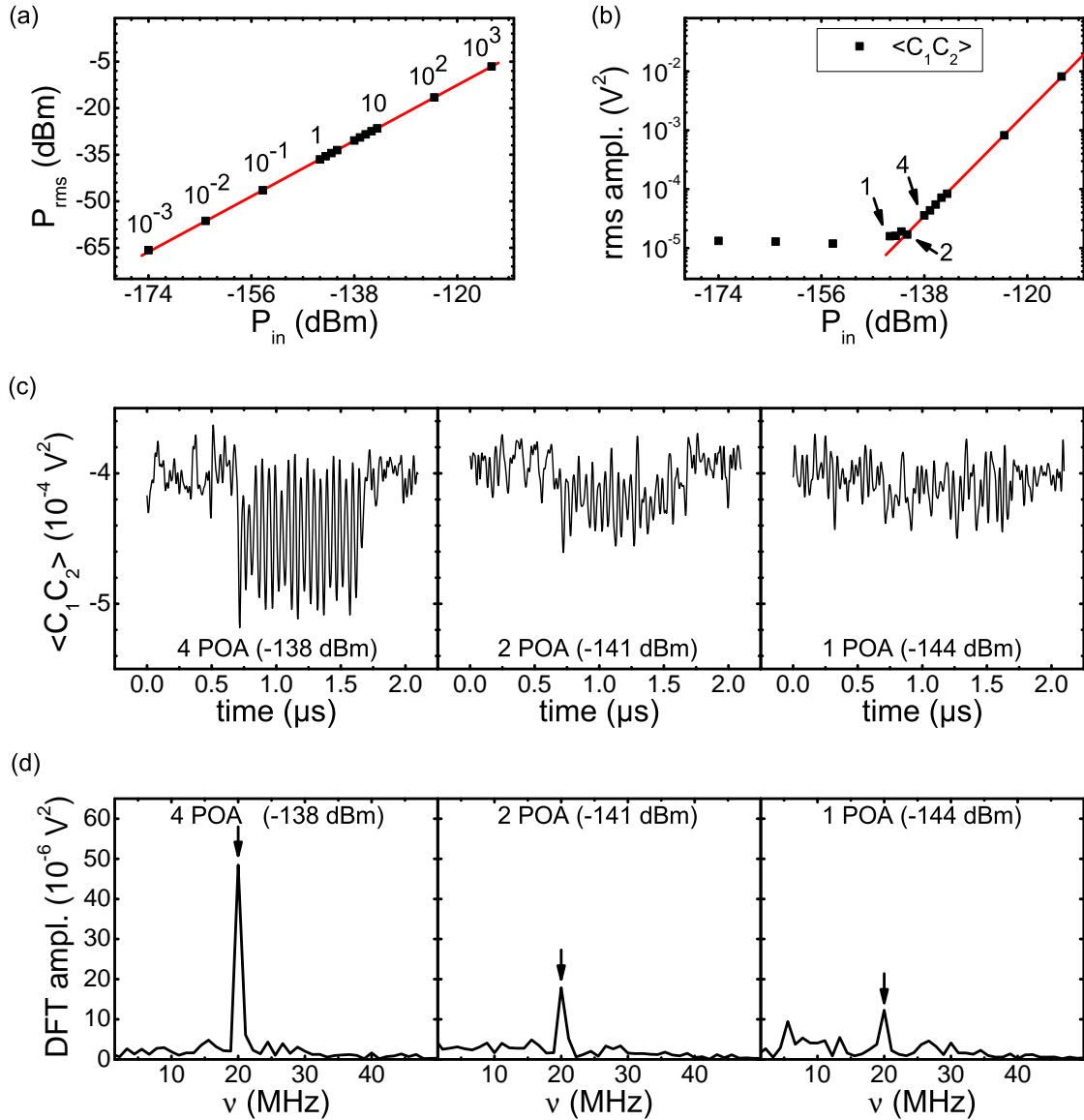


Figure 4.6: Dynamic range investigated with coherent pulses with various power levels (10^7 traces averaged). (a) Dynamic range of the mean value. P_{rms} is the root mean square power at the digitizer. The numbers above the data points indicate the number of photons on average. (b) Dynamic range of the cross-product $\langle C_1 C_2 \rangle$. The arrows indicate the values obtained from the time traces shown in (c). The rms amplitude inside the pulse region is calculated after subtracting the time average from each data point. (c) Power dependence of the cross-product time traces in the limit of few photons on average. (d) Discrete Fourier transform (DFT) of the pulse region of the traces shown in (c). The arrows indicate the 20 MHz peaks. Reprinted rearranged figure with permission from Ref. [57]. Copyright (2010) by the American Physical Society.

the cross-product $\langle C_1 C_2 \rangle$ is displayed in Figs. 4.6(b)–(d). Down to 2 POA, the pulse region is clearly visible [Fig. 4.6(c)]. For 1 POA, a Fourier transform [Fig. 4.6(d)] reveals that the signal component can still be identified. However, the associated peak has approximately the same amplitude as the largest noise peak in the spectrum. Hence, the detection limit of the cross-product [cf. also Fig. 4.6(b)] and therefore the one of the cross-variance is 1–2 POA. We note that this is not a fundamental limit, but is rather due to technical issues such as the filter bandwidth, isolation between the chains or the ensemble size. In order to study statistical effects, numerical simulations have been carried out by Phillip Summer in his Bachelor thesis [138] under the supervision of the author. The simulations are based on sinusoidal signals and Gaussian amplifier noise and take into account quantization effects of the analog-to-digital converters. For typical experimental parameters, we observe that a bit resolution of 5 bit is sufficient. The statistical uncertainty of a reconstructed moment scales as $1/\sqrt{N}$, where N is the ensemble size. Furthermore, this uncertainty is proportional to $T_N^{k/2}$, where T_N is the noise temperature of the amplifiers and k is the order of the considered moment. Finally, the resolution limits obtained from experiment and simulation agree very well.

4.3 Dual-path weak signal mixtures

So far, we have studied time-independent ensemble variances because $\langle f(t)^2 \rangle - \langle f(t) \rangle^2 = 0$ always holds for deterministic signals. Time-dependent variance signals require statistical mixtures of signals. As a first example, a sequence of coherent microwave pulses with alternating phase shifts $\pm\varphi$ is applied to the input line. This corresponds to a statistical mixture with an equally distributed histogram. The mean value and cross-variance are $A \cos(\varphi) \sin(\omega t)$ and $-\alpha \cos^2(\omega t)$, respectively, where $\alpha = A^2 \sin^2(\varphi)$ is the cross-variance amplitude and $\omega/2\pi = 10$ MHz is the signal frequency after the mixers. The frequency doubling $\cos^2(\omega t) \propto [1 + \cos(2\omega t)]$ is confirmed in our experiments (cf. Fig. 4.7). In Fig. 4.8(a), we reproduce the expected $\sin^2(\varphi)$ dependence of α for a power level of 2 POA, which is just above the detection limit.

Studying signal mixtures also allows us to address time-dependent third central moments $\langle (S - \langle S \rangle)^3 \rangle$ and $\langle (\chi_1 - \langle \chi_1 \rangle)^3 \rangle$. They are proportional to the skewness of their associated probability histograms and vanish for Gaussian distributions. In particular, both quantities are zero for an equally distributed histogram. Hence, to observe an oscillating third central moment a statistical mixture with an asym-

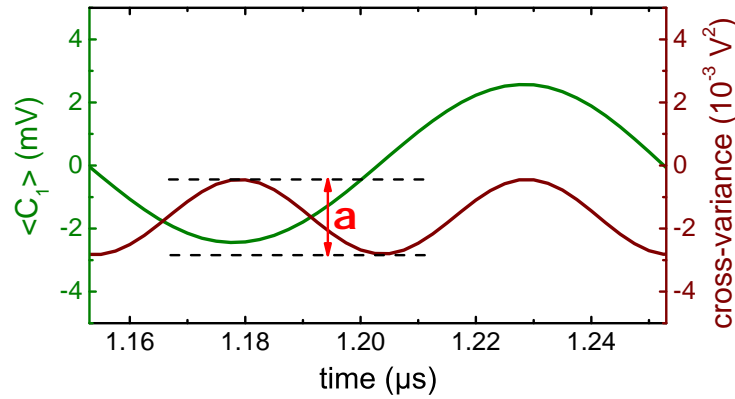


Figure 4.7: Time traces of first moment (green) and cross-variance of an equally distributed statistical mixture of phase-shifted pulses. α denotes the cross-variance amplitude. The power level is equivalent to 100 POA. The gain of the amplification and detection chain is 110 dB.

metric histogram [cf. inset of Fig. 4.8(b)] is required. In the experiment, we again create a train of pulses with 100 POA, but this time 75% of them are shifted by the phase φ and 25% by $-\varphi$. Figure 4.8(b) shows the third central moment calculated from the data of a single amplification chain. In contrast to the case of an equally distributed mixture, a clear oscillating signal is visible within the pulse duration for a skewed histogram. However, there is an offset of approximately $-7 \times 10^{-5} V^3$. In Fig. 4.8(c), one can see that this offset disappears when also taking into account the data from the second chain and applying the dual-path detection scheme described by Eqs. (2.30),(2.31),(2.32) and (2.33). Following these equations, we can write down the third central moment of C_1 as the sum of the third central moments of signal, noise, and ancilla state:

$$\begin{aligned} \langle (C_1 - \langle C_1 \rangle)^3 \rangle &= G^{3/2} \langle (S - \langle S \rangle)^3 \rangle + G^{3/2} \langle (\chi_1 - \langle \chi_1 \rangle)^3 \rangle \\ &\quad + G^{3/2} \langle (V - \langle V \rangle)^3 \rangle. \end{aligned}$$

Since $\langle (V - \langle V \rangle)^3 \rangle = 0$ due to the Gaussian statistics of V , it becomes obvious that the offset in Fig. 4.8(b) must be $G^{3/2} \langle (\chi_1 - \langle \chi_1 \rangle)^3 \rangle$. In this sense, the noise of the detection chain shows non-Gaussian statistics. Although the exact origin of the latter inside the detection chain remains unclear, our experiments provide a first confirmation that the dual-path method is indeed capable of characterizing signal and detector noise moments simultaneously. The detection limit for the third central moment is 10–20 POA in our measurements [cf. Fig. 4.8(d)].

In summary, we have experimentally demonstrated the applicability of the dual-

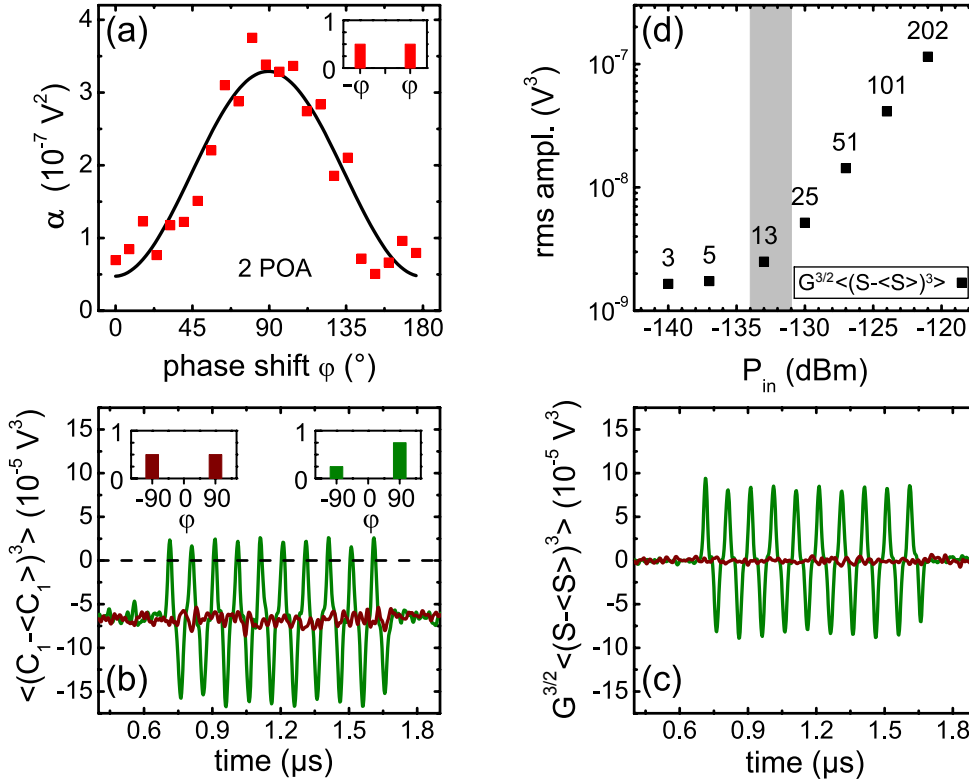


Figure 4.8: Statistical mixtures of phase-shifted pulses. (a) Cross-variance amplitude α plotted versus ϕ at 2 POA. Solid line: fit to the data. Inset: Pulse distribution histogram. (b) Third central moment at 100 POA measured with a single amplification chain. As expected, the trace is $\propto \sin^3(\omega t)$. Insets: Equally distributed (brown) and finite skew (green) histograms. (c) Third central moment measured with the dual-path method, data set as in (c). (d) Power dependence of the third central moment. Gray area: detection limit (10–20 POA). For technical reasons, in (a) and (d) a Wilkinson power divider [58] was used instead of the hybrid ring. Reprinted rearranged figure with permission from Ref. [57]. Copyright (2010) by the American Physical Society.

path method for the moment reconstruction of both the detector noise and statistical mixtures of weak coherent microwaves. Our method is tolerant to the considerable noise added by off-the-shelf phase-insensitive amplifiers for which we observe evidence of a non-Gaussian statistics. The obtained resolution limit of 1–2 POA for the second moment indicates that our dual-path method is a suitable tool for detecting propagating quantum signals such as squeezed states from a JPA, Fock states [14] leaking out of an on-chip resonator [12], or non-classical microwave field states generated in a two-resonator circuit QED setup [83]. Indeed, we successfully reconstruct squeezed states as presented in the next chapter and in Ref. [61].

Chapter 5

Squeezing and path entanglement

In the previous chapter, we have shown the applicability of the dual-path method for the reconstruction of signal moments of weak propagating quantum microwaves and, at the same time, the moments of the amplifier noise. Here, we want to concentrate on non-classical states and entanglement, a purely quantum-mechanical effect. As non-classical state, we use a squeezed state which we generate with a Josephson parametric amplifier (JPA). In Sec. 5.1, we characterize the JPA sample used in our experiments in detail. Next, in Sec. 5.2, we confirm, that the sample can squeeze the vacuum applying a standard homodyning setup. In the following Sec. 5.3, we quantitatively analyze the squeezing utilizing the dual-path cross-correlation technique to reconstruct the Wigner functions of various squeezed vacuum and thermal states and to measure the JPA noise temperature in the degenerate operation mode. In addition, a detailed noise analysis shows that our JPA is operated near the quantum limit in the phase-insensitive mode and that its noise temperature is below the standard quantum limit in the degenerate mode. Finally, in Sec. 5.4, we detect and quantify path entanglement present in the output state of the beam splitter. The results presented in this chapter have been published in Refs. [59, 61].

5.1 JPA characterization measurements

JPAs are promising devices for applications in circuit quantum electrodynamics and for studies on propagating quantum microwaves because of their excellent noise performance. In this section, we present a systematic characterization of a flux-driven JPA at millikelvin temperatures using the spectroscopy setup (cf. Sec. 3.2.3). More specifically, we analyze amplification properties, i.e., signal and idler gain, the associated bandwidths, compression effects, and the noise properties in the non-

degenerate operation mode. A detailed characterization of the JPA is essential to design the filters of the cross-correlation detector correctly (cf. Sec. 3.3). For a discussion of the operation principle of a flux-driven JPA, we refer the reader to Sec. 3.2.1. The sample used in all experiments presented in this chapter, is introduced in Sec. 3.2.2.

5.1.1 Operation point

The first step in characterizing the JPA is to determine a suitable operating point. To this end, we measure the signal gain with a VNA while synchronously sweeping the pump tone, fulfilling the relation $f_{\text{pump}} = 2f_{\text{signal}} + 10 \text{ kHz}$. Since the VNA measurement bandwidth of 30 Hz is much smaller than 10 kHz, only the signal mode is detected. Hence, no interference effects with the idler mode can occur. Furthermore, we emphasize that this measurement is different from the signal bandwidth measurements discussed in Sec. 5.1.3, where the pump tone is at a fixed frequency and only the signal frequency is swept. In Fig. 5.1, we plot the measured signal gain when synchronously sweeping the pump and signal frequency for varying flux values. For lower frequencies, the signal gain increases because the dependence of the resonant frequency on the flux becomes steeper [cf. also Fig. 3.9(b)]. For flux values larger than $-0.62 \Phi_0$, the dependence of the signal gain on the frequency is no longer Lorentzian resulting in an irregularly formed contour. This indicates the presence of large non-linearities and may be related to bifurcation [143]. We

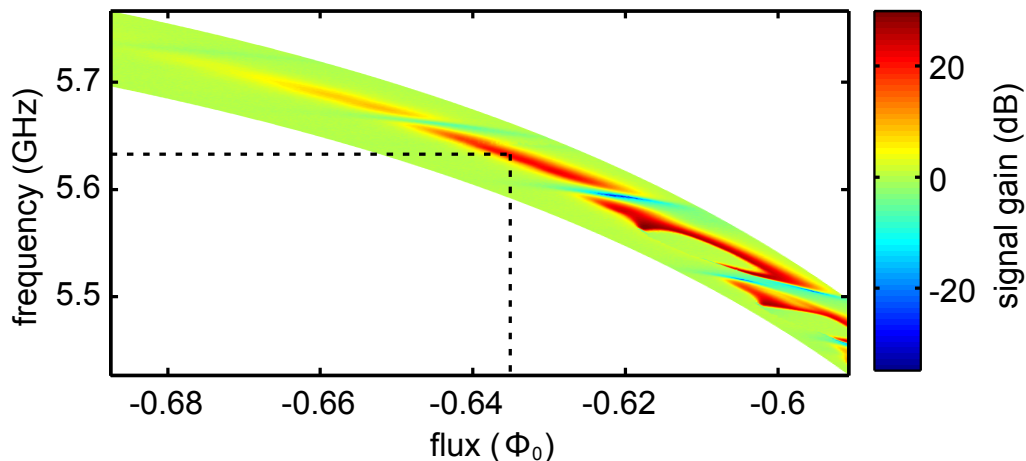


Figure 5.1: Signal gain as a function of frequency and applied magnetic flux at a pump power $P_{\text{pump}} = -39 \text{ dBm}$. The temperature of the JPA is stabilized at 130 mK. The dashed lines indicate the working point for our experiments. Reprinted figure from Ref. [59].

note that previously smooth contours become irregular when increasing the pump power (data not shown). The flux dependence of the signal gain also exhibits regions, where the signal gain attains negative dB-values (blue regions in Fig. 5.1). There the JPA attenuates the signal instead of amplifying it. A possible explanation is the conversion of the signal mode to a different mode (for example higher harmonics). However, the frequency range of the cryogenic microwave components (measurement circulator and HEMTs) do not allow us to investigate these higher order modes. We choose our operating point f_0 inside the interval of 5.634 GHz and 5.639 GHz, depending on the measurement. As it can be seen from Fig. 5.1, our operation point is located in the center of a region where the signal gain is appreciable and its frequency dependence is well behaved. At this operation frequency, the external quality factor is measured as $Q_{\text{ext}} = 312$, and the isolation between antenna and resonator is at least 28 dB.

5.1.2 Non-degenerate gain

When the signal frequency is detuned from half the pump frequency, signal and idler modes are at different frequencies and can be observed individually. This mode of operation is therefore called “non-degenerate mode”. Figure 5.2 shows the pump power dependence of the non-degenerate signal and idler gain for a detuning of 10 kHz. For low pump power, no significant signal gain is observed and the idler

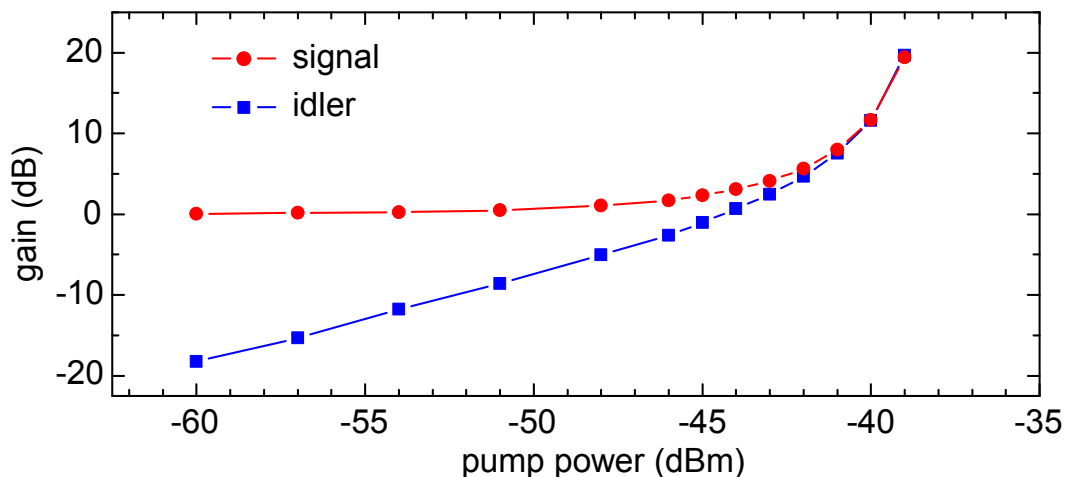


Figure 5.2: Pump power dependence of the idler and signal gain in the non-degenerate operation mode. The solid lines are guides to the eye. The pump and signal frequencies are set to 11.278 GHz and 5.63901 GHz, respectively. The temperature of the JPA is stabilized at 90 mK. Reprinted figure from Ref. [59].

gain is small. For large pump power, the two curves converge and both idler and signal gain reach 19.5 dB.

5.1.3 Bandwidth

Besides the gain properties described above, the bandwidth is an important feature of an amplifier. Therefore, we determine the instantaneous bandwidth of signal and idler modes at a fixed operation point (constant flux and pump frequency) by measuring the signal and idler gain for varying detuning between half the pump frequency $f_{\text{pump}}/2$ and the signal frequency f . As shown in Fig. 5.3, we observe a signal and idler bandwidth of 1.72 MHz for a pump power of -39 dBm. For smaller pump powers, the bandwidth increases, however, the gain is reduced. We define the gain bandwidth product (GBP) as the product of the voltage gain in linear units and the bandwidth of our amplifier. In the large gain limit, the GBP is nearly constant and close to the theoretical limit of $f_0/Q_{\text{ext}} = 18$ MHz [129] [cf. Fig. 5.3(c)]. For low values of the signal gain, the idler gain vanishes and the signal gain approaches one because the signal gain is normalized to the pump-off condition. Therefore, we expect the idler GBP to decrease and signal GBP to increase. However, in the low gain limit the signal bandwidth measurement is very sensitive to the calibration data and fluctuations. Consequently, the signal GBP does not diverge in contrast to expectations from theory.

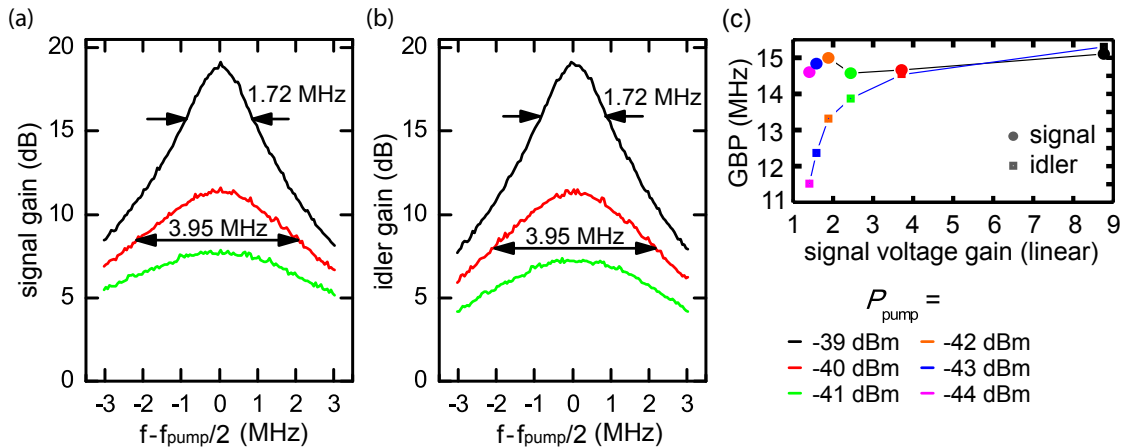


Figure 5.3: Signal (a) and idler (b) gain as a function of frequency, showing the bandwidth for various values of the pump power. (c) GBP as a function of the signal voltage gain in linear units. The dashed lines are guides to the eye. The temperature of the JPA is stabilized at 90 mK. Reprinted figure from Ref. [59].

5.1.4 1 dB-compression point

Another important figure of merit for amplifiers is their 1 dB-compression point. It denotes the power where the signal gain is 1 dB below the value expected for a perfectly linear device [119]. In other words, at some point the signal gain starts to decrease as a function of input power due to the non-linearity of the amplifier. In Fig. 5.4(a) bandwidth measurements of the signal gain are displayed. In contrast to Fig. 5.3, here the pump power is fixed at -39 dBm and the dependence on the signal power is studied. For small signal powers ($P_{\text{signal}} \leq -136$ dBm) the curves overlap meaning that the gain is constant and that the amplifier is in the linear regime. For larger signal powers a reduction of the gain is observed. Figure 5.4(b) shows the signal gain of Fig. 5.4(a) in the limit $f \rightarrow f_{\text{pump}}/2$ for several signal powers. The 1 dB-compression point can be observed at -133 dBm. An analogous analysis for the idler gain (data not shown) reveals that the compression occurs for both the idler and signal gain at the same input power. For a circuit QED experiment with a cavity decay rate of 1 MHz, this power level is equivalent to 10 photons on average.

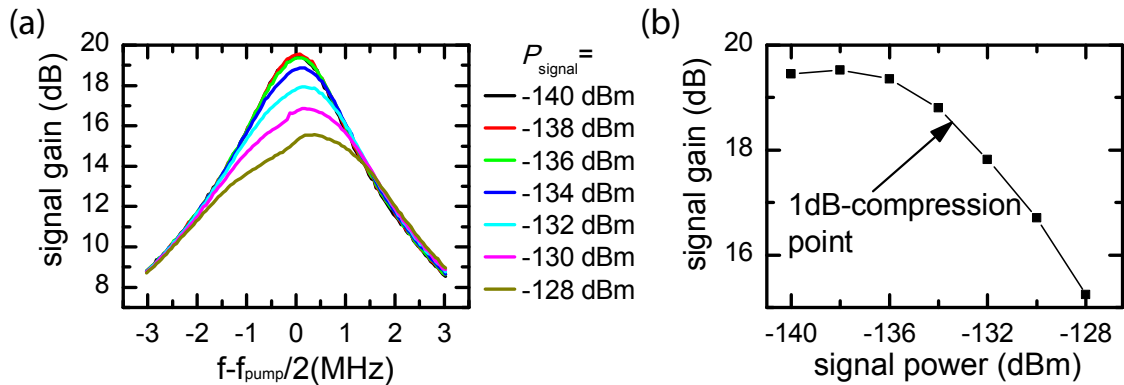


Figure 5.4: (a) Signal gain as a function of frequency for various values of the signal power and (b) signal gain at $f \rightarrow f_{\text{pump}}/2$ versus signal power. Squares: data. Line: guide to the eye. The temperature of the JPA is stabilized at 88 mK. Reprinted figure from Ref. [59].

5.1.5 JPA noise properties in non-degenerate mode

A low noise temperature of an amplifier is very important when using it for measuring signals at the quantum level. Here, we use the spectroscopy setup for a rough characterization of the noise properties of our JPA when it is operated in the phase-insensitive mode. For details on the noise temperature in the degenerate mode, we refer to Sec. 5.3.3. In order to determine the JPA noise properties, we measure the

amplified noise power emitted by the 30 dB-attenuator, whose temperature is controlled in the range $T_{\text{att}} = 50 - 800$ mK. The total noise power P at the spectrum analyzer is given by

$$P(T_{\text{att}}) = GB \left[\frac{hf_0}{2} \coth \left(\frac{hf_0}{2k_B(T_{\text{att}} + \delta T)} \right) + k_B T_{\text{total}} \right], \quad (5.1)$$

where G denotes the total gain, B the detection bandwidth, h the Planck constant, k_B the Boltzmann constant and T_{total} the total noise temperature of the complete detection chain, which includes the measurement circulator, the JPA and the amplification chain. T_{total} is related to the number of photons n_{total} added by the complete detection chain by $k_B T_{\text{total}} = n_{\text{total}} h f_0$. The first term in Eq. (5.1) describes thermal fluctuations and vacuum fluctuations according to Ref. [144]. Possible deviations between the electronic temperature of the attenuator and the measured temperature are taken into account by δT . We set the signal gain to $G_{\text{signal}}(T \rightarrow 0) = 19$ dB at the operation point f_0 . However, sample heating due to the pumping process and compression effects at high noise source temperatures may cause the signal gain to deviate from this value. Therefore, we measure the dependence of the gain-corrected power on the noise source temperature T_{att} (cf. Fig. 5.5). To this end,

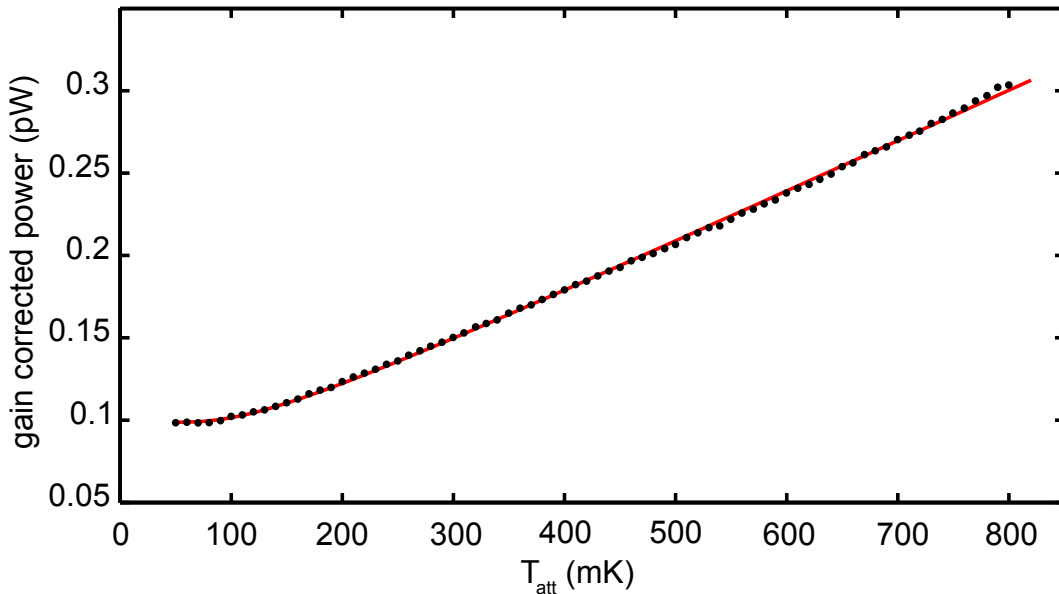


Figure 5.5: Gain-corrected power as a function of the noise source temperature. Red line: Fit to the data using Eq. (5.1). The JPA operation frequency f_0 is 5.6372 GHz. The JPA temperature is in the range from 92 to 115 mK. Reprinted figure from Ref. [59].

we implement the following protocol for each temperature point: after measuring the signal gain with the VNA, we turn off the VNA and measure the total noise power using a spectrum analyzer. We obtain the gain-corrected power by dividing the total noise power at each temperature point by the effective JPA gain for white uncorrelated noise, $G_{\text{eff}}(T) = 2G_{\text{signal}}(T) - 1$. Here, we consider the idler gain using $G_{\text{idler}} = G_{\text{signal}} - 1$ from Ref. [112]. Taking into account the cable and connector losses between the noise source and the measurement circulator, we estimate $T_{\text{total}} = 167$ mK, which corresponds to $n_{\text{total}} = 0.62$ for the noise photons added by the whole detection chain referred to the input of the measurement circulator. This value is close to the standard quantum limit for phase-insensitive amplifiers of 0.5 photons (135 mK). In addition, we find $\delta T = -19$ mK to be reasonably small.

5.1.6 Degenerate gain

In order to demonstrate the usability of our JPA as a phase-dependent amplifier, we investigate the degenerate gain. In this mode of operation, the pump frequency is twice the signal frequency. Thus, the idler mode is created at the frequency of the amplified signal mode. This results in an interference of the two modes that is constructive or destructive depending on the phase between the idler and the signal modes, which can be controlled by shifting the phase difference between the probe signal and the pump tone. The degenerate gain is measured with a spectrum analyzer, where a measurement with zero pump power is used as a reference.

In Fig. 5.6, the degenerate gain is plotted as a function of the phase between the probe signal and the pump for various pump power levels. We observe a maximum degenerate gain of 25.5 dB and a maximum deamplification of 22.3 dB. The former value is consistent with the signal and idler gain of 19.5 dB (cf. Sec. 5.1.2), since the constructive interference of equal amplitudes results in a 6 dB increase of gain.

In summary, at an operating frequency close to 5.637 GHz, we find a total noise temperature of 167 mK (non-degenerate operation mode), a signal and idler gain of 19.5 dB, a bandwidth of 1.72 MHz, and a maximum degenerate gain of 25.5 dB.

5.2 Homodyne detection of squeezed vacuum

As mentioned in the discussion of the operation principle (cf. Sec. 3.2.1), the JPA creates quantum correlations between the signal and the idler mode. In the degenerate operation mode, these correlations result in deamplification or amplification

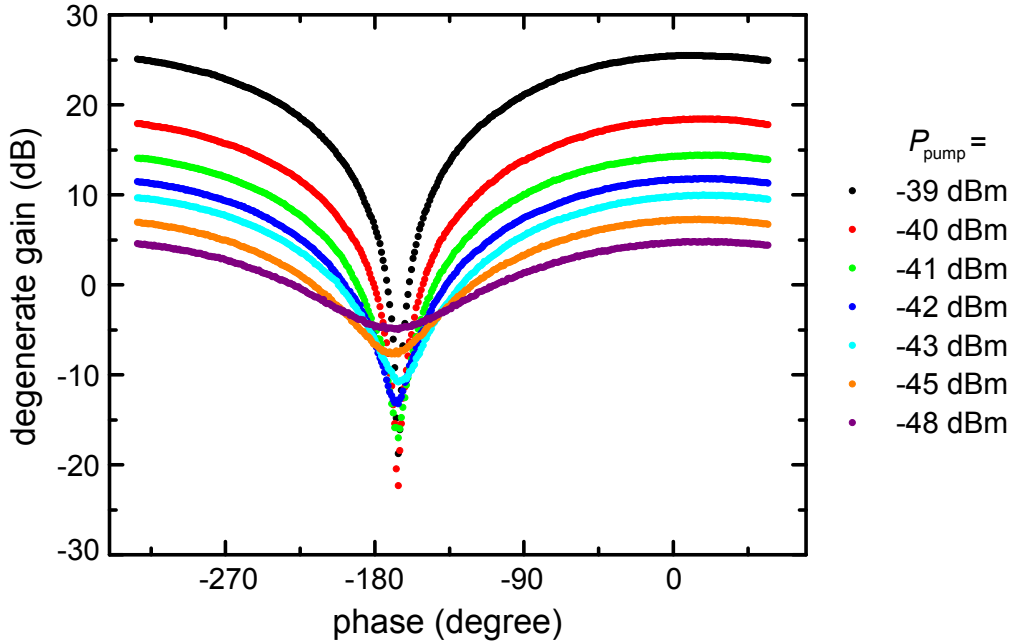


Figure 5.6: Degenerate gain as a function of the phase difference between probe and pump signal for various values of the pump power. For clarity, the curves are shifted in phase direction, so that the minima coincide. The temperature of the JPA is stabilized at 95 mK. Reprinted figure from Ref. [59].

depending on the quadrature direction. In the case of deamplification, the quadrature fluctuations can be squeezed below those of the vacuum. In this section, we investigate squeezed vacuum fluctuations generated by the flux-driven JPA with the homodyne detection setup (cf. Sec. 3.2.3). The dual-path state reconstruction [57,61] of squeezed states is considered in the next section, Sec. 5.3.

To define the squeezing level \mathcal{S} in decibel, we compare the variance of the squeezed quadrature $(\Delta X_{\text{sq}})^2$ with the quadrature variance of vacuum fluctuations, obtaining

$$\mathcal{S} = \max\{0, -10 \lg [(\Delta X_{\text{sq}})^2 / 0.25]\}. \quad (5.2)$$

We note that $(\Delta X_{\text{sq}})^2 < 0.25$ indicates squeezing and \mathcal{S} is positive. Larger \mathcal{S} corresponds to a higher squeezing level. $(\Delta X_{\text{sq}})^2 \geq 0.25$ indicates no squeezing and, in this situation, \mathcal{S} equals zero. Hence, in this work we use the nomenclature that the term “squeezing” is equivalent to “squeezing below the vacuum level”.

We detect the output signal of the JPA with the homodyne detector shown in Fig. 3.11(b). By sweeping the temperature of the 30 dB-attenuator from 50 mK to 800 mK with inactive JPA, we calibrate the gain and the noise temperature of the detection chain using Eq. (5.1). Then, we cool the attenuator to 33 mK and investi-

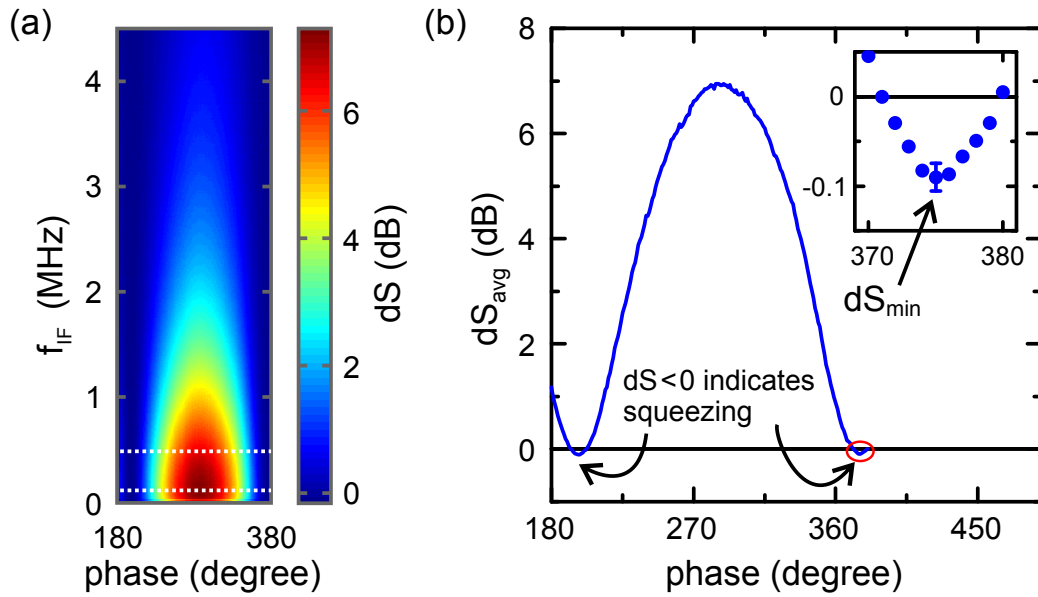


Figure 5.7: Squeezing of vacuum fluctuations detected with the homodyne setup. (a) Power spectral density ratio dS plotted as a function of phase and intermediate frequency. (b) The power spectral density ratio averaged over the frequency range from 118 to 487 kHz, dS_{avg} , plotted as a function of phase. The averaged region is indicated by the dotted lines in panel (a). The inset shows a zoom-in of the region marked by the red ellipse. The JPA temperature is stabilized at 88 mK. Reprinted figure from Ref. [59].

gate the squeezed vacuum state. To this end, we record the power spectral densities S_{on} and S_{off} with the JPA pump power on and off, respectively. In Fig. 5.7(a), the ratio $dS \equiv S_{\text{on}}/S_{\text{off}}$ is plotted as a function of the relative phase between the pump and the local oscillator and the detected intermediate frequency f_{IF} . The latter is obtained by downconverting the signal using a fixed local oscillator frequency $f_{\text{LO}} = f_0 = f_{\text{pump}}/2$. For these settings, signals at $f_{\text{LO}} + f_{\text{IF}}$ and $f_{\text{LO}} - f_{\text{IF}}$, representing the signal and idler modes, are downconverted to the same intermediate frequency f_{IF} . Therefore, the homodyne detector is sensitive to the correlations between the two modes created by the JPA. In Fig. 5.7(b), the average dS_{avg} of dS calculated in the frequency range $118 \text{ kHz} < f_{\text{IF}} < 487 \text{ kHz}$ is plotted. Whenever $dS_{\text{avg}} < 0 \text{ dB}$, the noise detected at the spectrum analyzer referred to the input of the amplification chain is smaller than the vacuum noise emitted by the attenuator. This demonstrates the effect of vacuum squeezing. From the minimal value dS_{min} indicated in the inset of Fig. 5.7(b), we calculate the squeezing level [25]

$$\mathcal{S} = -10 \lg \left[1 - \frac{T_n (1 - 10^{dS_{\text{min}}/10})}{0.5h f_0 / k_B} \right]. \quad (5.3)$$

Here, T_n is the noise temperature of the detection chain with the JPA off. Taking into account the cable losses, reference spectrum fluctuation and thermal population at the input of the JPA, we retrieve a lower bound of 2.8 dB of squeezing at the input of the amplification chain.

5.3 Dual-path state reconstruction

The estimation of the squeezing level with the homodyne detection setup only yields a lower bound for the amount of squeezing. Rather than improving this setup, we choose to fully reconstruct the squeezed state emitted by the JPA with the dual-path setup, which is based on cross-correlation techniques and realtime data processing [57, 61]. For an introduction of the dual-path theory and a detailed description of the dual-path setup, we refer the reader to Sec. 2.6 and Sec. 3.3, respectively. For the sake of a convenient discussion on the relevant physics, we display a simplified sketch of the experimental setup in Fig. 5.8. We measure all moments of the signal mode and of the noise contributions in the two detection paths up to fourth order. The calibration of the photon number conversion factors, which relate the auto-correlations measured in our detector (in units of V^2) to photon numbers at the input of the beam splitter, is presented in Sec. 3.3.4.

Following Sec. 2.12, we calculate the third and fourth order cumulants from the third and fourth signal moments to verify the Gaussianity of the state. Whenever

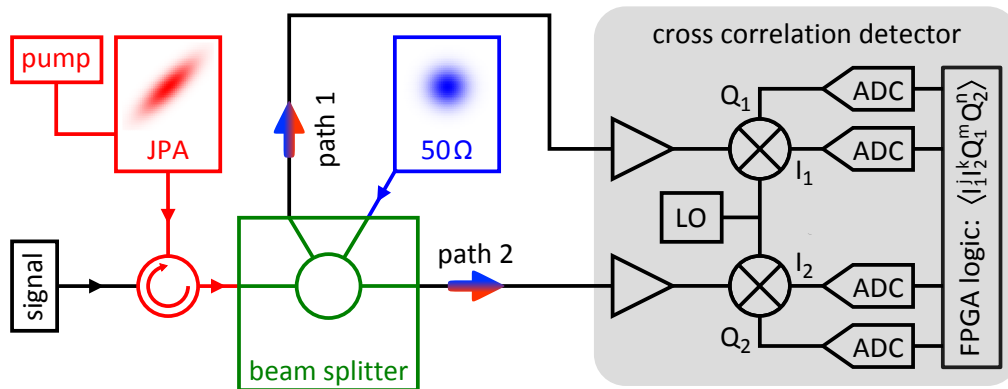


Figure 5.8: Layout of the experiment. The signal can be a thermal state or a (displaced) vacuum and becomes squeezed by the JPA when the pump is on. The signal is split into two paths by a 180° -hybrid ring microwave beam splitter (green). The blue-and-red arrows denote the output state, which is measured by the cross-correlation detector. Reprinted figure with permission from Ref. [61]. Copyright (2012) by the American Physical Society.

this verification is positive, we use the first two moments to reconstruct the signal Wigner functions at the input of the beam splitter (cf. Sec. 2.7). In all dual-path experiments, the temperature of the JPA sample box is stabilized at 50 mK resulting in a $50\ \Omega$ -termination temperature of 40 mK.

5.3.1 Reconstruction of coherent states

As a first test of our setup, we perform dual-path reconstructions of the Wigner function for known input states. Here, we exploit the fact that the noise contributions of the two amplification paths are independent, while the split signals are correlated (cf. also Sec. 2.6 and Ref. [57]). We reconstruct vacuum fluctuations and coherent states (displaced vacuum), both at a frequency $f_0 = 5.637$ GHz. The JPA pump is off in these measurements. Because of the narrow measurement bandwidth of 978 kHz, we approximate the vacuum and thermal states as single-mode fields. The results shown in Fig. 5.9 exhibit a very good phase control for the coherent state. In addition, we find a small thermal contribution of 0.097 ± 0.007 photons above the vacuum level which can be due to a small thermal population or other experimental imperfections. At the same time, the noise moments of the two detection paths are

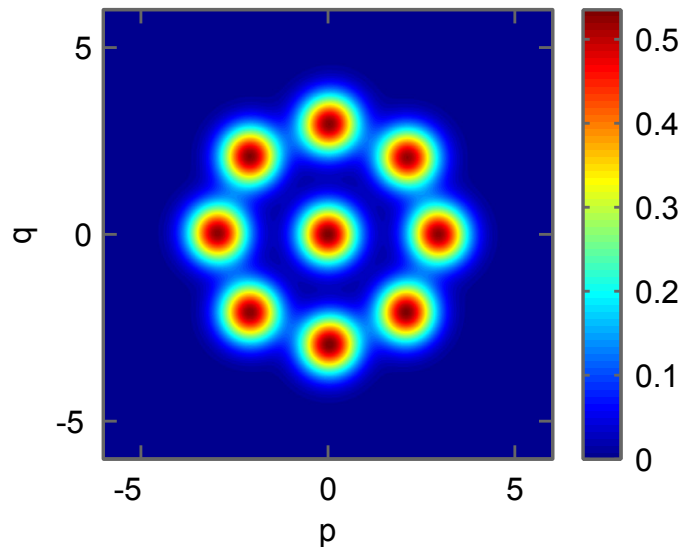


Figure 5.9: Dual-path reconstruction of the vacuum and of coherent states incident at the beam splitter. The photon number is 8.80 ± 0.01 photons and the phase varies from 0° to 315° in steps of 45° . All nine Wigner functions are superposed. p and q are dimensionless variables spanning the phase space. Reprinted figure with permission from Ref. [61]. Copyright (2012) by the American Physical Society.

obtained. We find that the detection chains add 24.82 ± 0.03 and 26.87 ± 0.03 photons referred to the beam splitter input which corresponds to noise temperatures of 6.71 ± 0.01 K and 7.27 ± 0.01 K for the detection path 1 and 2, respectively. The error bars we provide are of purely statistical nature.

In Fig. 5.10, we show the photon number $n \equiv \langle \hat{a}^\dagger \hat{a} \rangle$ and amplitude $\alpha \equiv \langle \hat{a} \rangle$ extracted from the reconstructed moments against power P_{gen} at the output of the signal generator. Here, \hat{a}^\dagger and \hat{a} are the field operators of the input state as defined in Sec. 2.6. The expected linear and square root dependences, $n(P_{\text{gen}}) = AP_{\text{gen}}$ and $\alpha(P_{\text{gen}}) = B\sqrt{P_{\text{gen}}}$, are clearly reproduced. Within an error bar of less than two percent, B is the square root of A for independent fits.

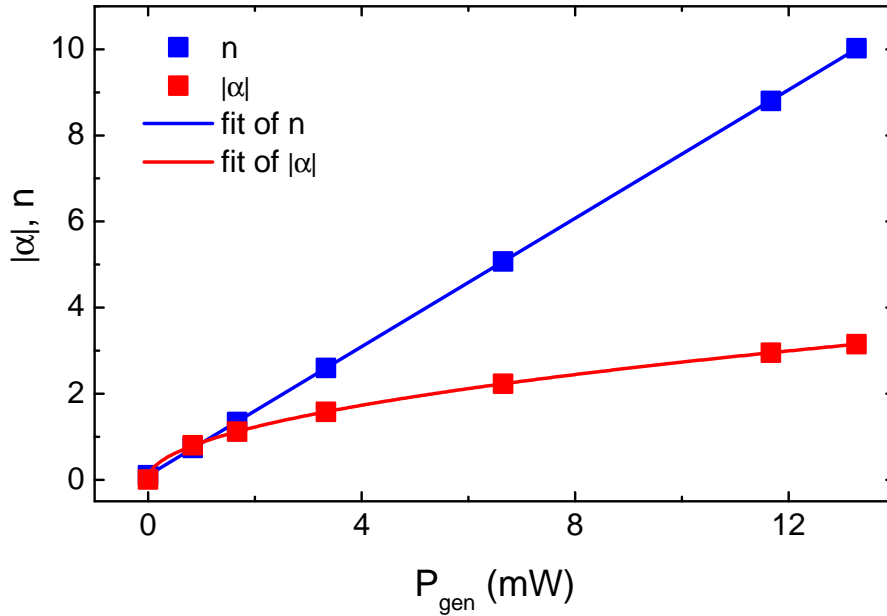


Figure 5.10: Coherent state reconstruction. Photon number n and amplitude $|\alpha|$ as a function of the signal generator power P_{gen} .

5.3.2 Reconstruction of squeezed vacuum and squeezed thermal states

Having verified that our detector is well calibrated, we reconstruct squeezed vacuum and squeezed thermal states incident at the input of the beam splitter. To this end, we generate squeezed states by pumping the JPA at $2f_0 = 11.274$ GHz. Figure 5.11 shows typical time traces for selected second moments of a squeezed vacuum state averaged over 5×10^5 traces. Since the phase angle in this example is chosen to be 0° , $\langle Q_1^2 \rangle$ increases significantly above the vacuum level and $\langle I_1^2 \rangle$ decreases below

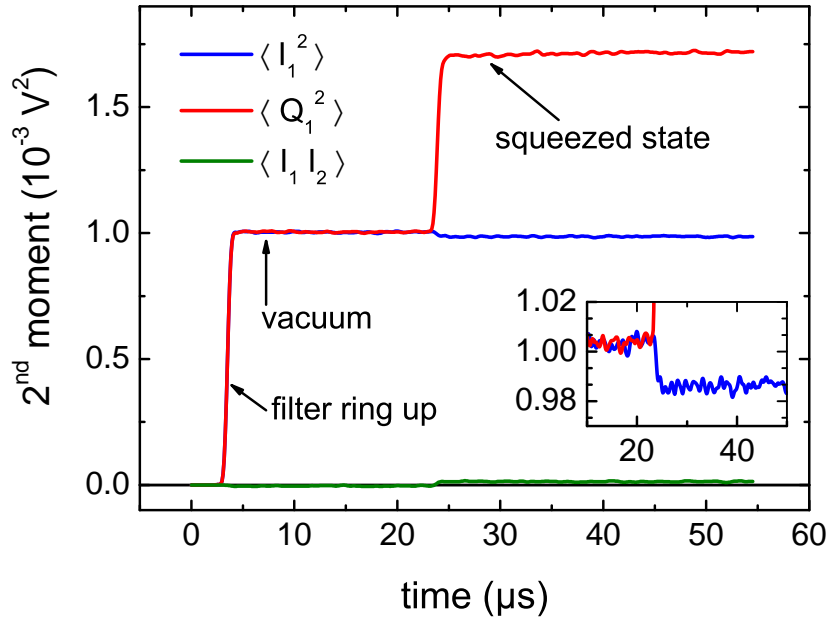


Figure 5.11: Typical averaged time traces of selected second moments from a squeezed state measurement with 0° phase and for 10 dB signal gain. Each averaged trace consists of 5×10^5 single traces. The rise time of 650 ns is determined by the digital filters. The step between JPA pump off (vacuum) and on (squeezed state) is shifted by $4 \mu\text{s}$ with respect to the pulse shown in Fig. 3.16 because of a delay due to filtering.

the vacuum level as expected. The cross-moment $\langle I_1 I_2 \rangle$ shows the characteristic cancellation of the uncorrelated noise contributions of the amplification paths, which lies at the heart of the dual-path tomography. A Wigner function reconstruction based on this dataset is shown in Fig. 5.13(b).

Furthermore, we demonstrate the capability of the dual-path state reconstruction method to retrieve clean signal moments. Figure 5.12(a) displays the Wigner functions based on the measured complex envelope moments of a single path for a squeezed vacuum state. The elliptic shape suggests squeezing, however, the blue contour line in Fig. 5.12(c) reveals that the noise of the HEMT amplifiers dominates the detected signal. Thus, one cannot evaluate if the state is squeezed below the vacuum without making use of a signal recovery method. The situation changes completely, when we apply the dual-path state reconstruction method to the data. The resulting Wigner function, shown in Fig. 5.12(b), is much thinner in the squeezed direction than the one based on the uncorrected complex envelope moments of a single path. An analysis of the reconstructed signal moments reveals that, at the input of the beam splitter, the state generated by the JPA is squeezed by 4.9 ± 0.2 dB below the vacuum level and contains 8.72 ± 0.05 photons. Furthermore, the product

of the standard deviation of the squeezed quadrature with that of its orthogonal, enlarged one, is 3.45 ± 0.07 times larger than the variance of the ideal vacuum. In other words, we can model the state as one created by an ideal squeezer acting on an effective thermal field with 1.22 ± 0.04 photons. This thermal field contains the combined effects of losses and the small thermal population found in the experimental vacuum. It is noteworthy to mention that the amount of squeezing quoted above is mainly limited by cable losses and not by the JPA itself.

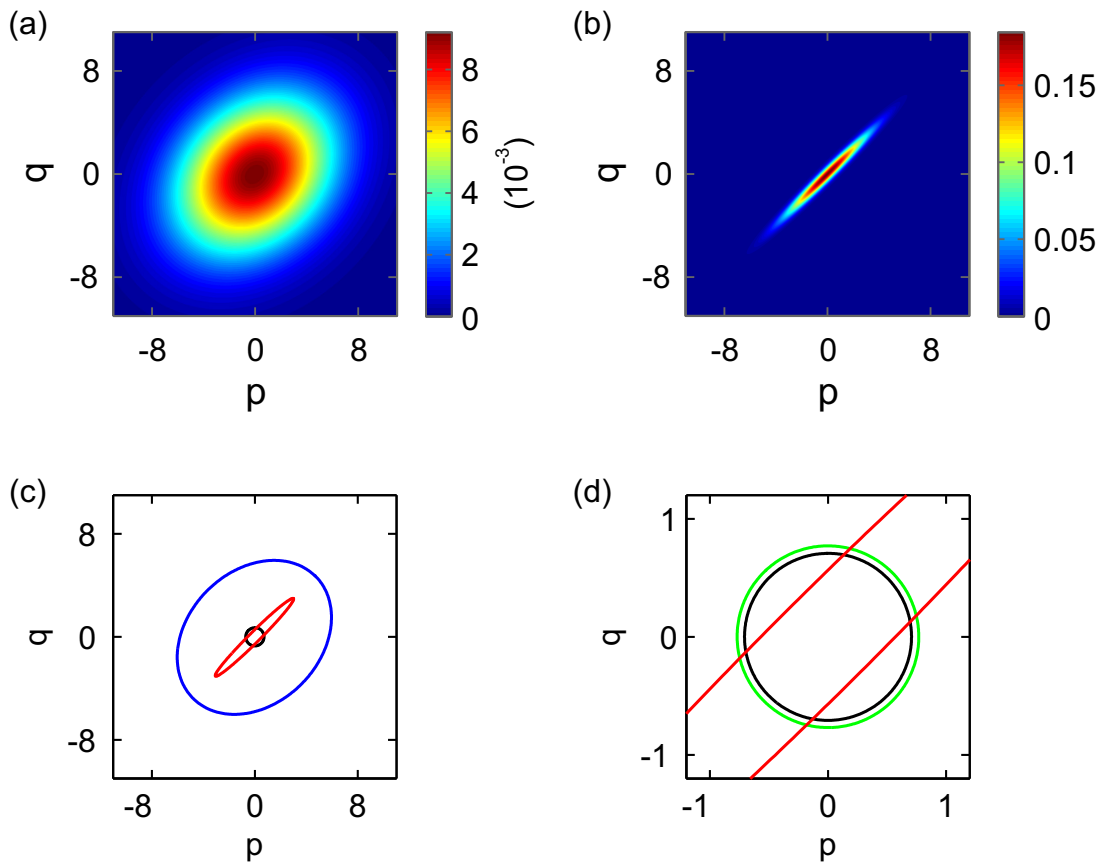


Figure 5.12: Reconstruction of a squeezed vacuum state at the input of the beam splitter for a JPA signal gain of 10 dB and a phase of 45° . (a) Color map plot of the Wigner function based on the uncorrected measured complex envelope moments of path 1. (b) Color map plot of the Wigner function using the signal moments reconstructed with the dual-path method. (c) $1/e$ -contours of the Wigner functions displayed in panels (a) and (b). The blue curve is calculated from the uncorrected complex envelope moments. The red line is based on the dual-path reconstructed signal moments. Black line: ideal vacuum. (d) Zoom-in on the central region of panel (c). Black line: ideal vacuum. Green line: experimental vacuum. Red line: squeezed vacuum.

Again, we notice good control of the phase. The phase stability between signal/pump and local oscillator is better than $\pm 0.3^\circ$ for 5×10^5 traces. Hence, reconstructions based on such a number of averages exhibit very good phase control as shown in Fig. 5.13.

Next, we investigate the squeezing and its dependence on the signal gain and on thermal fluctuations in more detail. Selected Wigner function reconstructions are plotted in Fig. 5.14. When the 30 dB-attenuator is stabilized at 50 mK, vacuum fluctuations are present at the input of the JPA. As shown in Fig. 5.14(a), the increase in pump power, which corresponds to an increase of signal gain, causes an increase of the squeezing level and an increase of the photon number [cf. also Fig. 5.15(a)]. We achieve a maximum squeezing level of 4.9 ± 0.2 dB below vacuum at 10 dB signal gain.

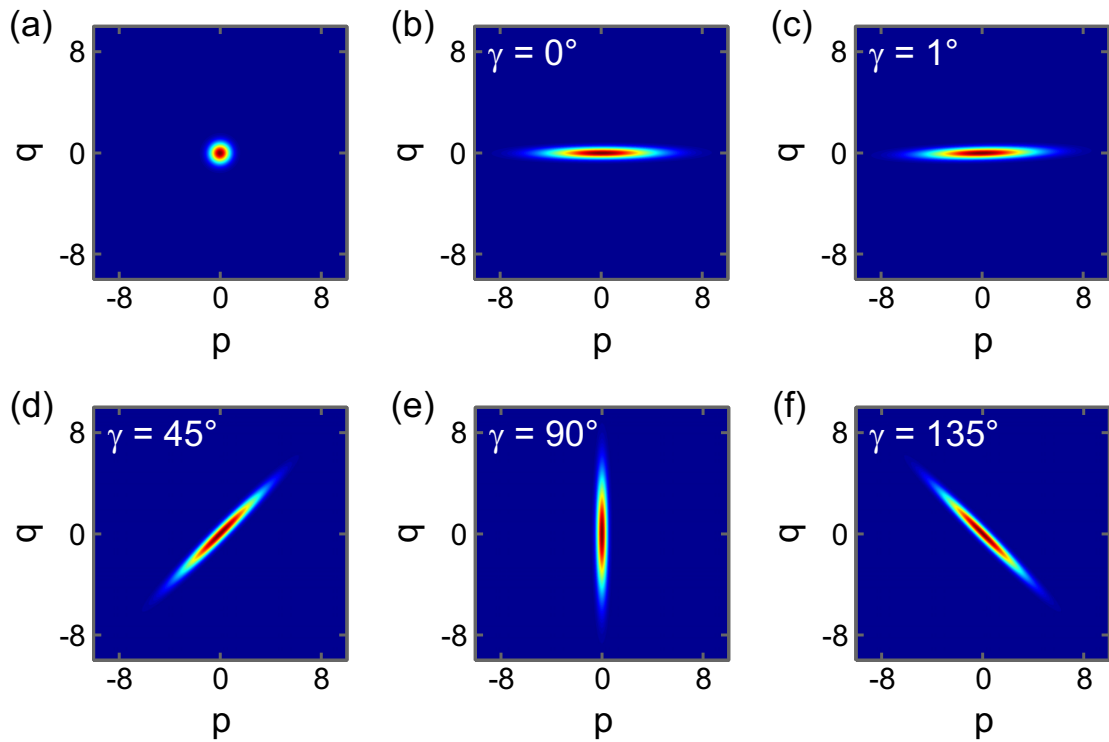


Figure 5.13: Phase control for squeezed state reconstruction. Wigner functions of (a) the vacuum, (b) a squeezed state at 0° , (c) a squeezed state at 1° , (d) a squeezed state at 45° , (e) a squeezed state at 90° , and (f) a squeezed state at 135° . The angle between the anti-squeezed quadrature and the p -axis is denoted as γ . The number of averaged traces is 5×10^5 . The residual thermal population of the vacuum is 0.102 ± 0.005 photons. For the squeezed state, the JPA signal gain is 10 dB and the reconstructed photon number $n = 8.67$ varies by approximately 0.5% for the different phase angles.

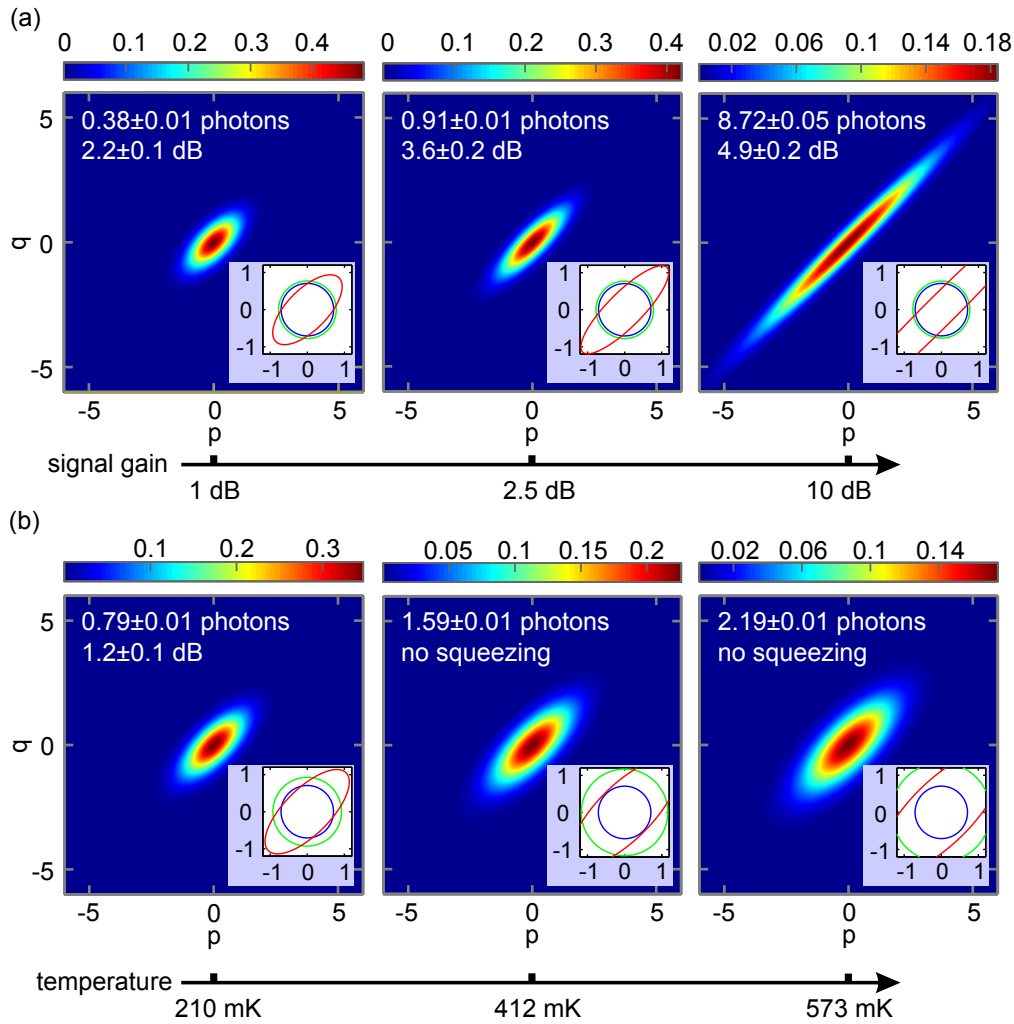


Figure 5.14: Reconstructed Wigner functions (color map) of squeezed vacuum and squeezed thermal states incident at the input port of the microwave beam splitter. p and q are dimensionless quadrature variables spanning the phase space. The insets show the $1/e$ -contours of the ideal vacuum (blue), the experimental vacuum or thermal states (green), and the squeezed vacuum or squeezed thermal states (red). (a) Constant 30 dB-attenuator temperature of 50 mK. (b) Constant signal gain of 1 dB. Reprinted figure from Ref. [59].

However, if we further increase the signal gain, the squeezing level decreases again. This behavior is expected [66] because the squeezing becomes suppressed when the JPA enters the bifurcation regime. In this regime, also the higher order cumulants are no longer expected to vanish. Indeed, we observe this effect in our data for signal gains larger than 10 dB. In addition, from the JPA input-output relation [64] we identify the signal voltage gain in the non-degenerate mode in linear units as $G_{\text{signal},V} = \cosh(r)$. Applying this relation, we obtain from the photon

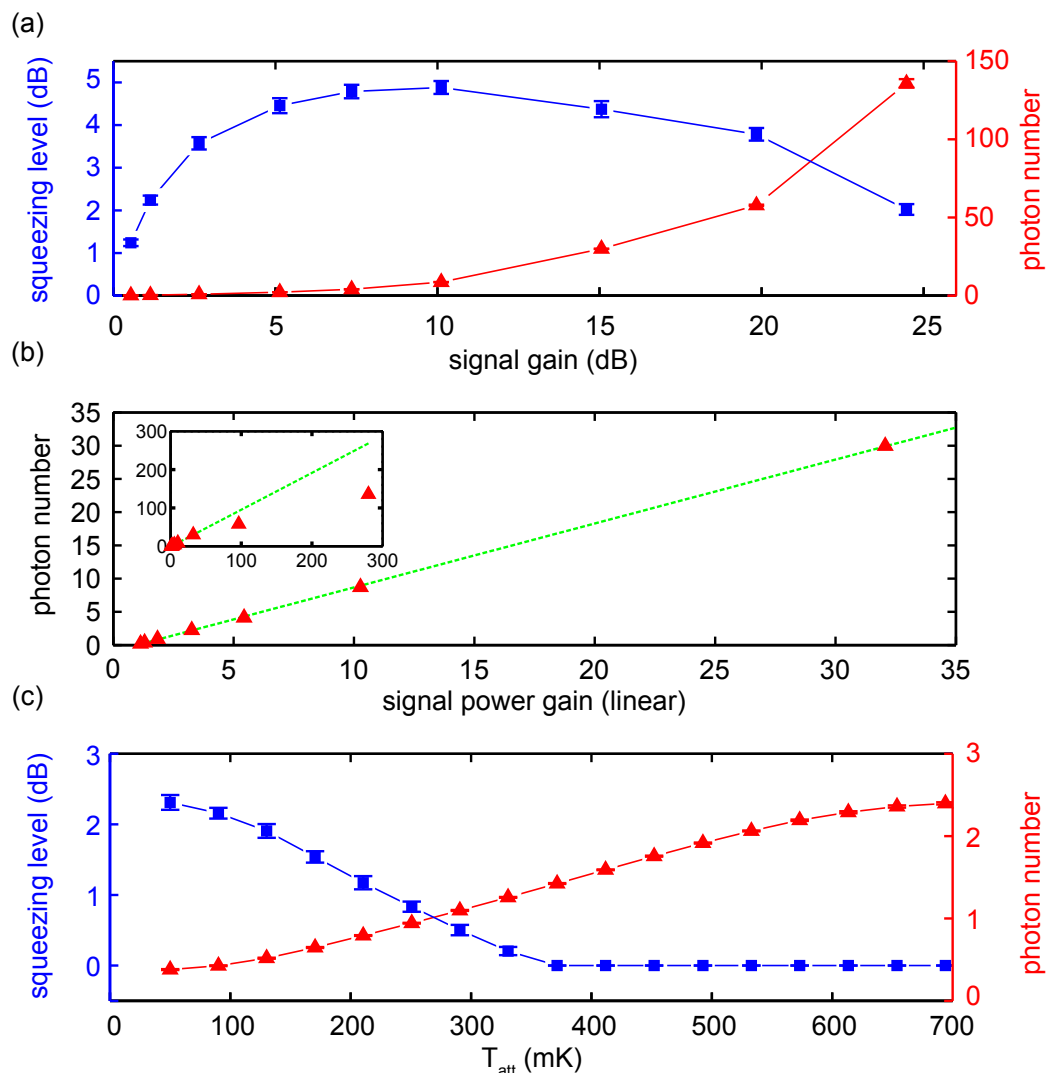


Figure 5.15: (a) Squeezing level (blue squares) and photon number (red triangles) plotted as a function of the signal gain when the 30 dB-attenuator is at 50 mK. The lines are guides to the eye. (b) Photon number as a function of signal power gain in linear units. Red triangles: data. Green dashed line: linear fit. Inset: Signal gain range equivalent to that shown in panel (a). The two data points with the largest signal gain are excluded from the fit. (c) Squeezing level (blue squares) and photon number (red triangles) plotted as a function of the 30 dB-attenuator temperature for 1 dB signal gain. The lines are guides to the eye. All error bars are of statistical nature. Reprinted figure from Ref. [59].

number of a squeezed state, $n = \sinh^2(r)$, the expression $n = G_{\text{signal,P}} - 1$, where $G_{\text{signal,P}} = G_{\text{signal,V}}^2$ is the signal power gain in linear units. Therefore, we expect that the photon number increases linearly with $G_{\text{signal,p}}$ in the non-degenerate mode with a slope of one. Figure 5.15(b) confirms this behavior for small signal gains below the bifurcation regime. Next, we fix the signal gain at 1 dB. When the temperature of the 30 dB-attenuator is increased [cf. Fig. 5.14(b) and Fig. 5.15(c)], more and more thermal photons are incident at the input port of the JPA. Thus, the squeezing level decreases and at some point the output state of the JPA is not squeezed below vacuum any more.

5.3.3 JPA noise properties in degenerate mode

A JPA operated in the degenerate mode can not only generate vacuum squeezing, it can also be used as a low-noise phase-sensitive amplifier which, in principle, does not need to add any noise to the amplified quadrature [81]. With the dual-path setup, we therefore study the noise properties of our JPA in the degenerate mode. More precisely, we perform a temperature sweep of the 30 dB-attenuator at the input of the JPA (see also Fig. 3.14 in Sec. 3.3.1). The variance of the fluctuations at the frequency f_0 generated with this procedure is

$$(\Delta X_{\text{therm}})^2 = \frac{1}{4} \coth\left(\frac{hf_0}{2k_B T_{\text{att}}}\right) \quad (5.4)$$

where $(\Delta X_{\text{therm}})^2$ has the unit of photon number. At each temperature, the JPA pump is operated in the pulsed mode. Consequently, a single time trace in our measurement always contains a region corresponding to a non-squeezed thermal state and a region corresponding to a squeezed thermal state. For any quadrature, the variance $(\Delta X_{\text{out}})^2$ at the output of the JPA is related to the variance $(\Delta X_{\text{in}})^2$ at the input via the relation [81]

$$(\Delta X_{\text{out}})^2 = G_X (\Delta X_{\text{in}})^2 + (\Delta X_{\text{noise}})^2. \quad (5.5)$$

Here, G_X is the gain for this quadrature and $(\Delta X_{\text{noise}})^2$ is the noise added by the amplifier referred to the output. In principle, we could determine the variance of the thermal state at the input of the JPA using the dual-path reconstructed signal moments at the input of the beam splitter taking into account the cable, circulator and JPA losses. However, the dual-path reconstruction detects a thermal population of 0.1 photons in the vacuum which would result in a significant underestimation of

the JPA noise. For this reason, we calculate $(\Delta X_{\text{in}})^2$ based on Eq. (5.4), and model the cable loss between the 30 dB-attenuator output and the measurement circulator input with beam splitters, and account for the temperature gradients. In this way, we model an equivalent amplifier consisting of the measurement circulator, JPA, and cables to the beam splitter input. The noise contributions of all these components are represented by the noise temperature of the equivalent amplifier. Therefore, the latter is a pessimistic estimate for the noise properties of the JPA itself.

In Fig. 5.16, we show the anti-squeezed and squeezed quadrature variance as a function of the noise source temperature. We find good agreement between theory and experiment. The corresponding numerical results are displayed in Tab. 5.1. Most importantly, we observe a variance of 0.14 ± 0.01 photons (referred to the input) for the noise added by our JPA to the anti-squeezed quadrature. This value is clearly below the standard quantum limit of 0.25 photons for a single quadrature of a phase-insensitive amplifier. The relevant noise number for the use of the JPA as a squeezer is the noise it adds to the squeezed quadrature at the JPA output. We do not refer the added noise from the squeezed quadrature to the input of the equivalent JPA, because systematic uncertainties in the setup [61] dominate the squeezed quadrature noise variance at the JPA output and would be amplified by $1/G_{\text{sq}}$ when referring to the JPA input. However, these uncertainties are negligible for the anti-squeezed

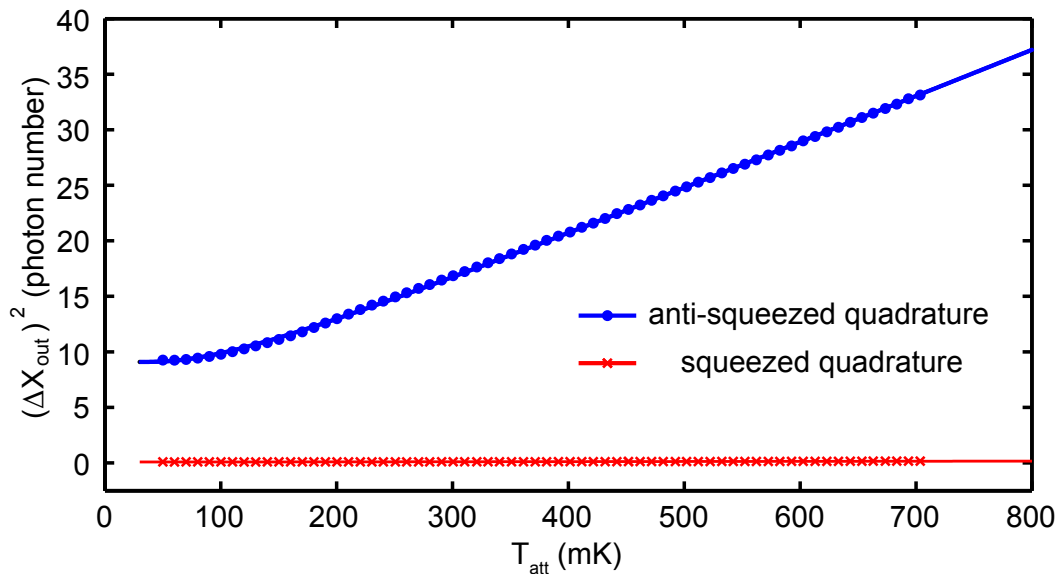


Figure 5.16: Anti-squeezed and squeezed quadrature variance as a function of the noise source temperature T_{att} . Lines: Fits of Eq. (5.5) to the data (symbols). The fit results are summarized in Tab. 5.1. For each temperature point, 2×10^6 traces are measured. Reprinted figure from Ref. [59].

| X | G_X (dB) | $(\Delta X_{\text{noise}})^2$ | $(\Delta X_{\text{noise}})^2 / G_X$ |
|------|-----------------|-------------------------------|-------------------------------------|
| sq | -11.7 ± 0.3 | 0.06 ± 0.01 | – |
| anti | 13.7 ± 0.1 | – | 0.14 ± 0.01 |

Table 5.1: Dual-path analysis results for JPA gain and noise along squeezed and anti-squeezed quadratures. The error bars describe the statistical error obtained from the fitting procedure. $(\Delta X_{\text{noise}})^2$ has the unit of photon number.

quadrature. Instead, following [81] we calculate a lower bound for the squeezed quadrature noise variance at the JPA input from the experimentally more robust quadrature gains G_{sq} and G_{anti} of the squeezed and anti-squeezed quadrature noise variance. Using the values from Tab. 5.1, we obtain the relation

$$(\Delta X_{\text{noise,sq}})^2 / G_{\text{sq}} \geq \frac{1}{16} \left| 1 - (G_{\text{sq}} G_{\text{anti}})^{-1/2} \right|^2 / [(\Delta X_{\text{noise,anti}})^2 / G_{\text{anti}}] = 0.02. \quad (5.6)$$

Thus, the JPA adds at least 0.02 noise photons referred to its input to the squeezed quadrature.

To sum up, we present a detailed analysis of the physics of squeezed propagating microwaves generated with a flux-driven JPA. We find 4.9 ± 0.2 dB of squeezing at 10 dB signal gain. In the degenerate mode, we verify that our JPA, as a phase-sensitive device, adds less noise to the amplified quadrature than an ideal phase-insensitive amplifier. This property is of utmost importance for high efficiency detection, state tomography and quantum communication applications in the microwave domain. In these protocols, a key resource is entanglement which we consider in the next section.

5.4 Path entanglement

Fascinatingly, quantum mechanics allows for a compound system to have a common description while, at the same time, no individual states can be ascribed to its subsystems [3]. The presence of entanglement between spatially separated systems is a necessary condition for what Einstein called “spooky action at a distance” [145]: the contradiction between quantum mechanics and local realism [3, 146]. Furthermore, entanglement is at the heart of quantum communication and information processing technologies, which promise significant performance gains over classical protocols [3–5]. Consequently, entanglement has been extensively explored in atomic physics and quantum optics [4, 5, 147]. In these investigations, optical frequencies were preferred over microwaves because the higher photon energies facilitate prac-

tical applications. However, since the late 1990s, microwave technology has evolved rapidly in both industry and science. For one thing, classical microwave fields have become an indispensable tool in mobile communication. For another, a promising direction towards scalable quantum information processing has appeared with the advent of superconducting microwave quantum circuits [6, 7, 9]. Despite some decoherence issues, these systems provide unprecedented light-matter coupling strengths due to their large effective dipole moments and field enhancement effects [18, 22]. As a consequence, standing-wave fields in transmission line resonators were shown to act as a short-range quantum bus between superconducting qubits [148, 149] and various gates were implemented [148–152]. For microwave quantum communication, however, propagating fields are required. As a first step in this direction, early experiments demonstrated tomography of weak thermal states [58], coherent states [57], and single photons [13]. Next, continuous-variable states generated by Josephson parametric devices were reconstructed [56]. Very recently, such devices have permitted to investigate two-mode squeezing [34, 44] and frequency non-degenerate path entanglement [62]. An important aspect of these experiments is the understanding they provide regarding entanglement. In order to be a resource in quantum communication protocols, it must occur between spatially separated subsystems [3]. Furthermore, a strict proof of entanglement requires the entangler and the detector to be based on independent experimental techniques. In this work, we make a significant step beyond previous efforts and demonstrate frequency-degenerate path entanglement in the microwave regime. We respect both criteria mentioned above by directly measuring the correlations between two different propagation paths. Our experiments follow the spirit of the quantum-optical realization [147] of the original Einstein-Podolsky-Rosen (EPR) paradox [146]. As shown in Fig. 5.8, we combine a vacuum and a squeezed vacuum state in a hybrid ring microwave beam splitter [89] acting as an entangling device. Its two output ports hold a continuous-variable state which is frequency-degenerate and entangled with respect to the two propagation paths. Along these paths, the entanglement can be conveniently distributed to two parties requiring it for any suitable quantum communication protocol. In our experiments, we first reconstruct the squeezed *input* state by means of dual-path tomography [57], which assumes knowledge of the beam splitter relations (cf. Sec. 5.3.1 and Sec. 5.3.2). Next, we reconstruct the moments of the *output* state after the beam splitter by treating the latter as a black box and calibrating against a known state [28]. In this reference-state method (cf. Sec. 2.9), we only assume that independent vacuum states are produced in each output path when vacuum is incident

at both input ports. From the moments reconstructed in this way, we build a witness matrix which proves the existence of path entanglement independently of the detailed nature of our output state [97]. Since in practice the data shows that our states are Gaussian, we finally quantify the degree of entanglement by means of the negativity [98]. The result of this analysis agrees with what we expect for our squeezed input state. We note here that for bipartite single-mode Gaussian entanglement, as it is relevant in our case, entanglement implies nonlocality [3, 5]. All in all, our results show that we have realized the main building block for microwave quantum teleportation and communication protocols.

The characterization of the input fields of the beam splitter is considered in Sec. 5.3.2. Here, we investigate the output state of the beam splitter. With the moments reconstructed using the reference-state method, we build an entanglement witness matrix. For the determination of the moments, we typically average over $7.7 \times 10^8 - 5.7 \times 10^9$ samples and all subsequently given error bars are based on this statistics. Our witness indicates path entanglement in the outputs for a squeezed state input present at the JPA-port of the beam splitter, while it does not do so for a vacuum state input. Next, we analyze the third and fourth order cumulants and find them to be small for JPA signal gains up to 10 dB. Since this is a strong indication for Gaussian states, we explore the path entanglement generated in our setup quantitatively via the negativity \mathcal{N}_{out} . For positive values, \mathcal{N}_{out} describes the degree of entanglement produced between the beam splitter output paths (cf. Sec. 2.11). In the limit of low JPA signal gain, Fig. 5.17 shows how \mathcal{N}_{out} becomes suppressed when sending more and more thermal photons into the JPA. At some point, the JPA cannot squeeze the incoming field below the vacuum anymore and the output state is no longer entangled.

For constant temperature, Fig. 5.18 shows how \mathcal{N}_{out} increases with increasing signal gain from zero to a value $\mathcal{N}_{\text{out,max}} = 0.55 \pm 0.04$ at 10 dB signal gain. This behavior is in good agreement with the negativity $\mathcal{N}_{\text{calc}}$ calculated from the dual-path reconstructed input state. Again, we observe a suppression for large thermal fields sent into the JPA. Our results confirm the expectation [60] that the degree of squeezing at the beam splitter input determines the amount of entanglement generated between the output paths. However, since $\mathcal{N}_{\text{calc}}$ is generally slightly lower than \mathcal{N}_{out} , we conclude that either the dual-path reconstruction underestimates the squeezing at the beam splitter input or the reference-state method ignores a small amount of spurious classical correlations between the two paths. Both effects are consistent with the data shown in Fig. 5.17, where at constant signal gain, the curve

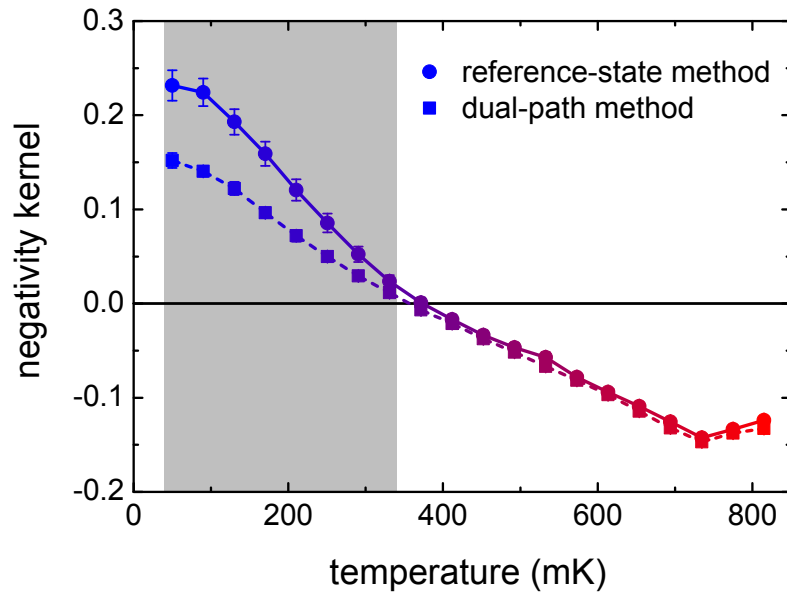


Figure 5.17: Path entanglement generated applying squeezed thermal states. The negativities \mathcal{N}_{out} , $\mathcal{N}_{\text{calc}}$ are the maxima of the corresponding negativity kernels $\tilde{\mathcal{N}}_{\text{out}}$, $\tilde{\mathcal{N}}_{\text{calc}}$ and 0. Circular symbols: $\tilde{\mathcal{N}}_{\text{out}}$ data at the beam splitter output. Square symbols: $\tilde{\mathcal{N}}_{\text{calc}}$ calculated from the reconstructed input state. The lines are guides to the eye. Negativity kernel versus attenuator temperature (color code) at 1 dB signal gain. For the data points in the shaded area, the witness matrix [97] confirms entanglement. Reprinted figure with permission from Ref. [61]. Copyright (2012) by the American Physical Society.

measured with the reference-state method at the beam splitter output converges for high temperatures to that calculated from the dual-path reconstructed input state. We finally note that the path-entangled state is expected to be a two-mode squeezed state with two additional local squeezing operations applied to it [60]. Since local operations do not change the amount of entanglement, the negativity $\mathcal{N}_{\text{out,max}} = 0.55 \pm 0.04$ implies that the two-mode squeezed state before the two local operations would have a variance squeezed by 3.2 ± 0.2 dB below that of the two-mode vacuum. All in all, we present clear evidence for path entanglement generated by combining two frequency-degenerate continuous-variable microwave fields, the vacuum and the squeezed vacuum, in a beam splitter.

To sum up this chapter, we present a detailed characterization of a flux-driven JPA regarding its amplification and noise properties in the degenerate and non-degenerate operation mode. The latter allows us to create continuous-variable quantum states, which are studied in detail applying the dual-path state reconstruction method. Making use of these quantum states, we demonstrate the generation and detection of frequency-degenerate path entanglement.

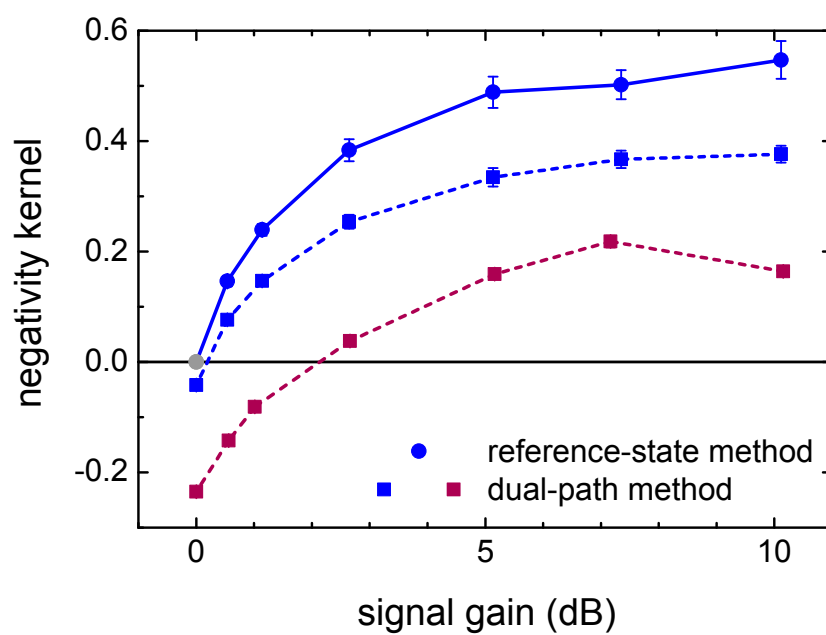


Figure 5.18: Dependence of the path entanglement on the JPA signal gain. The blue (red) curves are recorded at 50 mK (573 mK). Grey point: negativity of the reference state, assumed to be zero. Reprinted figure with permission from Ref. [61]. Copyright (2012) by the American Physical Society.

Chapter 6

Conclusions and outlook

The results of this thesis constitute a significant contribution to the progress of the new and highly active research area of propagating quantum microwaves. Propagating microwave fields offer a great potential for applications in quantum electrodynamics. However, the low energy scale of the microwave photons make a simple adoption of well-known quantum-optical strategies impossible. Accepting this challenge, we succeeded to extend the experimental investigation of propagating microwaves to the quantum regime. In particular, we establish the foundations as well as the experimental techniques and resources for quantum information processing and quantum communication with continuous-variable microwaves.

Our first main result is the invention of the dual-path state reconstruction method for propagating quantum microwaves. In order to address this problem, one has to deal with the absence of efficient single-photon detectors working at microwave frequencies. Instead, our reconstruction method uses a cryogenic beam splitter, linear amplifiers with a finite noise temperature, and signal recovery techniques to provide simultaneous access to, in principle, all moments of signal and amplifier noise. Exploiting suitable cross-correlations as well as massive and efficient averaging, our approach tolerates significant amplifier noise.

Second, we experimentally test our method with weak classical microwave signals. Applying thermal states, we perform Planck spectroscopy and corroborate the functionality of our beam splitters for signals on the quantum level. Using statistical mixtures of phase-shifted microwave pulses, we confirm that we can detect third order moments for such weak signals.

Third, we generate non-classical squeezed vacuum states by applying a Josephson parametric amplifier (JPA) and reconstruct them with an advanced dual-path setup. Applying realtime data processing, we measure moments up to the fourth order. By

considering cumulants up to this order, we confirm the Gaussianity of the states for JPA signal gains up to 10 dB. At this operation point, we obtain the maximum squeezing of 4.9 ± 0.2 dB referred to the beam splitter input.

Finally, we use the dual-path setup with a squeezed input state to observe the quantum physics of path-entangled microwave beams. We confirm experimentally that the beam splitter input states are such that the output state must be entangled. In addition, we characterize this output state directly applying an independent analysis technique, where we treat the beam splitter as a “black box” device. In this way, we find that the maximum entanglement contained in the output state is equivalent to 3.2 dB of two-mode squeezing, occurring at 10 dB JPA signal gain.

Currently, we are continuing the research on propagating quantum microwaves by investigating squeezed state physics. More precisely, our work in progress considers the generation and reconstruction of squeezed coherent states. Figure 6.1(a) and Fig. 6.1(b) display $1/e$ -contours of measured squeezed coherent states. When the anti-squeezing direction is collinear to the displacement vector of the coherent input state, the displacement of the squeezed state is maximal. In Fig. 6.1(a), we are close to this situation. As expected, we observe that the squeezed coherent state physics is governed by the phase of the coherent state at the input of the JPA, while we control and stabilize the coherent state phase at the output of the inactive JPA. In Fig. 6.1(b), the anti-squeezing direction is almost perpendicular to the coherent displacement vector. In this situation, the displacement of the squeezed coherent state is small since the coherent state displacement is deamplified. Additionally, the squeezed coherent state is shifted along the anti-squeezed direction due to the imperfect alignment already mentioned above. This shift is obviously larger than in Fig. 6.1(a) where it occurs along the squeezed direction and is therefore deamplified. As it can be seen from Fig. 6.1(c) and (d), the agreement between experiment and theory regarding the orientation and position of the squeezed state ellipse is excellent. However, the area enclosed by the experimental contour is larger than the theoretical one. The reason for this are effective thermal photons which are contained in the state due to losses or residual JPA noise contributions. For simplicity reasons, we only mention that the area of the squeezed vacuum ellipse is the same as the one of the squeezed coherent ellipse and refer the reader to Ref. [59] for further details.

One limitation of our current setup for the investigation of squeezed coherent states is that large displacements, especially along the anti-squeeze direction, are hard to achieve due to JPA compression effects. Therefore, we want to displace squeezed vacuum states by applying a directional coupler in the near future. In this

highly asymmetric beam splitter, the transmission for the squeezed vacuum input state is close to unity, whereas the coherent state is strongly attenuated before both are superposed. With such a setup, we plan to further extend our studies on squeezing physics and compare the generated coherent squeezed states to squeezed coherent states. In this way, we will be able to characterize the implementation

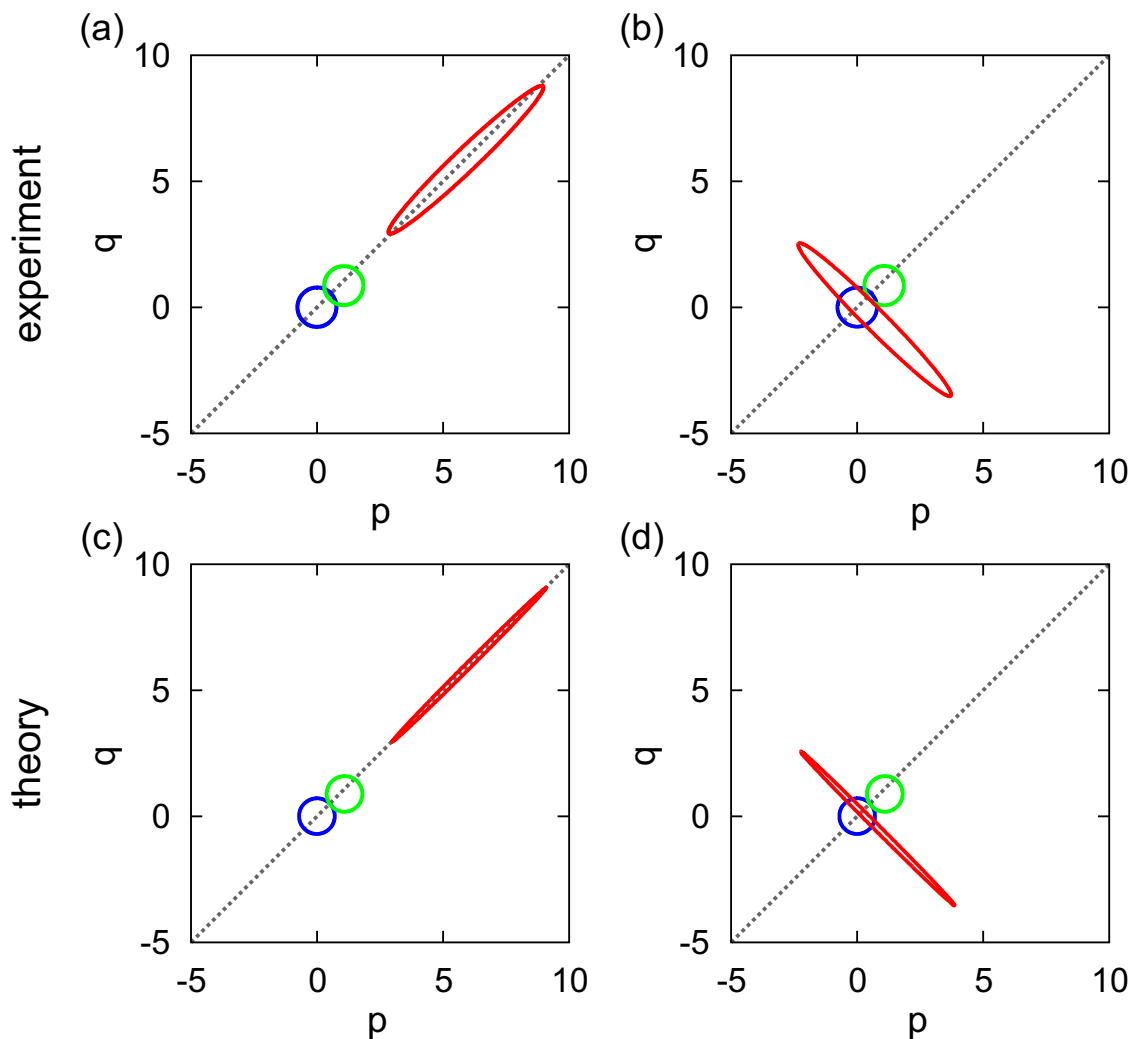


Figure 6.1: Squeezed coherent states. (a) and (b): $1/e$ -contours of reconstructed Wigner functions. Green: coherent state referred to the input of the JPA. The misalignment of the coherent displacement vector from the angle bisector (dotted line) is $6.2 \pm 0.2^\circ$. Red: squeezed coherent state at the input of the hybrid ring. Blue: vacuum. (c) and (d): $1/e$ -contours of theoretical Wigner functions. The calculations are based on the experimentally determined squeeze factor of 1.809 ± 0.001 , the coherent state photon number of 1.972 ± 0.005 and the angle of $6.2 \pm 0.2^\circ$ between input and output of the active JPA. In panel (a) and (c) the dotted line represents the anti-squeeze direction ($\gamma = 45^\circ$) and in panel (b) and (d) the squeeze direction ($\gamma = 135^\circ$).

of the displacement operator, which is a key element in remote state preparation or quantum teleportation protocols. These applications represent the mid-term goals for our experimental work exploiting continuous-variable propagating quantum microwaves. Our successful demonstration of path entanglement already provides a good basis for further research towards the realization of these protocols. Regarding the latter, one challenge is the reduction of losses which diminish the entanglement by mixing the quantum state with vacuum or thermal fluctuations. An ansatz for this is to avoid interconnections by combining different elements on a single chip and to avoid dielectrics by using wave guides for long transmission lines. Another challenge is the temporal mode matching of the classical communication signal and the EPR state, which could be solved by applying entangled states with slowly decreasing correlations or ultra-low-loss delay lines. Regarding the grand goal of quantum microwave communication over macroscopic distances, our results allow for the optimistic outlook that fundamental protocols such as state teleportation between two nearby laboratories are certainly challenging, but by no way impossible even with present-day technology.

Appendix A

Superconducting coil and persistent current switch

For the generation of a static magnetic flux bias for the JPA, we use a superconducting coil [cf. Fig. A.1(a)] equipped with a persistent current switch [cf. Fig. A.1(b) and (c)]. The latter allows to freeze a persistent current in the coil. This provides an effective isolation from current noise possibly present on the coil leads. The circuit diagram is shown in Fig. A.1(d). The coil is wound from a S1-1,5(0,10)V superconducting wire from European Advanced Superconductors consisting of a single NbTi filament embedded in a copper matrix. The conductor diameter is 0.1 mm. The coil frame material is gold-plated OFHC copper. The 4416 windings are distributed on 46 layers. For better thermal anchoring of the wire, it has been wound in Stycast 1266, which needed to harden after 2 to 3 layers. The twisted leads of the coil are well anchored with GE varnish over their complete length, e.g., following the windings of the coil exchanger, to prevent quenches and to reduce the heat load. Thus, after installing the coil system the base temperature increases by less than 1 mK. The coil is tested with currents up to 200 mA and no changes in the fridge performance is observed. Figure A.2 shows a numerical calculation of the z -component of the magnetic field. The simulation agrees well with the magnetic field determined with a niobium SQUID without resonator (data not shown). In order to change the flux in the SQUID loop of the JPA by the amount Φ_0 , we expect a field value of 0.21 mT requiring for a coil current of 3.1 mA. However, a current of only 138 μ A is sufficient to change the flux by Φ_0 . Therefore, the flux is concentrated in the small gaps between the superconducting ground planes of the resonator. We note that large magnetic fields can degrade the performance of the JPA. As a remedy, the JPA has to be heated above the critical temperature of niobium to release trapped

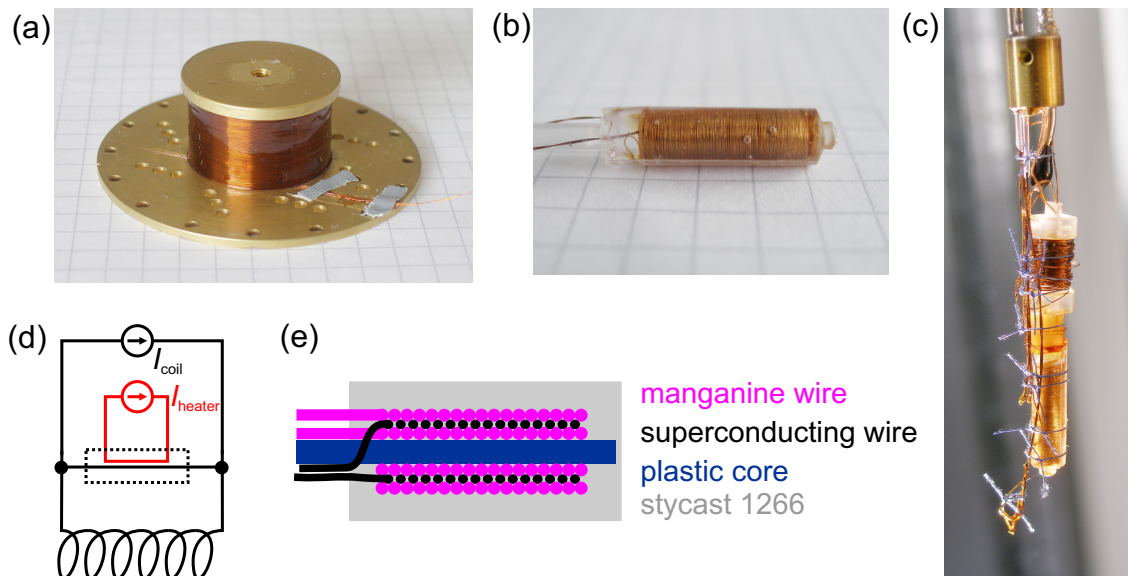


Figure A.1: Superconducting coil and persistent current switch. (a) Photograph of the superconducting coil. (b) Photograph of the persistent current switch before assembly. (c) Installed persistent current switch without protective tube. (d) Circuit diagram. The dashed rectangle represents the persistent current switch. (e) Cross-sectional schematics of the persistent current switch.

flux.

The coil is equipped with a persistent current switch. A cross-section of this switch is displayed in Fig. A.1(e). Between two layers of Manganin heating wire there is a layer of superconducting wire. It is wound in a bifilar fashion in order to be insensitive to external flux variations and to prevent cross-talk from the heater wire. The characteristics of the persistent current switch is shown in Fig. A.3. For heater currents up to 25 mA, the switch filament is superconducting. Above 25 mA the superconductivity breaks down. The switch is in a stable resistive state for heater currents above 33 mA. We usually operate the switch at a heating current of 80 mA resulting in a larger filament resistance and a faster change of the coil current.

The persistent current switch is connected to the superconducting coil by point welding the NbTi filaments after removing the copper matrix. We generate the coil current with a home-made ultra-low-noise current source controlled via a National Instruments 16 bit digital-to-analog converter board (NI PCI-6052E). We filter the coil leads with a combination of a Mini-Circuits BLP-1.9 and a home-made RC lowpass filter. Except for flux sweeps, we always operate the coil in the persistent mode.

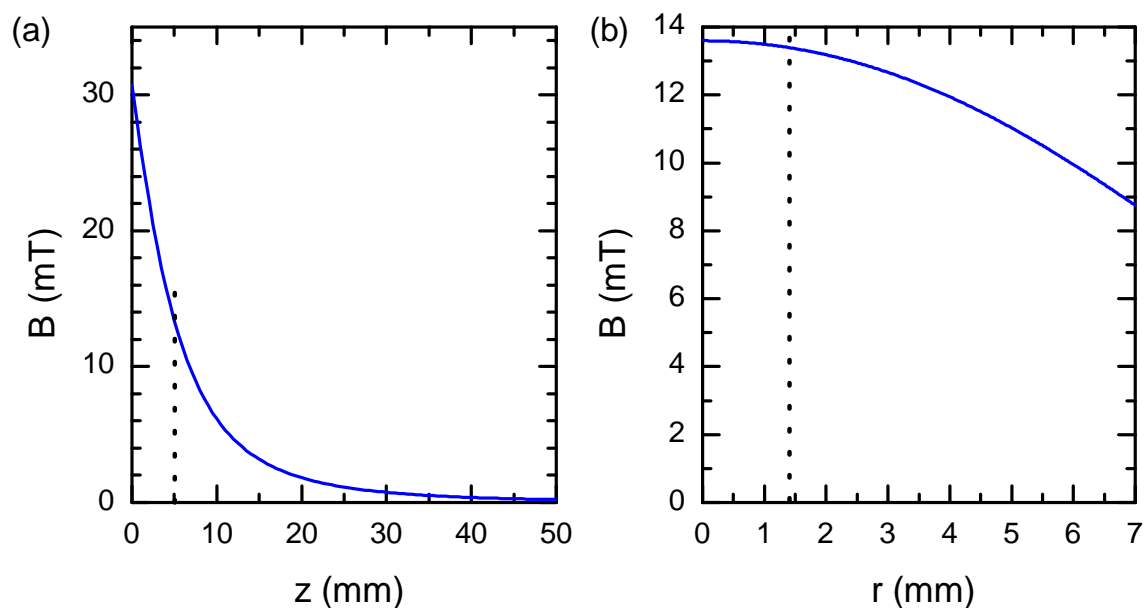


Figure A.2: Calculated axial (z) component of the magnetic field of the superconducting coil for a current of 200 mA. (a) Magnetic field vs. the distance from the coil plate for a radial position of 1.4 mm. The dashed line marks the JPA position of 5 mm. (b) Magnetic field vs. the radial distance from the coil axis. The dashed line marks the SQUID position of 1.4 mm, where the calculated field is 13.4 mT.

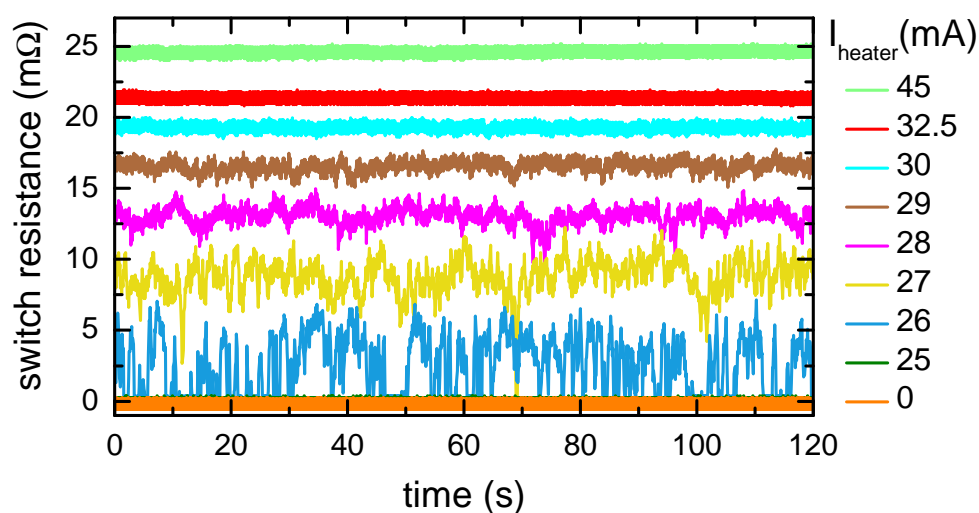


Figure A.3: Characteristics of the persistent current switch immersed in liquid Helium. The current through the switch filament is 150 mA.

Bibliography

- [1] Y. Nakamura & T. Yamamoto. Breakthroughs in Photonics 2012: Breakthroughs in Microwave Quantum Photonics in Superconducting Circuits. *IEEE Photon. J.* **5**, 0701406 (2013).
- [2] M. A. Nielsen & I. L. Chuang. *Quantum Computation and Quantum Information* (Cambridge University Press, Cambridge, 2010).
- [3] R. Horodecki, P. Horodecki, M. Horodecki & K. Horodecki. Quantum entanglement. *Rev. Mod. Phys.* **81**, 865–942 (2009).
- [4] J. M. Raimond, M. Brune & S. Haroche. Manipulating quantum entanglement with atoms and photons in a cavity. *Rev. Mod. Phys.* **73**, 565–582 (2001).
- [5] S. L. Braunstein & P. van Loock. Quantum information with continuous variables. *Rev. Mod. Phys.* **77**, 513–577 (2005).
- [6] R. J. Schoelkopf & S. M. Girvin. Wiring up quantum systems. *Nature* **451**, 664–669 (2008).
- [7] J. Clarke & F. K. Wilhelm. Superconducting quantum bits. *Nature* **453**, 1031–1042 (2008).
- [8] M. Reagor, H. Paik, G. Catelani, L. Sun, C. Axline, E. Holland, I. M. Pop, N. A. Masluk, T. Brecht, L. Frunzio, M. H. Devoret, L. Glazman & R. J. Schoelkopf. Reaching 10 ms single photon lifetimes for superconducting aluminum cavities. *Appl. Phys. Lett.* **102**, 192604 (2013).
- [9] M. Mariantoni, H. Wang, T. Yamamoto, M. Neeley, R. C. Bialczak, Y. Chen, M. Lenander, E. Lucero, A. D. O’Connell, D. Sank, M. Weides, J. Wenner, Y. Yin, J. Zhao, A. N. Korotkov, A. N. Cleland & J. M. Martinis. Implementing the Quantum von Neumann Architecture with Superconducting Circuits. *Science* **334**, 61–65 (2011).

-
- [10] E. Lucero, R. Barends, Y. Chen, J. Kelly, M. Mariantoni, A. Megrant, P. O'Malley, D. Sank, A. Vainsencher, J. Wenner, T. White, Y. Yin, A. N. Cleland & J. M. Martinis. Computing prime factors with a Josephson phase qubit quantum processor. *Nature Phys.* **8**, 719–723 (2012).
- [11] L. Steffen, Y. Salathe, M. Oppliger, P. Kurpiers, M. Baur, C. Lang, C. Eichler, G. Puebla-Hellmann, A. Fedorov & A. Wallraff. Deterministic quantum teleportation with feed-forward in a solid state system. *Nature* **500**, 319–322 (2013).
- [12] A. A. Houck, D. I. Schuster, J. M. Gambetta, J. A. Schreier, B. R. Johnson, J. M. Chow, L. Frunzio, J. Majer, M. H. Devoret, S. M. Girvin & R. J. Schoelkopf. Generating single microwave photons in a circuit. *Nature* **449**, 328–331 (2007).
- [13] D. Bozyigit, C. Lang, L. Steffen, J. M. Fink, C. Eichler, M. Baur, R. Bianchetti, P. J. Leek, S. Filipp, M. P. da Silva, A. Blais & A. Wallraff. Antibunching of microwave-frequency photons observed in correlation measurements using linear detectors. *Nature Phys.* **7**, 154–158 (2011).
- [14] M. Hofheinz, H. Wang, M. Ansmann, R. C. Bialczak, E. Lucero, M. Neeley, A. D. O'Connell, D. Sank, J. Wenner, J. M. Martinis & A. N. Cleland. Synthesizing arbitrary quantum states in a superconducting resonator. *Nature* **459**, 546–549 (2009).
- [15] G. Wendin & V. S. Shumeiko. Quantum bits with Josephson junctions (Review Article). *Low Temp. Phys.* **33**, 724–744 (2007).
- [16] M. H. Devoret & R. J. Schoelkopf. Superconducting Circuits for Quantum Information: An Outlook. *Science* **339**, 1169–1174 (2013).
- [17] A. Blais, R.-S. Huang, A. Wallraff, S. M. Girvin & R. J. Schoelkopf. Cavity quantum electrodynamics for superconducting electrical circuits: An architecture for quantum computation. *Phys. Rev. A* **69**, 062320 (2004).
- [18] A. Wallraff, D. I. Schuster, A. Blais, L. Frunzio, R.-S. Huang, J. Majer, S. Kumar, S. M. Girvin & R. J. Schoelkopf. Strong coupling of a single photon to a superconducting qubit using circuit quantum electrodynamics. *Nature* **431**, 162–167 (2004).

- [19] A. Blais, J. Gambetta, A. Wallraff, D. I. Schuster, S. M. Girvin, M. H. Devoret & R. J. Schoelkopf. Quantum-information processing with circuit quantum electrodynamics. *Phys. Rev. A* **75**, 032329 (2007).
- [20] S. Haroche. Controlling Photons in a Box and Exploring the Quantum to Classical Boundary. *Nobel Lecture* (2012). URL http://www.nobelprize.org/nobel_prizes/physics/laureates/2012/haroche-lecture.html.
- [21] S. Haroche. Nobel Lecture: Controlling photons in a box and exploring the quantum to classical boundary. *Rev. Mod. Phys.* **85**, 1083–1102 (2013).
- [22] T. Niemczyk, F. Deppe, H. Huebl, E. P. Menzel, F. Hocke, M. J. Schwarz, J. J. Garcia-Ripoll, D. Zueco, T. Hümmer, E. Solano, A. Marx & R. Gross. Circuit quantum electrodynamics in the ultrastrong-coupling regime. *Nature Phys.* **6**, 772–776 (2010).
- [23] M. A. Castellanos-Beltran, K. D. Irwin, G. C. Hilton, L. R. Vale & K. W. Lehnert. Amplification and squeezing of quantum noise with a tunable Josephson metamaterial. *Nature Phys.* **4**, 929–931 (2008).
- [24] B. Yurke. Squeezed-state generation using a Josephson parametric amplifier. *J. Opt. Soc. Am. B* **4**, 1551–1557 (1987).
- [25] R. Movshovich, B. Yurke, P. G. Kaminsky, A. D. Smith, A. H. Silver, R. W. Simon & M. V. Schneider. Observation of Zero-Point Noise Squeezing via a Josephson-Parametric Amplifier. *Phys. Rev. Lett.* **65**, 1419–1422 (1990).
- [26] W. P. Schleich. *Quantum Optics in Phase Space* (Wiley-VCH Verlag, Berlin, 2001).
- [27] N. J. Cerf, G. Leuchs & E. S. Polzik (eds.) *Quantum Information with Continuous Variables of Atoms and Light* (Imperial College Press, London, 2007).
- [28] C. Eichler, D. Bozyigit, C. Lang, L. Steffen, J. Fink & A. Wallraff. Experimental State Tomography of Itinerant Single Microwave Photons. *Phys. Rev. Lett.* **106**, 220503 (2011).
- [29] O. Astafiev, A. M. Zagoskin, A. A. Abdumalikov, Jr., Yu. A. Pashkin, T. Yamamoto, K. Inomata, Y. Nakamura & J. S. Tsai. Resonance Fluorescence of a Single Artificial Atom. *Science* **327**, 840–843 (2010).

- [30] I.-C. Hoi, C. M. Wilson, G. Johansson, T. Palomaki, B. Peropadre & P. Delsing. Demonstration of a Single-Photon Router in the Microwave Regime. *Phys. Rev. Lett.* **107**, 073601 (2011).
- [31] I.-C. Hoi, T. Palomaki, J. Lindkvist, G. Johansson, P. Delsing & C. M. Wilson. Generation of Nonclassical Microwave States Using an Artificial Atom in 1D Open Space. *Phys. Rev. Lett.* **108**, 263601 (2012).
- [32] A. A. Abdumalikov, Jr., O. Astafiev, A. M. Zagoskin, Yu. A. Pashkin, Y. Nakamura & J. S. Tsai. Electromagnetically Induced Transparency on a Single Artificial Atom. *Phys. Rev. Lett.* **104**, 193601 (2010).
- [33] O. V. Astafiev, A. A. Abdumalikov, Jr., A. M. Zagoskin, Yu. A. Pashkin, Y. Nakamura & J. S. Tsai. Ultimate On-Chip Quantum Amplifier. *Phys. Rev. Lett.* **104**, 183603 (2010).
- [34] C. M. Wilson, G. Johansson, A. Pourkabirian, M. Simoen, J. R. Johansson, T. Duty, F. Nori & P. Delsing. Observation of the dynamical Casimir effect in a superconducting circuit. *Nature* **479**, 376–379 (2011).
- [35] N. J. Cerf, M. Lévy & G. Van Assche. Quantum distribution of Gaussian keys using squeezed states. *Phys. Rev. A* **63**, 052311 (2001).
- [36] F. Grosshans, G. Van Assche, J. Wenger, R. Brouri, N. J. Cerf & P. Grangier. Quantum key distribution using gaussian-modulated coherent states. *Nature* **421**, 238–241 (2003).
- [37] A. Furusawa, J. L. Sørensen, S. L. Braunstein, C. A. Fuchs, H. J. Kimble & E. S. Polzik. Unconditional Quantum Teleportation. *Science* **282**, 706–709 (1998).
- [38] T. C. Zhang, K. W. Goh, C. W. Chou, P. Lodahl & H. J. Kimble. Quantum teleportation of light beams. *Phys. Rev. A* **67**, 033802 (2003).
- [39] W. P. Bowen, N. Treps, B. C. Buchler, R. Schnabel, T. C. Ralph, H.-A. Bachor, T. Symul & P. K. Lam. Experimental investigation of continuous-variable quantum teleportation. *Phys. Rev. A* **67**, 032302 (2003).
- [40] B. Julsgaard, A. Kozhekin & E. S. Polzik. Experimental long-lived entanglement of two macroscopic objects. *Nature* **413**, 400–403 (2001).

- [41] C. Schori, B. Julsgaard, J. L. Sørensen & E. S. Polzik. Recording Quantum Properties of Light in a Long-Lived Atomic Spin State: Towards Quantum Memory. *Phys. Rev. Lett.* **89**, 057903 (2002).
- [42] M. P. da Silva, D. Bozyigit, A. Wallraff & A. Blais. Schemes for the observation of photon correlation functions in circuit QED with linear detectors. *Phys. Rev. A* **82**, 043804 (2010).
- [43] Y. Yin, Y. Chen, D. Sank, P. J. J. O'Malley, T. C. White, R. Barends, J. Kelly, E. Lucero, M. Mariantoni, A. Megrant, C. Neill, A. Vainsencher, J. Wenner, A. N. Korotkov, A. N. Cleland & J. M. Martinis. Catch and Release of Microwave Photon States. *Phys. Rev. Lett.* **110**, 107001 (2013).
- [44] C. Eichler, D. Bozyigit, C. Lang, M. Baur, L. Steffen, J. M. Fink, S. Filipp & A. Wallraff. Observation of Two-Mode Squeezing in the Microwave Frequency Domain. *Phys. Rev. Lett.* **107**, 113601 (2011).
- [45] C. Lang, D. Bozyigit, C. Eichler, L. Steffen, J. M. Fink, A. A. Abdumalikov, Jr., M. Baur, S. Filipp, M. P. da Silva, A. Blais & A. Wallraff. Observation of Resonant Photon Blockade at Microwave Frequencies Using Correlation Function Measurements. *Phys. Rev. Lett.* **106**, 243601 (2011).
- [46] G. Kirchmair, B. Vlastakis, Z. Leghtas, S. E. Nigg, H. Paik, E. Ginossar, M. Mirrahimi, L. Frunzio, S. M. Girvin & R. J. Schoelkopf. Observation of quantum state collapse and revival due to the single-photon Kerr effect. *Nature* **495**, 205–209 (2013).
- [47] A. I. Lvovsky & M. G. Raymer. Continuous-variable optical quantum-state tomography. *Rev. Mod. Phys.* **81**, 299–332 (2009).
- [48] A. I. Lvovsky, H. Hansen, T. Aichele, O. Benson, J. Mlynek & S. Schiller. Quantum State Reconstruction of the Single-Photon Fock State. *Phys. Rev. Lett.* **87**, 050402 (2001).
- [49] U. Leonhardt. *Measuring the Quantum State of Light* (Cambridge University Press, Cambridge, 1997).
- [50] F. Helmer, M. Mariantoni, E. Solano & F. Marquardt. Quantum nondemolition photon detection in circuit QED and the quantum Zeno effect. *Phys. Rev. A* **79**, 052115 (2009).

-
- [51] G. Romero, J. J. García-Ripoll & E. Solano. Microwave Photon Detector in Circuit QED. *Phys. Rev. Lett.* **102**, 173602 (2009).
- [52] G. Romero, J. J. García-Ripoll & E. Solano. Photodetection of propagating quantum microwaves in circuit QED. *Phys. Scr.* **T137**, 014004 (2009).
- [53] B. Peropadre, G. Romero, G. Johansson, C. M. Wilson, E. Solano & J. J. García-Ripoll. Approaching perfect microwave photodetection in circuit QED. *Phys. Rev. A* **84**, 063834 (2011).
- [54] A. Poudel, R. McDermott & M. G. Vavilov. Quantum efficiency of a microwave photon detector based on a current-biased Josephson junction. *Phys. Rev. B* **86**, 174506 (2012).
- [55] Y.-F. Chen, D. Hover, S. Sendelbach, L. Maurer, S. T. Merkel, E. J. Pritchett, F. K. Wilhelm & R. McDermott. Microwave Photon Counter Based on Josephson Junctions. *Phys. Rev. Lett.* **107**, 217401 (2011).
- [56] F. Mallet, M. A. Castellanos-Beltran, H. S. Ku, S. Glancy, E. Knill, K. D. Irwin, G. C. Hilton, L. R. Vale & K. W. Lehnert. Quantum State Tomography of an Itinerant Squeezed Microwave Field. *Phys. Rev. Lett.* **106**, 220502 (2011).
- [57] E. P. Menzel, F. Deppe, M. Mariani, M. Á. Araque Caballero, A. Baust, T. Niemczyk, E. Hoffmann, A. Marx, E. Solano & R. Gross. Dual-Path State Reconstruction Scheme for Propagating Quantum Microwaves and Detector Noise Tomography. *Phys. Rev. Lett.* **105**, 100401 (2010).
- [58] M. Mariani, E. P. Menzel, F. Deppe, M. Á. Araque Caballero, A. Baust, T. Niemczyk, E. Hoffmann, E. Solano, A. Marx & R. Gross. Planck Spectroscopy and Quantum Noise of Microwave Beam Splitters. *Phys. Rev. Lett.* **105**, 133601 (2010).
- [59] L. Zhong, E. P. Menzel, R. Di Candia, P. Eder, M. Ihmig, A. Baust, M. Haerberlein, E. Hoffmann, K. Inomata, T. Yamamoto, Y. Nakamura, E. Solano, F. Deppe, A. Marx & R. Gross. Squeezing with a flux-driven Josephson parametric amplifier. *New J. Phys.* **15**, 125013 (2013). Doi: 10.1088/1367-2630/15/12/125013.
- [60] M. S. Kim, W. Son, V. Bužek & P. L. Knight. Entanglement by a beam splitter: Nonclassicality as a prerequisite for entanglement. *Phys. Rev. A* **65**, 032323 (2002).

- [61] E. P. Menzel, R. Di Candia, F. Deppe, P. Eder, L. Zhong, M. Ihmig, M. Haerberlein, A. Baust, E. Hoffmann, D. Ballester, K. Inomata, T. Yamamoto, Y. Nakamura, E. Solano, A. Marx & R. Gross. Path Entanglement of Continuous-Variable Quantum Microwaves. *Phys. Rev. Lett.* **109**, 250502 (2012).
- [62] E. Flurin, N. Roch, F. Mallet, M. H. Devoret & B. Huard. Generating Entangled Microwave Radiation Over Two Transmission Lines. *Phys. Rev. Lett.* **109**, 183901 (2012).
- [63] D. M. Pozar. *Microwave Engineering* (John Wiley & Sons, Inc., New York, 2005).
- [64] M. O. Scully & M. S. Zubairy. *Quantum optics* (Cambridge University Press, Cambridge, 1997).
- [65] E. Wigner. On the Quantum Correction For Thermodynamic Equilibrium. *Phys. Rev.* **40**, 749–759 (1932).
- [66] D. F. Walls & G. J. Milburn. *Quantum Optics* (Springer, Berlin, 2008).
- [67] J. E. Moyal. Quantum mechanics as a statistical theory. *Math. Proc. Camb. Phil. Soc.* **45**, 99–124 (1949).
- [68] M. Hillery, R. F. O’Connell, M. O. Scully & E. P. Wigner. Distribution functions in physics: Fundamentals. *Phys. Rep.* **106**, 121–167 (1984).
- [69] J. Bertrand & P. Bertrand. A Tomographic Approach to Wigner’s function. *Found. Phys.* **17**, 397–405 (1987).
- [70] R. J. Glauber. Coherent and Incoherent States of the Radiation Field. *Phys. Rev.* **131**, 2766–2788 (1963).
- [71] E. C. G. Sudarshan. Equivalence of Semiclassical and Quantum Mechanical Descriptions of Statistical Light Beams. *Phys. Rev. Lett.* **10**, 277–279 (1963).
- [72] N. Lütkenhaus & S. M. Barnett. Nonclassical effects in phase space. *Phys. Rev. A* **51**, 3340–3342 (1995).
- [73] A. Wünsche. Reconstruction of operators from their normally ordered moments for a single boson mode. *Quantum Opt.* **2**, 453–466 (1990).
- [74] C. T. Lee. Moment problem for a density matrix and a biorthogonal set of operator bases. *Phys. Rev. A* **46**, 6097–6099 (1992).

- [75] U. Herzog. Generating-function approach to the moment problem for the density matrix of a single mode. *Phys. Rev. A* **53**, 2889–2892 (1996).
- [76] V. Bužek, G. Adam & G. Drobný. Quantum state reconstruction and detection of quantum coherences on different observation levels. *Phys. Rev. A* **54**, 804–820 (1996).
- [77] S. N. Filippov & V. I. Man’ko. Evolution of Microwave Quantum States in Terms of Measurable Ordered Moments of Creation and Annihilation Operators. *Opt. Spectrosc.* **112**, 365–372 (2012).
- [78] S. N. Filippov & V. I. Man’ko. Measuring microwave quantum states: Tomogram and moments. *Phys. Rev. A* **84**, 033827 (2011).
- [79] A. Bednorz & W. Belzig. Fourth moments reveal the negativity of the Wigner function. *Phys. Rev. A* **83**, 052113 (2011).
- [80] M. Oxborrow, J. D. Breeze & N. M. Alford. Room-temperature solid-state maser. *Nature* **488**, 353–356 (2012).
- [81] C. M. Caves. Quantum limits on noise in linear amplifiers. *Phys. Rev. D* **26**, 1817–1839 (1982).
- [82] F. Deppe, M. Mariani, E. P. Menzel, A. Marx, S. Saito, K. Kakuyanagi, H. Tanaka, T. Meno, K. Semba, H. Takayanagi, E. Solano & R. Gross. Two-photon probe of the Jaynes-Cummings model and controlled symmetry breaking in circuit QED. *Nature Phys.* **4**, 686–691 (2008).
- [83] M. Mariani, F. Deppe, A. Marx, R. Gross, F. K. Wilhelm & E. Solano. Two-resonator circuit quantum electrodynamics: A superconducting quantum switch. *Phys. Rev. B* **78**, 104508 (2008).
- [84] J. M. Fink, R. Bianchetti, M. Baur, M. Göppl, L. Steffen, S. Filipp, P. J. Leek, A. Blais & A. Wallraff. Dressed Collective Qubit States and the Tavis-Cummings Model in Circuit QED. *Phys. Rev. Lett.* **103**, 083601 (2009).
- [85] T. Niemczyk, F. Deppe, M. Mariani, E. P. Menzel, E. Hoffmann, G. Wild, L. Eggenstein, A. Marx & R. Gross. Fabrication technology of and symmetry breaking in superconducting quantum circuits. *Supercond. Sci. Technol.* **22**, 034009 (2009).

- [86] A. A. Clerk, M. H. Devoret, S. M. Girvin, F. Marquardt & R. J. Schoelkopf. Introduction to quantum noise, measurement, and amplification. *Rev. Mod. Phys.* **82**, 1155–1208 (2010).
- [87] J. S. Lundeen, A. Feito, H. Coldenstrodt-Ronge, K. L. Pregnell, Ch. Silberhorn, T. C. Ralph, J. Eisert, M. B. Plenio & I. A. Walmsley. Tomography of quantum detectors. *Nature Phys.* **5**, 27–30 (2009).
- [88] P. Kok, W. J. Munro, K. Nemoto, T. C. Ralph, J. P. Dowling & G. J. Milburn. Linear optical quantum computing with photonic qubits. *Rev. Mod. Phys.* **79**, 135–174 (2007).
- [89] E. Hoffmann, F. Deppe, T. Niemczyk, T. Wirth, E. P. Menzel, G. Wild, H. Huebl, M. Mariani, T. Weißl, A. Lukashenko, A. P. Zhuravel, A. V. Ustinov, A. Marx & R. Gross. A superconducting 180° hybrid ring coupler for circuit quantum electrodynamics. *Appl. Phys. Lett.* **97**, 222508 (2010).
- [90] J. Gabelli, L.-H. Reydellet, G. Fève, J.-M. Berroir, B. Plaçais, P. Roche & D. C. Glattli. Hanbury Brown–Twiss Correlations to Probe the Population Statistics of GHz Photons Emitted by Conductors. *Phys. Rev. Lett.* **93**, 056801 (2004).
- [91] V. Bužek, G. Adam & G. Drobný. Reconstruction of Wigner Functions on Different Observation Levels. *Ann. Phys.* **245**, 37–97 (1996).
- [92] E. Fick & G. Sauermaun. *The Quantum Statistics of Dynamic Processes* (Springer Verlag, Berlin, 1990).
- [93] E. T. Jaynes. Information Theory and Statistical Mechanics. *Phys. Rev.* **106**, 620–630 (1957).
- [94] E. T. Jaynes & F. W. Cummings. Comparison of Quantum and Semiclassical Radiation Theories with Application to the Beam Maser. *Proc. IEEE* **51**, 89–109 (1963).
- [95] C. H. Bennett & S. J. Wiesner. Communication via One- and Two-Particle Operators on Einstein-Podolsky-Rosen States. *Phys. Rev. Lett.* **69**, 2881–2884 (1992).
- [96] C. H. Bennett, G. Brassard, C. Crépeau, R. Jozsa, A. Peres & W. K. Wootters. Teleporting an Unknown Quantum State via Dual Classical and Einstein-Podolsky-Rosen Channels. *Phys. Rev. Lett.* **70**, 1895–1899 (1993).

-
- [97] E. Shchukin & W. Vogel. Inseparability Criteria for Continuous Bipartite Quantum States. *Phys. Rev. Lett.* **95**, 230502 (2005).
- [98] G. Adesso & F. Illuminati. Gaussian measures of entanglement versus negativities: Ordering of two-mode Gaussian states. *Phys. Rev. A* **72**, 032334 (2005).
- [99] P. Hyllus & J. Eisert. Optimal entanglement witnesses for continuous-variable systems. *New J. Phys.* **8**, 51 (2006).
- [100] R. Schack & A. Schenzle. Moment hierarchies and cumulants in quantum optics. *Phys. Rev. A* **41**, 3847–3852 (1990).
- [101] L.-Z. Jiang. The Cumulants of Bosonic Quantum States. *Proc. SPIE* **7846**, 784612 (2010).
- [102] P. Eder. *Dual-path receiver for state reconstruction of propagating quantum microwaves*. Diploma thesis, Technische Universität München (2012). URL http://www.wmi.badw-muenchen.de/publications/theses/Eder,Peter_Diplomarbeit_2012.pdf.
- [103] R. E. Collin. *Foundations for Microwave Engineering* (Wiley-IEEE, New York, 2000).
- [104] S. B. Cohn. A Class of Broadband Three-Port TEM-Mode Hybrids. *IEEE Trans. Microw. Theory Tech.* **16**, 110–116 (1968).
- [105] M. Mariantoni. *New Trends in Superconducting Circuit Quantum Electrodynamics: Two Amplifiers, Two Resonators, and Two Photons*. Dissertation, Technische Universität München (2009). URL http://www.wmi.badw-muenchen.de/publications/theses/Mariantoni_Doktorarbeit_2009.pdf.
- [106] E. J. Wilkinson. An N-Way Hybrid Power Divider. *IRE Trans. Microw. Theory Tech.* **8**, 116–118 (1960).
- [107] M. Á. Araque Caballero. *A Setup for Quantum Signal Detection in a Circuit QED Architecture*. Diploma thesis, Technische Universität München (2008). URL http://www.wmi.badw-muenchen.de/publications/theses/Araque%20Caballero_Diplomarbeit_2008.pdf.

- [108] C. E. Shannon. Communication in the Presence of Noise. *Proc. IRE* **37**, 10–21 (1949).
- [109] H. Nyquist. Certain Topics in Telegraph Transmission Theory. *Transactions of the American Institute of Electrical Engineers* **47**, 617–644 (1928).
- [110] A. J. Jerri. The Shannon Sampling Theorem – Its Various Extensions and Applications: A Tutorial Review. *Proc. IEEE* **65**, 1565–1596 (1977).
- [111] B. Yurke, L. W. Rupp & P. G. Kaminsky. Use of the Josephson junction in fundamental quantum electronics experiments. *IEEE Trans. Magn.* **23**, 458–464 (1987).
- [112] B. Yurke, L. R. Corruccini, P. G. Kaminisky, L. W. Rupp, A. D. Smith, A. H. Silver, R. W. Simon & E. A. Whittaker. Observation of parametric amplification and deamplification in a Josephson parametric amplifier. *Phys. Rev. A* **39**, 2519–2533 (1989).
- [113] B. Yurke, M. L. Roukes, R. Movshovich & A. N. Pargellis. A low-noise series-array Josephson junction parametric amplifier. *Appl. Phys. Lett.* **69**, 3078–3080 (1996).
- [114] I. Siddiqi, R. Vijay, F. Pierre, C. M. Wilson, M. Metcalfe, C. Rigetti, L. Frunzio & M. H. Devoret. RF-Driven Josephson Bifurcation Amplifier for Quantum Measurement. *Phys. Rev. Lett.* **93**, 207002 (2004).
- [115] E. A. Tholén, A. Ergül, E. M. Doherty, F. M. Weber, F. Grégis & D. B. Haviland. Nonlinearities and parametric amplification in superconducting coplanar waveguide resonators. *Appl. Phys. Lett.* **90**, 253509 (2007).
- [116] M. A. Castellanos-Beltran & K. W. Lehnert. Widely tunable parametric amplifier based on a superconducting quantum interference device array resonator. *Appl. Phys. Lett.* **91**, 083509 (2007).
- [117] T. Yamamoto, K. Inomata, M. Watanabe, K. Matsuba, T. Miyazaki, W. D. Oliver, Y. Nakamura & J. S. Tsai. Flux-driven Josephson parametric amplifier. *Appl. Phys. Lett.* **93**, 042510 (2008).
- [118] B. Abdo, O. Suchoi, E. Segev, O. Shtempluck, M. Blencowe & E. Buks. Intermodulation and parametric amplification in a superconducting stripline resonator integrated with a dc-SQUID. *Europhys. Lett.* **85**, 68001 (2009).

- [119] C. Eichler & A. Wallraff. Controlling the dynamic range of a Josephson parametric amplifier. *arXiv preprint arXiv:1305.6583* (2013). URL <http://arxiv.org/abs/1305.6583>.
- [120] G. Wendin & V. Shumeiko. Superconducting Quantum Circuits, Qubits and Computing. *arXiv preprint arXiv:cond-mat/0508729* (2005). URL <http://arxiv.org/abs/cond-mat/0508729>.
- [121] B. Abdo, F. Schackert, M. Hatridge, C. Rigetti & M. Devoret. Josephson amplifier for qubit readout. *Appl. Phys. Lett.* **99**, 162506 (2011).
- [122] Z. R. Lin, K. Inomata, W. D. Oliver, K. Koshino, Y. Nakamura, J. S. Tsai & T. Yamamoto. Single-shot readout of a superconducting flux qubit with a flux-driven Josephson parametric amplifier. *Appl. Phys. Lett.* **103**, 132602 (2013).
- [123] J. D. Teufel, T. Donner, M. A. Castellanos-Beltran, J. W. Harlow & K. W. Lehnert. Nanomechanical motion measured with an imprecision below that at the standard quantum limit. *Nature Nanotech.* **4**, 820–823 (2009).
- [124] P. D. Nation, J. R. Johansson, M. P. Blencowe & F. Nori. *Colloquium* : Stimulating uncertainty: Amplifying the quantum vacuum with superconducting circuits. *Rev. Mod. Phys.* **84**, 1–24 (2012).
- [125] A. M. Zagoskin, E. Il'ichev, M. W. McCutcheon, J. F. Young & F. Nori. Controlled Generation of Squeezed States of Microwave Radiation in a Superconducting Resonant Circuit. *Phys. Rev. Lett.* **101**, 253602 (2008).
- [126] T. Ojanen & J. Salo. Possible scheme for on-chip element for squeezed microwave generation. *Phys. Rev. B* **75**, 184508 (2007).
- [127] J. R. Klauder, S. L. McCall & B. Yurke. Squeezed states from nondegenerate four-wave mixers. *Phys. Rev. A* **33**, 3204–3209 (1986).
- [128] K. Jensen, W. Wasilewski, H. Krauter, T. Fernholz, B. M. Nielsen, M. Owari, M. B. Plenio, A. Serafini, M. M. Wolf & E. S. Polzik. Quantum memory for entangled continuous-variable states. *Nature Phys.* **7**, 13–16 (2011).
- [129] A. Baust. *Characterization of Flux-driven Josephson Parametric Amplifiers*. Diploma thesis, Technische Universität München (2010). URL http://www.wmi.badw-muenchen.de/publications/theses/Baust,Alexander_Diplomarbeit_2012.pdf.

- [130] P. L. Tea, Jr. & H. Falk. Pumping on a Swing. *Am. J. Phys.* **36**, 1165–1166 (1968).
- [131] W. B. Case & M. A. Swanson. The pumping of a swing from the seated position. *Am. J. Phys.* **58**, 463–467 (1990).
- [132] C. W. Gardiner & M. J. Collett. Input and output in damped systems: Quantum stochastic differential equations and the master equation. *Phys. Rev. A* **31**, 3761–3774 (1985).
- [133] G. J. Dolan. Offset masks for lift-off photoprocessing. *Appl. Phys. Lett.* **31**, 337–339 (1977).
- [134] M. Wallquist, V. S. Shumeiko & G. Wendin. Selective coupling of superconducting charge qubits mediated by a tunable stripline cavity. *Phys. Rev. B* **74**, 224506 (2006).
- [135] D. I. Schuster. *Circuit Quantum Electrodynamics*. Ph.D. thesis, Yale University (2007).
- [136] Xilinx, Inc., 2100 Logic Drive, San Jose, CA 95124-3400, USA. URL <http://www.xilinx.com>.
- [137] K.-D. Kammeyer & K. Kroschel. *Digitale Signalverarbeitung* (Teubner Verlag, Wiesbaden, 2006).
- [138] P. Summer. *Simulation of the dual-path detector for propagating quantum microwaves*. Bachelor thesis, Technische Universität München (2011). URL http://www.wmi.badw-muenchen.de/publications/theses/Summer_Bachelorarbeit_2011.pdf.
- [139] E. Tholén. *Intermodulation in microresonators*. Doctoral thesis, KTH School of Engineering Sciences, Stockholm (2009).
- [140] L. Mandel & E. Wolf. *Optical Coherence and Quantum Optics* (Cambridge University Press, Cambridge, 1995).
- [141] C. W. J. Beenakker & H. Schomerus. Counting Statistics of Photons Produced by Electronic Shot Noise. *Phys. Rev. Lett.* **86**, 700–703 (2001).
- [142] H. Nyquist. Thermal Agitation of Electric Charge in Conductors. *Phys. Rev.* **32**, 110–113 (1928).

-
- [143] V. E. Manucharyan, E. Boaknin, M. Metcalfe, R. Vijay, I. Siddiqi & M. Devoret. Microwave bifurcation of a Josephson junction: Embedding-circuit requirements. *Phys. Rev. B* **76**, 014524 (2007).
- [144] H. B. Callen & T. A. Welton. Irreversibility and Generalized Noise. *Phys. Rev.* **83**, 34–40 (1951).
- [145] M. Born. *The Born-Einstein Letters* (Walker and Company, New York, 1971).
- [146] A. Einstein, B. Podolsky & N. Rosen. Can Quantum-Mechanical Description of Physical Reality Be Considered Complete? *Phys. Rev.* **47**, 777–780 (1935).
- [147] Z. Y. Ou, S. F. Pereira, H. J. Kimble & K. C. Peng. Realization of the Einstein-Podolsky-Rosen Paradox for Continuous Variables. *Phys. Rev. Lett.* **68**, 3663–3666 (1992).
- [148] J. Majer, J. M. Chow, J. M. Gambetta, J. Koch, B. R. Johnson, J. A. Schreier, L. Frunzio, D. I. Schuster, A. A. Houck, A. Wallraff, A. Blais, M. H. Devoret, S. M. Girvin & R. J. Schoelkopf. Coupling superconducting qubits via a cavity bus. *Nature* **449**, 443–447 (2007).
- [149] M. A. Sillanpää, J. I. Park & R. W. Simmonds. Coherent quantum state storage and transfer between two phase qubits via a resonant cavity. *Nature* **449**, 438–442 (2007).
- [150] T. Yamamoto, Yu. A. Pashkin, O. Astafiev, Y. Nakamura & J. S. Tsai. Demonstration of conditional gate operation using superconducting charge qubits. *Nature* **425**, 941–944 (2003).
- [151] J. H. Plantenberg, P. C. de Groot, C. J. P. M. Harmans & J. E. Mooij. Demonstration of controlled-NOT quantum gates on a pair of superconducting quantum bits. *Nature* **447**, 836–839 (2007).
- [152] M. Ansmann, H. Wang, R. C. Bialczak, M. Hofheinz, E. Lucero, M. Neeley, A. D. O’Connell, D. Sank, M. Weides, J. Wenner, A. N. Cleland & J. M. Martinis. Violation of Bell’s inequality in Josephson phase qubits. *Nature* **461**, 504–506 (2009).

List of publications

Publications related to this thesis

1. R. Di Candia, **E. P. Menzel**, L. Zhong, F. Deppe, A. Marx, R. Gross & E. Solano. Dual-Path Methods for Propagating Quantum Microwaves. *arXiv preprint arXiv:1308.3117* (2013).
Accepted for publication in New J. Phys.
Roberto Di Candia and Edwin P. Menzel contributed equally to this work.
2. L. Zhong, **E. P. Menzel**, R. Di Candia, P. Eder, M. Ihmig, A. Baust, M. Haeberlein, E. Hoffmann, K. Inomata, T. Yamamoto, Y. Nakamura, E. Solano, F. Deppe, A. Marx & R. Gross. Squeezing with a flux-driven Josephson parametric amplifier. *New J. Phys.* **15**, 125013 (2013).
Ling Zhong and Edwin P. Menzel contributed equally to this work.
3. **E. P. Menzel**, R. Di Candia, F. Deppe, P. Eder, L. Zhong, M. Ihmig, M. Haeberlein, A. Baust, E. Hoffmann, D. Ballester, K. Inomata, T. Yamamoto, Y. Nakamura, E. Solano, A. Marx & R. Gross. Path Entanglement of Continuous-Variable Quantum Microwaves. *Phys. Rev. Lett.* **109**, 250502 (2012).
4. **E. P. Menzel**, F. Deppe, M. Mariantoni, M. Á. Araque Caballero, A. Baust, T. Niemczyk, E. Hoffmann, A. Marx, E. Solano & R. Gross. Dual-Path State Reconstruction Scheme for Propagating Quantum Microwaves and Detector Noise Tomography. *Phys. Rev. Lett.* **105**, 100401 (2010).
5. M. Mariantoni, **E. P. Menzel**, F. Deppe, M. Á. Araque Caballero, A. Baust, T. Niemczyk, E. Hoffmann, E. Solano, A. Marx & R. Gross. Planck Spectroscopy and Quantum Noise of Microwave Beam Splitters. *Phys. Rev. Lett.* **105**, 133601 (2010).
Matteo Mariantoni and Edwin P. Menzel contributed equally to this work.

Other publications

1. T. Niemczyk, F. Deppe, H. Huebl, **E. P. Menzel**, F. Hocke, M. J. Schwarz, J. J. Garcia-Ripoll, D. Zueco, T. Hümmer, E. Solano, A. Marx & R. Gross. Circuit quantum electrodynamics in the ultrastrong-coupling regime. *Nature Phys.* **6**, 772–776 (2010).
2. G. M. Reuther, D. Zueco, F. Deppe, E. Hoffmann, **E. P. Menzel**, T. Weißl, M. Mariani, S. Kohler, A. Marx, E. Solano, R. Gross & P. Hänggi. Two-resonator circuit quantum electrodynamics: Dissipative Theory. *Phys. Rev. B* **81**, 144510 (2010).
3. E. Hoffmann, F. Deppe, T. Niemczyk, T. Wirth, **E. P. Menzel**, G. Wild, H. Huebl, M. Mariani, T. Weißl, A. Lukashenko, A. P. Zhuravel, A. V. Ustinov, A. Marx & R. Gross. A superconducting 180° hybrid ring coupler for circuit quantum electrodynamics. *Appl. Phys. Lett.* **97**, 222508 (2010).
4. M. Opel, S. Geprägs, **E. P. Menzel**, A. Nielsen, D. Reisinger, K.-W. Nielsen, A. Brandlmaier, F. D. Czeschka, M. Althammer, M. Weiler, S. T. B. Goennenwein, J. Simon, M. Svete, W. Yu, S.-M. Hühne, W. Mader & R. Gross. Novel multifunctional materials based on oxide thin films and artificial heteroepitaxial multilayers. *Phys. Status Solidi A*, **208**, 232–251 (2010).
5. T. Niemczyk, F. Deppe, M. Mariani, **E. P. Menzel**, E. Hoffmann, G. Wild, L. Eggenstein, A. Marx & R. Gross. Fabrication technology of and symmetry breaking in superconducting quantum circuits. *Supercond. Sci. Technol.* **22**, 034009 (2009).
6. F. Deppe, M. Mariani, **E. P. Menzel**, A. Marx, S. Saito, K. Kakuyanagi, H. Tanaka, T. Meno, K. Semba, H. Takayanagi, E. Solano & R. Gross. Two-photon probe of the Jaynes-Cummings model and controlled symmetry breaking in circuit QED. *Nature Phys.* **4**, 686–691 (2008).
7. F. Deppe, M. Mariani, **E. P. Menzel**, S. Saito, K. Kakuyanagi, H. Tanaka, T. Meno, K. Semba, H. Takayanagi & R. Gross. Phase coherent dynamics of a superconducting flux qubit with capacitive bias readout. *Phys. Rev. B* **76**, 214503 (2007).

Acknowledgments

At this point, I want to express my gratitude to everyone who contributed to the success of this work. In particular, I thank

- Prof. Dr. Rudolf Gross for giving me the opportunity to work on a highly attractive topic, supporting my ideas, and fruitful discussions.
- Dr. Achim Marx and Dr. Frank Deppe for advice and assistance in the lab and for proof-reading this thesis.
- Frank for discussions on interpreting the data which were often the key to a deeper understanding. Frank, your commitment and readiness to help are singular.
- Our collaborators and friends:
 - Roberto Di Candia, Dr. Daniel Ballester, and Prof. Enrique Solano from the University of the Basque Country UPV/EHU, Bilbao, Spain for their excellent theory support. Roberto, I will always remember our long and efficient working sessions on the analysis of the path entanglement.
 - Tsuyoshi Yamamoto, Ph.D. for designing and Kunihiro Inomata, Ph.D. for fabricating the Josephson parametric amplifier samples at the NEC Smart Energy Research Laboratories, Tsukuba, Japan. I give many thanks to their former group leader Prof. Yasunobu Nakamura for supporting us and for interesting discussions.
 - Matthias Ihmig for developing the FPGA logic. Matthias, I enjoyed working with you, not only since you are a profound expert of electrical engineering.
- My former diploma students, Miguel Ángel Araque Caballero, Alexander Baust, and Peter Eder, and bachelor student, Philipp Summer, for their excellent scientific work and the very good cooperation. Their commitment and specific skills were the key for the success of many experiments. Peter and Alex, I am very happy that both of you are doing a Ph.D. at the WMI and I wish you the very best for your future.
- Ling Zhong for assisting me in improving the cross-correlation detector, checking our lengthy dual-path Matlab scripts, and the good cooperation in our common publications. Ling, I wish you all the best for your project.

- Max Haeberlein, Alexander Baust and Elisabeth Hoffmann for their great support during redesigning and rebuilding the fridge.
- Matteo Mariantoni for the joint work on Planck spectroscopy and the quantum properties of beam splitters.
- Dr. Christian Probst, Dr. Karl Neumaier, and Dr. Kurt Uhlig for support on cryogenic technologies.
- Dr. Hans Huebl for fruitful discussions and lending me books.
- The working students, Benno Blaschke, Garlich Fischbeck, Chris Rau, Rolf Ripsam, and Franz Sterr for their help in developing power supplies, motorized phase shifters, measurement software, thermalizing DC lines and battery cabling.
- Ulrich Guggenberger for his support in designing the pulse driver for the cryogenic microwave switch.
- Christopher Eichler for fruitful discussions.
- All members of the qubit group for interesting discussions and the friendly working atmosphere.
- The workshop team, Helmut Thies, Robert Müller, Christian Reichlmeier, Julius Klaus, and Georg Nitschke for the high quality of their work and their suggestions to improve designs.
- Astrid Habel and Karen Helm-Knapp for gold plating of sample holders and processing printed circuit boards.
- Thomas Brenninger for giving advice on CAD software.
- Sepp Höß for developing the wire rope hoist for lifting the vacuum chamber.
- My current and former office colleagues, Fredrik Hocke, Matthias Kath, Bernhard Muschler, Deepak Venkateshvaran, and Edwar Xie for the good working atmosphere and for discussions on physics and other topics.
- Dr. Dietrich Einzel for discussions.
- Prof. Martin Brandt for lending us a power meter.
- Dr. Matthias Opel and Dieter Guratzsch for IT support.
- The Helium liquefaction team for continuous supply of Helium and for laying a screening pipe.
- Emel Dönertas, Ludwig Osslander and Liane Lindner for administrative tasks.
- All members of the WMI for the very good working atmosphere.
- Especially, my parents for always supporting me in every respect and for all the memories we share.